Studies on Solid-state Polymerization Triggered by High Energy Charged Particle and Fabrication of Functional Nanomaterials

Shugo Sakaguchi

2023

Preface

The present thesis is the collection of studies that have been performed from 2017 to 2023 at the Department of Molecular Engineering, Graduate School of Engineering, Kyoto University under direction of Professor Shu Seki. The studies in this thesis are focused on organic nano-fabrication of organic materials via polymerization reactions induced by irradiation of high-energy charged particles.

Contents

General Introduction

Since the dawn of quantum mechanical aspects on atoms and molecules, interactions of ionizing radiations with condensed matters had been the center of analysis techniques for the electronic structures of them.[1–4] Particularly the Coulombic interactions between the charged particles with relatively high momentum and electrons confined in their orbitals have been discussed precisely in terms of experimental energy loss of the incident charged particles and/or cross section of ionization events induced in the target condensed matters.[5,6] For the quantitative experimental analysis of the loss/events in the system, X-rays/γ-rays and high energy electron beams have been often of choices because of homogeneity of the released energy from the ionizing radiation into the target matters, which helps statistical counting of the events/resulting products and intermediates by conventional analysis protocols such as spectroscopic/microscopic techniques.[7,8] In contrast to the classical ionizing radiation applied to reveal atomic/molecular structures, heavy charged particles played also a significant role to clarify the structures, as evident in the initial success of Rutherford scattering experiments via momentum transfer from incident charged particle to the target atoms. The energy dissipation processes from the incident charged particles, therefore, had awakened always general interests of scientists working on condensed matter physics, nuclear physics, astrophysics, etc. For instance, the visualization of high energy charged particle tracks in the organic/inorganic matters was successfully applied to assess energy/momentum of the incident charged particles, giving clear evidences of nuclear reactions caused by the particles.[9] Within 20th century, the theoretical background interpreting the interactions has been well developed in correlation with the experimental observation, leading to the sophisticated formulations. Initial benchmark of the formulation was first established by Bethe, starting from a simple binary elastic collision model in terms of T: transferred energy from one to the other,[10,11]

$$T = \frac{4m_1m_2}{\left(m_1+m_2\right)^2}\frac{1}{2}m_1v^2\cos^2\varphi \tag{1},$$

where, m_1 and m_2 are masses of incident and target particles, v and φ are the velocity of the incident particle and recoil angle, respectively. In case of the binary collision model, the collision diameter b can be used, as follows with the atomic number Z_1 and Z_2 of the incident particle and target the atom ,

$$b = \frac{2Z_1Z_2e^2}{\mu v^2} \tag{2}$$

and

$$\mu = \frac{m_1m_2}{m_1+m_2} \tag{3},$$

where μ is reduced mass of the system and e is an elementary charge. The scattering angle is therefore in a simple direct correlation to b and a scattering parameter s as,

$$\tan\varphi = \frac{2s}{b} \tag{4},$$

and a following formulation of T is obtained as,

$$T = \frac{4m_1m_2}{\left(m_1+m_2\right)^2}\cdot\frac{1}{2}m_1v^2\cdot\frac{1}{1+\left(\frac{2s}{b}\right)^2} \tag{5}.$$

Considering a small deviation of s as Δs, the differential cross section ($\Delta\sigma$) of the incident particle by the target will be given by,

$$\Delta\sigma = 2\pi s\Delta s \tag{6},$$

and the resulting $d\sigma$ is obtained as,

$$d\sigma = 2\pi s\left(\frac{ds}{dT}\right)dT = \pi\frac{d\left(s^2\right)}{dT}dT = \frac{\pi b^2}{4}\frac{4m_1m_2}{\left(m_1+m_2\right)^2}\frac{1}{2}m_1v^2\frac{dT}{T^2} \tag{7}.$$

Eq. (6) can be represented explicitly for the momentum transfer between the incident particle and the target atom in Rutherford back scattering processes as,

$$\mathrm{d}\sigma = \frac{2\pi Z_1^2 Z_2^2 e^4}{m_2 v^2}\frac{\mathrm{d}T}{T^2} \tag{8}.$$

Now, the ionization events in the condensed phases as well as successive chemical reaction in the matters are evidently regarded as inelastic collision events for an incident particle.[12] Ionization cross section in classical Thomson model could be delivered by eq. (8) based on Rutherford scattering scheme,[2,13] however the more detailed discussions had been started by an initiative of Born with quantum mechanical views of target substances with a general wave function of their frontier orbital: $\psi(\mathbf{r})$ which can be derived by a general Schrödinger equation as,

$$\left(\nabla^2 + k^2\right)\psi(\mathbf{r}) = U(\mathbf{r})\psi(\mathbf{r}), \quad V(\mathbf{r}) = \frac{\hbar^2 U(\mathbf{r})}{2\mu} \tag{9},$$

and the solutions of eq. (8) are given with an use of Green's function of $G_{\pm}(\mathbf{r})$ and an incident plane-wave function $\phi_{inc}(\mathbf{r})$ as,[14]

$$\psi(\mathbf{r}) = \phi_{inc}(\mathbf{r}) + \int G_{\pm}(\mathbf{r}-\mathbf{r}')U(\mathbf{r}')\psi(\mathbf{r}')\mathrm{d}^3 r' \tag{10}.$$

And

$$G_{\pm}(\mathbf{r}-\mathbf{r}') = -\frac{1}{4\pi}\frac{\exp\left(\pm ik|\mathbf{r}-\mathbf{r}'|\right)}{|\mathbf{r}-\mathbf{r}'|} \tag{11},$$

under the following requirements for $\phi(\mathbf{r})$ and $G_{\pm}(\mathbf{r})$ of

$$\left(\nabla^2 + k^2\right)\phi(\mathbf{r}) = 0 \tag{12}$$

and

$$\left(\nabla^2 + k^2\right)G_{\pm}(\mathbf{r}-\mathbf{r}') = \delta^d(\mathbf{r}-\mathbf{r}') \tag{13}.$$

Considering only the contribution of the outgoing wave function from **r**' leading to $G_{+}(\mathbf{r})$, the solution of the above Schrödinger equation is given by Lippmann-Schwinger equation as,[15]

$$\psi(\mathbf{r}) = \phi_{inc}(\mathbf{r}) + \int G_{+}(\mathbf{r}-\mathbf{r}')U(\mathbf{r}')\psi(\mathbf{r}')\mathrm{d}^3 r' \tag{14}.$$

Here, when presuming **r** >> **r**', the norm of displacement vector can be represented by,

$$\left|\mathbf{r}-\mathbf{r}'\right| = r - \mathbf{n}\cdot\mathbf{r}' \tag{15},$$

then a simplified expression of form for Green's function can be obtained as,

$$G_{+}\left(\mathbf{r}-\mathbf{r}'\right) = -\frac{1}{4\pi}\frac{\exp\left(ikr\right)}{r}\exp\left(-ik\mathbf{n}\cdot\mathbf{r}'\right) \tag{16}.$$

By substituting this into eq. (13), the resulting wave function of the target is represented as,

$$\psi\left(\mathbf{r}\right) = \phi_{inc}\left(\mathbf{r}\right) + \left[-\frac{1}{4\pi}\int \exp\left(-ik\mathbf{n}\cdot\mathbf{r}'\right)U\left(\mathbf{r}'\right)\psi\left(\mathbf{r}'\right)\mathrm{d}^3r'\right]\frac{\exp\left(ikr\right)}{r} \tag{17}.$$

To lead an explicit analytical solution for $\psi(\mathbf{r})$ of electrons responsible to the first ionization energy of the target materials, Born approximation to eq. (14) is used expanded with Born series,[16] and take the first order expansion as an approximate as follows,

$$\psi\left(\mathbf{r}\right) = \phi_{inc}\left(\mathbf{r}\right) + \int G_{+}\left(\mathbf{r}-\mathbf{r}'\right)U\left(\mathbf{r}'\right)\phi_{inc}\left(\mathbf{r}'\right)\mathrm{d}^3r' \tag{18}.$$

By comparing eq. (18) to (17), provisionally the solution has been obtained as,

$$\psi\left(\mathbf{r}\right) = \phi_{inc}\left(\mathbf{r}\right) + \left[-\frac{1}{4\pi}\int \exp\left(-ik\mathbf{n}\cdot\mathbf{r}'\right)U\left(\mathbf{r}'\right)e^{i\mathbf{k}\cdot\mathbf{r}'}\mathrm{d}^3r'\right]\frac{\exp\left(ikr\right)}{r} \tag{19}.$$

Here, **n** is an unit vector. The wave vectors in the integrant can be substituted by,

$$\mathbf{K} = k\mathbf{n} - \mathbf{k} = \mathbf{k}' - \mathbf{k} \tag{20},$$

and the simplified wave function is given by,

$$\psi\left(\mathbf{r}\right) = \phi_{inc}\left(\mathbf{r}\right) + \left[-\frac{1}{4\pi}\int \exp\left(-i\mathbf{K}\cdot\mathbf{r}'\right)U\left(\mathbf{r}'\right)\mathrm{d}^3r'\right]\frac{\exp\left(ikr\right)}{r} \tag{21}.$$

The second term in eq. (21) is responsible for the inelastic energy loss of an incident particle which can be transferred to the target. Considering the term separatory as a function of $f(\theta, \varphi)$, eq. (21) can be rewritten as,

$$\psi\left(\mathbf{r}\right) \simeq \exp\left(i\mathbf{k}\cdot\mathbf{r}\right) + f\left(\theta,\varphi\right)\frac{\exp\left(ikr\right)}{r} \tag{22}$$

and

$$f(\theta,\varphi)=-\frac{1}{4\pi}\int\exp(-i\mathbf{K}\cdot\mathbf{r}')U(\mathbf{r}')\mathrm{d}^3r' \tag{23},$$

respectively. Now the differential inelastic cross section of dσ can be formulated clearly as,

$$\mathrm{d}\sigma=\frac{1}{16\pi^2}\left|\langle\phi_{\mathbf{k}'}|U|\phi_{\mathbf{k}}\rangle\right|^2\mathrm{d}\Omega \tag{24},$$

where dΩ is the differential solid angle. With the measure of momentum of the incident particle prior after the collision events as *p* and *p*', respectively, eq. (24) can be derived as,

$$\mathrm{d}\sigma=\frac{\mu^2}{4\pi^2\hbar^4}\frac{p'}{p}\left|\langle\phi_{\mathbf{k}'}|V|\phi_{\mathbf{k}}\rangle\right|^2 \tag{25},$$

where $V(\mathbf{r})$ is the Coulombic potential between the particles as represented simply by,

$$V=\frac{Z_1Z_2e^2}{r}-Z_1\sum_{i=1}^{Z_2}\frac{e^2}{|\mathbf{r}-\mathbf{r}_i|} \tag{26},$$

Then the integration over **r** can be written by,

$$\int\exp(i\mathbf{K}\cdot\mathbf{r})\frac{\mathrm{d}\mathbf{r}}{|\mathbf{r}-\mathbf{r}_i|}=\frac{4\pi}{K^2}\exp(i\mathbf{K}\cdot\mathbf{r}_i) \tag{27}.$$

Thus, eq. (25) transforms into follows with an atomic matrix element called as Fano factor: $|F_n(\mathbf{K})|^2$ [17,18]

$$\mathrm{d}\sigma=\frac{4Z_1^2\mu^2e^4}{\hbar^4K^4}\frac{p'}{p}\left|F_n(\mathbf{K})\right|^2\mathrm{d}\Omega \tag{28}$$

and

$$\left|F_n(\mathbf{K})\right|^2=\int\sum_i\exp(i\mathbf{K}\cdot\mathbf{r}_i)u_n^*u_0\mathrm{d}\mathbf{r}_i \tag{29},$$

where *u* is the eigenfunction of electron orbital in the target. Considering the energy and momentum consevation law, a relationship between *K* and Ω is given as,

$$\mathrm{d}(K^2)=\frac{pp'}{\pi}\mathrm{d}\Omega \tag{30}.$$

Therefore eq. (28) is eqivalent to:

$$\mathrm{d}\sigma=\frac{4\pi Z_1^2\mu^2e^4}{\hbar^4K^4}\frac{1}{p^2}\left|F_n(\mathbf{K})\right|^2\mathrm{d}(K^2) \tag{31}.$$

Given the kinetic energy transferred to an electron as $Q=\frac{\hbar^2K^2}{2m_e}$ into eq. (31), dσ can be finally appeared as,

$$\mathrm{d}\sigma=\frac{2\pi Z_1^2e^4}{m_ev^2}\frac{1}{Q^2}\left|F_n\left(Q\right)\right|^2\mathrm{d}Q \tag{32}.$$

This equation is the theoretical differential cross section of the incident particle in an inelastic collision event.[18]

Statistical treatment of the collision events within the matter will lead overall energy loss of an incident particle along the particle trajectory. Now, the averaged energy loss (S) of the particle per unit length of the trajectory is defined by,

$$-\frac{dE}{dx}=N\int Td\sigma\equiv S \tag{33},$$

where N is the number density of atoms in the target. In this study, the energy delivered by the incident particle to the molecular materials is predominantly consumed as ionization events, where the velocity of an incident particle is relatively larger than the angular momentum of electrons bound to the molecules. When only treat the case of the larger velocity than the Massey's criterion[19] is trated, S is given with static mass of electron (m_e) by,

$$S=\frac{2\pi Z_1^2e^4}{m_ev^2}N\int_{T_{\min}}^{T_{\max}}\frac{\mathrm{d}T}{T} \tag{34},$$

where $T_{\max}$ equals to $2m_ev^2$, and $T_{\min}$ depends on the ionization potentials of chemical substances in the target. If the discrete energy levels of electrons bound in the target molecule are given by ε_i, an accurate expression of the integration in the above equation should be,

$$S=\frac{2\pi Z_1^2e^4}{m_ev^2}N\sum_i n_i\ln\frac{2m_ev^2}{\varepsilon_i} \tag{35}.$$

Now the density of states for electrons in the target matter are high enough to average by numerical integration over the range of ε_i, the summation can be parameterized by an averaged ionization potential of I as,[20]

$$\frac{1}{Z_2}\sum_i n_i \ln \varepsilon_i = \ln I \tag{36}$$

Then S can be expressed with I as,

$$S = \frac{2\pi Z_1^2 e^4}{m_e v^2} N Z_2 \ln\left(\frac{2m_e v^2}{I}\right) \tag{37}$$

The direct energy transfer from the incident particle to the target matter below its ionization potentials can be calculated based on the total transition dipoles of the target molecular substances. The generalized oscillator strength ($f_n(Q)$) corresponding to a discrete energy level with quantum number of n can be represented by $F_n(Q)$ as,

$$f_n(Q) = \frac{\varepsilon_n}{Q}\left|F_n(Q)\right|^2 \tag{38}$$

Here the oscillator strength is defined as a function of transferred energy to the molecular substances (Q). Thus the total energy loss by this scheme can be calculated by,

$$S = N\sum_n \int \varepsilon_n \frac{2\pi Z_1^2 e^4}{m_e v^2}\frac{\mathrm{d}Q}{Q^2}\left|F_n(Q)\right|^2 = N\sum_n \int \frac{2\pi Z_1^2 e^4}{m_e v^2} f_n(Q)\frac{\mathrm{d}Q}{Q} \tag{39}$$

For f_n, its summing up should be equal to the total number of electrons in the target: Fermi's golden rule. This can be simply represented by,

$$\sum f_n = Z_2 \tag{40}$$

and again the oscillator strength is correlated directly to I as,

$$\ln I = \sum_n f_n \ln \varepsilon_n \tag{41}$$

Substituting eq. (41) into eq. (38) leads to

$$S = \frac{2\pi Z_1^2 e^4}{m_e v^2} N Z_2 \ln\left(\frac{2m_e v^2}{I}\right) \tag{42}$$

This shows striking contrast to eq. (37), showing equal contribution of energy transfer above and below I; the averaged ionization potential. Finally the overall value of S can be,

$$S = \frac{4\pi Z_1^2 e^4}{m_e v^2} N Z_2 \ln\left(\frac{2m_e v^2}{I}\right) \quad (43).$$

Based on this equation, the spatial distribution of released energy by an incident particle is discussed in an isolated particle track.

Since quantum mechanical description of electronic stopping was proposed for the first time by Bethe[10,11] in 1930's, a number of further theoretical approaches have been continuously discussed aiming more precise estimation of stopping power within variable energy regimes of the incident charged particles. Particularly in the high-velocity regime (above 1 MeV/u), the relativistic effects were taken into accounts by Bloch[21], the shell correction and the density effect correction by Fano,[22] and the effective charge correction by Bohr and Northcliff,[23,24] respectively. In the low-velocity regime (significantly below 1 MeV/u), nuclear stopping becomes remarkable resulting in developments of the non-perturbative stopping models based on the electron exchange within the collision events by Firsov,[25] the Thomas-Fermi model by Lindhard and Scharff,[26] and the electron gas model by Fermi and Teller.[27] At the later stage of the collision cascades, a high energy charged particle penetrates the target with slowing down to as represented by $T_{\min}$ in eq. (34). Here the electronic stopping no longer be derived from a series of separable binary collisions because of complicated energy exchange between the particle and the target electrons, which is often called as "electron-phonon coupling". Several theories have therefore been proposed embedding new electronic and nuclear stopping mechanisms: two-temperature models,[28] the Coulomb explosion model,[29] and thermal spike model.[30]

Overcoming these complexities due to variable velocity-dependent electronic stopping processes, quantum-mechanical descriptions by use of first-principle calculations have attracted attentions since 1980s.[31–34] These approaches have striking advantages in terms of non-empirical calculation of electronic stopping over a wide range of particle velocities including the stopping power maximum. The rapid development of computational capabilities such as

peta-scale or exa-scale supercomputers have also realized direct simulation of the electron dynamics of the system incorporating the quantum-mechanical effects, which now allows us to estimate precisely the mean energy transfer within many-body and complicated molecules with time-dependent density functional theory (TDDFT) simulations. The protocols to assess the energy transfer are based on a simple scheme to predict distinct initial and final states of the systems with Kohn-Sham orbitals as:

$$i\frac{\partial}{\partial t}\psi(\boldsymbol{r},t)=\left[\nabla^2+V(N,\boldsymbol{r},t)\right]\psi(\boldsymbol{r},t) \quad (44),$$

and the dynamic potential of V has been simulated in every step with short enough time intervals. In the most recent cases, the steps were divided into 2 at, revealing gradual changes of the energy state of each target molecule.[35] In this regard, further detailed models were developed rapidly in sequence, taking self-consistent, non-perturbative, and time-lapse treatment of electron dynamics into accounts for metals,[36-38] semiconductors,[39,40] and biomolecules.[41,42]

References

1. Gieger, H.; Marsden, E. *Proc. Roy. Soc.* **1909**, *82*, 495.
2. Rutherford, E. *Philos. Mag.* **1911**, *21*, 212.
3. Darwin, C.G. *Philos. Mag.* **1912**, *13*, 901–920.
4. Thomson, J.J. *Philos. Mag.* **1912**, *6-23*, 449–457.
5. Bohr, N. *Philos. Mag.* **1913**, *25*, 10–31.
6. Bohr, N. *Philos. Mag.* **1915**, *30*, 581–612.
7. Seki, S.; Yoshida, Y.; Tagawa, S.; Asai, K. *Macromolecules* **1999**, *32*, 1080–1086.
8. Kobayashi, K.; Tagawa, S. *J. Am. Chem. Soc.* **2003**, *125*, 10213–10218.
9. Wilson, C.T.R. *Proc. Roy. Soc. A* **1923**, *104*, 192–212.
10. Bethe, H. *Ann. Phys.* **1930**, *5*, 325–400.

11. Bethe, H. *Z. Phys.* **1932**, *76*, 293–299.
12. Seki, S.; Sakurai, T.; Omichi, M.; Saeki, A.; Sakamaki, D. *High Energy Charged particle: Their Chemistry and Use as Versatile Tools for Nanofabrication.* Springer: London, UK, 2015.
13. Rutherford, E. *Philos. Mag.* **1911**, *21*, 669.
14. Kittel, C. *Quantum Theory of Solids.* John Wiley & Sons Inc.: New York, USA, 1963.
15. Lippmann, B.A.; Schwinger, J. *Phys. Rev.* **1950**, *79*, 469–480.
16. Born, M. *Z. Physik* **1926**, *38*, 803–827.
17. Fano, U. *Phys. Rev.* **1954**, *95*, 1198.
18. Fano, U. *Ann. Rev. Nuclear Sci.*, **1963**, *13*, 1–66.
19. Mott, N.F.; Massey, H.S.W. *The Theory of Atomic Collisions.* 3rd ed.; Oxford University Press: Oxford, USA, 1965.
20. Bohr, N.; Dan, K. *Vidensk. Selsk. Mat.-Fys. Medd.* **1948**, *18*, 1–144.
21. Bloch, F. *Ann. Phys.* **1933**, *16*, 285–320.
22. Fano, U. *Phys. Rev.* **1947**, *72*, 26–29.
23. Bohr, N. *Phys. Rev.* **1940**, *58*, 654–655.
24. Northcliffe, L.C. *Phys. Rev.* **1960**, *120*, 1744.
25. Firsov, O.B. *J. Exp. Theor. Phys.* **1957**, *5*, 1192–1196.
26. Lindhard, J.; Scharff, M. *Phys. Rev.* **1961**, *124*, 128–130.
27. Fermi, E.; Teller, E. *Phys. Rev.* **1947**, *72*, 399–408.
28. Seitz, F.; Koehler, J.S. *Displacement of Atoms During Irradiation.* Solid State Physics; Seitz, F.; Turnbull, D., Eds.; Academic Press: New York, USA, 1956; Volume 2, pp. 305–448.
29. Fleischer, R.; Price, P.; Walker, R. *J. Appl. Phys.* **1965**, *36*, 3645–3652.
30. Lifshitz, I.M.; Kaganov, M.I.; Tanatarov, L.V. *J. Nucl. Energy A* **1960**, *12*, 69–78.
31. Echenique, P.M.; Nieminen, R.M.; Ritchie, R.H. *Solid State Commun.* **1981**, *37*, 779–781.

32. Nagy, I.; Arnau, A.; Echenique, P.M.; Zaremba, E.; *Phys. Rev. B* **1989**, *40*, 11983–11985.
33. Pitarke, J.M.; Ritchie, R.H.; Echenique, P.M. *Phys. Rev. B* **1995**, *52*, 13883–13902.
34. Nagy, I.; Apagyi, B. *Phys. Rev. A* **1998**, *58*, 1653–1656.
35. Schleife, A.; Draeger, E.W.; Anisimov, V.M.; Correa, A.A.; Kanai, Y. *Comput. Sci. Eng.* **2014**, *16*, 54-61.
36. Quijada, M.; Borisov, A.G. *Phys. Rev. A* **2007**, *75*, 042902.
37. Zeb, M.A.; Kohanoff, J. *Phys. Rev. Lett.* **2012**, *108*, 225504.
38. Schleife, A.; Kanai, Y.; Correa, A.A. *Phys. Rev. B* **2015**, *91*, 014306.
39. Yost, D.C.; Kanai, Y. *Phys. Rev. B* **2016**, *94*, 115107.
40. Ullah, R. Corsetti, F.; Sánchez-Portal, D.; Artacho, E. *Phys. Rev. B* **2015**, *91*, 125203.
41. Covington, C.; Hartig, K. *Phys. Rev. A* **2017**, *95*, 052701.
42. Yost, D.C.; Kanai, Y. *J. Am. Chem. Soc.* **2019**, *141*, 5241.

Chapter 1. Conjugated Nanowire Sensors via High-Energy Single-Particle-Induced Linear Polymerization of 9,9'-spirobi[9*H*-fluorene] Derivatives

Synopsis

Nanostructures composed of conjugated polymers or π-conjugated molecules provide sensing platforms with large specific surface areas. One of the feasible approaches to accessing such nanostructured miniaturized sensors with ultrahigh sensitivity is to develop a network of organic nanowires with optical/electronic properties that can measure signals upon interacting with the analytes at their surfaces. In this work, organic nanowires with controlled number density and uniform length were fabricated by one-dimensional solid-state polymerization of 9,9′-spirobi[9*H*-fluorene] (SBF) derivatives triggered by high-energy single particles. SBF was chosen as a conjugated molecular motif with the interplay of high density of π-electrons, high solubility, and uniform solid-state structures, allowing us to fabricate sensing platforms via solution processing. The as-deposited energy density in linear polymerization nanospace was theoretically analyzed by a collision model, interpreting nanowire sizes at sub-nanometer levels. The substitution of bromine atoms was confirmed to be effective not only for the higher collision probability of the incident particles but also for the remarkable increase in radiolytic neutral radical yield via C-Br cleavages or electron-dissociative attachments onto the bromine atoms. The fluorescence spectra of SBF-based nanowires were different from those of SBF derivatives due to extended bond formation as a result of polymerization reactions. Fluorescence was quenched by the addition of nitrobenzene, indicating the potential use of these nanowires for fluorometric sensing applications. Microwave-based conductivity measurements revealed that the SBF-based

nanowires exhibited charge carrier transport property upon photoexcitation, and that the conductivity was changed upon treatment with nitrobenzene vapors. The presented strategy of bromination of aromatic rings for efficient fabrication of controlled nanowire networks with favorable fluorescent and charge transport properties of nanowires advances the development of nanostructured sensing systems.

Introduction

Fluorenes, analogs of biphenyl rings bridged by a sp^3-carbon atom at the 2,2'-positions, have been recognized as one of the simplest motifs of conjugated molecules with efficient optoelectronic properties owing to their extended electron conjugation over the planar structure.[1,2] The unique electronic structure of fluorene derivatives is represented by degenerated π-orbitals with a direct energy gap, which is responsible for the high fluorescence quantum yields obtained in the blue region. The reactive 2,7-positions of the fluorene cores have often been used to polymerize the derivatives, affording poly(fluorene)s by facile polymerization protocols. The conjugated π-orbitals on the fluorene cores can be extended along the linear chain of poly(fluorene)s, which enables the formation of promising electronic conducting polymer backbones applicable to flexible optoelectronic devices.[3–5] In contrast to the planar fluorene motifs, 9,9′-spirobi[9*H*-fluorene] (SBF) is a fluorene dimer with orthogonal arrangement of biphenyl structures in the molecule. SBFs were already synthesized in the 1930s,[6,7] and increasing attention has been paid to SBFs due to their characteristic properties of electron delocalization over the skeletons and high solubility in typical organic solvents without any solubilizing substituents; the latter is a clear advantage of planar fluorenes and their derivatives.[8] The characteristic stereostructure of SBFs effectively hampers directional molecular aggregations in their solid state, leading to the interplay of high density of π-electrons, high solubility, and uniform solid-state structures. Thus, SBFs have been regarded as a

promising choice in organic electronic devices such as organic photovoltaics or organic light-emitting diodes as hole-transporting materials.[9]

One-dimensional conjugated structures with optical and/or electrical properties are important for electronic and sensing applications owing to the potentially high conductivity, light emission, and charge/energy transport properties.[10–14] In sensing systems, the binding of biological or chemical species on the surface of sensing materials induced a variety of changes in the abovementioned electrical/optical properties that were expected in the output signals. The important point is to maximize the modulation of the signals by binding biological or chemical species (i.e., analytes) on the nanowire surfaces. Till date, the representative output signals are classified as electrical, amperometric, conductometric, potentiometric, fluorometric, calorimetric, and gravimetric ones. Miniaturization of sensor dimensions has attracted attention not only with respect to sensitivity but also in practical application and multi-sensing chips. Particularly, extension of surface area is crucial for extraordinarily high sensitivity. In this regard, nanostructured materials—nanoparticles, nanowires, nanotubes, nanoribbons, *etc*.––play a key role in sensing materials. There are two approaches toward versatile, efficient, cost-effective production of nanostructured sensing platforms: one is top-down nanofabrication of matrices followed by surface modifications with the functional groups specified for absorbents, while the other is direct miniaturization of materials starting from the sensing materials themselves. One-dimensional nanowires of conjugated molecules/polymers are promising candidates, since they have potential for unidirectional carrier/energy transport along the nanowire conjugation direction and large surface areas accessible by the analytes. Directional transport enables the reading of electronic output signals upon contact with the analytes.

Precise control of the overall surface areas is key to ensuring ultrahigh sensitivity and reproducibility of the platform. However, it is still difficult to finely control the number density and length of nanowires simultaneously. In previous findings, the chemical reactions triggered by vertically incident high-energy charged particles on organic films could form organic nanowires with the desired number density and length and extremely high aspect ratios (**Figure 1**).[15–24] This unique method, referred to as single particle triggered linear polymerization (STLiP), is applicable to a type of small molecules[22–28] that can be polymerized in the solid state upon irradiation with high-energy charged heavy particles. The obtained nanowires with thickness of around 10 nm can be employed as not only an immobilization matrix but also sensing materials themselves. Asano *et al.* previously reported nanowires fabricated from polymers containing unreacted terminal alkyne groups functioning as a nanowire-shaped matrix that were further functionalized by using "click" chemistry, but the nanowire thickness increased.[19,20] Therefore, the next challenge is to fabricate organic nanowires from pure conjugated monomer structures that can be utilized for sensing materials with large accessible surface areas.

Herein, the author report the fabrication of nanowires via solid-state polymerization of SBF derivatives by high-energy charged particle irradiation. The SBF monomer is highly soluble in organic solvents despite the lack of solubilizing chains and thus behaves as a pure conjugated motif. After irradiation with high-energy particles, clear nanowires were isolated and visualized successfully by using microscopy techniques. The nanowires show a different fluorescence spectral pattern and electrical conductivity from those of the initial material, which offers sufficient signal outputs as sensing systems.

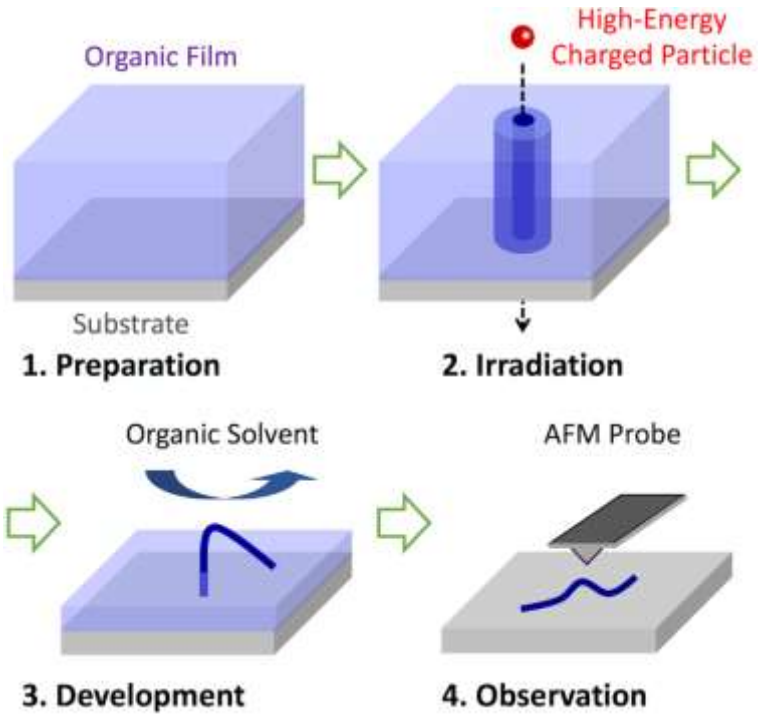

Figure 1. Schematic illustration of nanowire fabrication processes from organic thin films by using high-energy ion irradiation and following isolation by development with organic solvents.

Experimental

Materials. 9,9'-spirobi[9*H*-fluorene] (SBF), 2-bromo-9,9'-spirobi[9*H*-fluorene] (2Br-SBF), 4-bromo-9,9'-spirobi[9*H*-fluorene] (4Br-SBF), 2,2'-dibromo-9,9'-spirobi[9*H*-fluorene] (2,2'Br_2-SBF), 2,7-dibromo-9,9'-spirobi[9*H*-fluorene] (2,7Br_2-SBF), 2,2′,7,7′-tetrabromo-9,9′-spirobi[9*H*-fluorene] (Br_4-SBF), 2,2"-bi-9,9'-spirobi[9*H*-fluorene] (SBF_2), and 2,2":7",2""-ter-9,9'-spirobi[9*H*-fluorene] (SBF_3) were purchased from Tokyo Chemical Industry Co. and used as-received.

Nanowire Fabrication and Observation. Si substrates were cut into 1.5×1.5 cm^2 square pieces, and sonicated in 2-propanol and dried. The quartz substrates used had 1 mm thickness and dimensions 9 × 40 mm. All the substrates were exposed to UV-O_3 to clean the surface prior to use. All the SBF derivatives were dissolved in $CHCl_3$ and dropcast or spincoated onto the

substrates to yield thin films. The thickness of the films was set at 100–500 nm, as confirmed by a Veeco Instruments Inc. Dektak 150 surface profiler. For high-energy particle source, the author used 350 MeV $^{129}Xe^{26+}$ ions generated from a cyclotron accelerator or cluster ions of 1.5 MeV $^{27}Al^{+}$, 3.0 MeV $^{27}Al_2^{+}$, 4.5 MeV $^{27}Al_3^{+}$, and 6.0 MeV $^{27}Al_4^{+}$ generated from a tandetron accelerator at Takasaki Advanced Radiation Research Institute. All the thin films were evacuated ($< 1 \times 10^{-4}$ Pa), and high-energy particles were irradiated orthogonally to the film surfaces at the fluence of 1×10^{9}–5×10^{11} cm^{-2}. No sublimation under vacuum was confirmed based on the film thickness. After irradiation, the films were immersed in toluene for ~1 min at room temperature. The morphologies of the nanowires were determined by using a Bruker Co. Multimode 8 atomic force microscope (AFM).

Simulation of High-Energy Particle Irradiation. The loss of the kinetic energy of the ions due to their traversal through the organic films (linear energy transfer; LET) was estimated using the SRIM 2008 simulation code. The film thickness was set at 10 μm (larger than the actual maximum film thickness). The density of the film was set at 1.25,[29] 1.48, 1.63,[30] 1.84,[31] 1.34,[32] and 1.24[33] g cm^{-1} for SBF, 2Br(4Br)-SBF, 2,2'Br_2(2,7Br_2)-SBF, Br_4-SBF, SBF_2, and SBF_3, respectively. The ^{129}Xe particle was irradiated 1000 times.

Fluorescence Spectroscopy. The fluorescence spectra of the films or bundled nanowires on the quartz substrate were measured at room temperature in air using a JASCO FP-8500 fluorescence spectrophotometer. The bundled nanowires were obtained by irradiating with 350 MeV $^{129}Xe^{26+}$ at the fluence of 1.0×10^{11}–5.0×10^{11} cm^{-2} on the quartz substrate, isolated by development with toluene, and used for the measurements.

X-ray Photoelectron Spectroscopy (XPS). X-ray photoelectron spectra were measured on a SHIMADZU ESCA-3400 electron spectrometer. Bundled nanowires were obtained by 350 MeV $^{129}Xe^{26+}$ irradiation at the fluence of 1.0×10^{11}–5.0×10^{11} cm^{-2} on the silicon substrate

and the system evacuated (< 1×10^{-5} Pa) prior to the measurements with the bulk films as the references.

Flash-Photolysis Time-Resolved Microwave Conductivity (FP-TRMC). Transient conductivity was measured by the FP-TRMC technique at room temperature in air. Film samples on a quartz plate were prepared by dropcasting a $CHCl_3$ solution of SBF and drying under vacuum for 1 h at room temperature. The film of SBF nanowires was prepared by irradiation with 350 MeV $^{129}Xe^{26+}$ at the fluence of 1×10^{11} on the quartz substrate and developed by using toluene. Transient charge carriers were generated upon photoexcitation with laser pulses of third harmonic generation (λ = 355 nm) radiated from a Spectra Physics INDI-HG Nd:YAG laser with a pulse duration of 5–8 ns. The photon density of 355 nm pulse was set at 9.1×10^{15} photons cm^{-2} $pulse^{-1}$. The probing microwave frequency and power were 9.1 GHz and 3 mW, respectively. Photoconductivity transients were demodulated through a GaAs crystal-diode with Schottky-barriers (rise time < 1 ns), and monitored by a Tektronix TDS3032B digital oscilloscope. The observed conductivities were normalized, given by the photocarrier generation yield (ϕ) multiplied by the sum of the charge carrier mobilities ($\Sigma\mu$):

$$\phi\sum\mu=\left(eAI_0F\right)^{-1}\frac{\Delta P_r}{P_r}, \quad (1)$$

where, e, A, I_0, F_{light}, P_r, and ΔP_r are the elementary charge, sensitivity factor (S cm^{-1}), incident photon density of the excitation laser (photon cm^{-2}), correction (or filling) factor (cm^{-1}), and reflected microwave power and its change, respectively. The value of F was calculated as $1.0–1.2 \times 10^3$ cm^{-1} for all the prepared films based on the optical density depth profiles and geometry of the samples overlapped to the electric field strength in the cavity.

Size-Exclusion Chromatography (SEC). The nanowires on substrates, fabricated by irradiation of films of SBF derivatives with 350 MeV $^{129}Xe^{26+}$ ions at the fluence of 1×10^{11}

cm^{-2}, were sonicated in THF. The eluent was filtered through a PTFE membrane, concentrated, and injected into the analytical SEC system to study the excluded volume of polymerized products. The measurement was performed at 40 °C on a Hitachi chromatography instrument (L-2130, L-2455, L-2350) with Shodex columns (KF-804L/KF-805L) using tetrahydrofuran (Wako Pure Chemical Industries, Ltd., HPLC grade, stabilizer free) as an eluent at a flow rate of 1 mL min^{-1}. The chromatograms were monitored by the absorption at 280 nm with a diode array detector.

Fourier Transform Infrared Spectroscopy (FT-IR). Infrared (IR) spectra were recorded on a JASCO FT/IR-4700 Fourier transform infrared spectrometer with an attenuated total reflectance (ATR) unit.

Results

Fabrication of Nanowires from SBF Derivatives. The chemical structures of SBF, 2Br-SBF, 4Br-SBF, 2,2'Br_2-SBF, 2,7Br_2-SBF, Br_4-SBF, SBF_2, and SBF_3 are shown in **Figure 2a**. These compounds showed fluorescence in the solid state (**Figure 2b** and **2c**) with high quantum efficiencies.[8] The photoluminescence energy was reported to exhibit strong dependence on the linkage patterns of SBFs.[34] Here, two regioisomers, 2Br-SBF and 4Br-SBF, were examined based on the substitution patterns of bromine, along with the pristine SBF. In addition, two isomers, 2,2'Br_2-SBF and 2,7Br_2-SBF, and a higher-brominated derivative Br_4-SBF were chosen as the target materials. The formation of intermolecular linkages among the SBFs is expected within the confined cylindrical area during the STLiP processes. To achieve STLiP, the solubility of the polymerized products is critically important; much lower solubility of polymers compared to that of the monomer is appropriate for the isolation of nanowires by the development process. Prior to the irradiation experiments, the solubilities of SBF, SBF_2, and SBF_3 were tested, and the results are summarized in **Table 1**. It is clear that

oligomerization of SBF causes remarkably reduced solubility in both toluene and $CHCl_3$. Although the reactions triggered by high-energy charged particles are not site-selective oligomerization at the 2 or 7 positions of SBF, the reduction in solubility suggests sufficient applicability of the SBF derivatives to the STLiP method. To demonstrate the applicability of STLiP, the thin films of the SBF derivatives were exposed to 350 MeV $^{129}Xe^{26+}$ ions at the fluence of 1×10^{10} cm^{-2} under vacuum, followed by development with toluene.

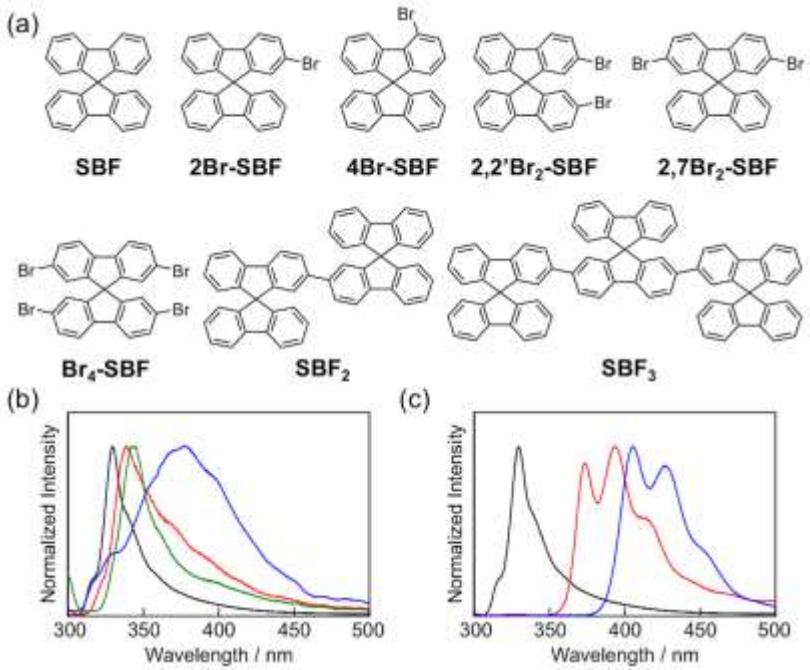

Figure 2. (a) Molecular structures of 9,9′-spirobi[9*H*-fluorene] derivatives. Fluorescent spectra in solid states (λ_{ex} = 250 nm) of (b) SBF (black), 2Br-SBF (red), 4Br-SBF (blue), and Br_4-SBF (green) and (c) SBF (black), SBF_2 (red), and SBF_3 (blue).

Table 1. Solubility (mg/cm^3) data of SBF, SBF_2, and SBF_3 in $CHCl_3$ and toluene.

	$CHCl_3$	Toluene
SBF	70	47
SBF_2	20	2
SBF_3	18	15

Simulation of Particle Trajectories. The value of LET, representing the magnitude of the energy deposited along unit trajectory length, was simulated by using the Monte-Carlo code (SRIM2008) based on the differential cross-section of the particle in a matter based on the densities of the SBF derivatives presumed from their crystalline structures;[29–33] this yielded the value of LET as 11000–12000 eV nm^{-1}. **Figure S1** represents the dependence of LET along the trajectory of an incident particle, suggesting a small deviation from the top to bottom of the film at ~10 μm thickness, and **Figure S2** indicates subsequent straightforward trajectories orthogonal to the substrate plane.

Microscopic Observation of Nanowires. After development, the morphology, shape, and size were studied by AFM. As clearly shown in **Figure 3**, all the compounds yielded clear nanowires with uniform diameters. The uniform size of the nanowires was unchanged over a variety of development conditions that include immersion time and solvents. Particularly, even with the use of strongly solubilizing $CHCl_3$ for 1 h, no obvious fragmentation was observed, suggesting that the SBFs are interconnected in the nanowires, as presented in the AFM images (**Figure S3**). The unchanged morphology of the pattern is typical of cross-linked negative resist materials, and is suggestive of gelation of the polymerized SBFs in the present nanowires with negligible solubility in any type of solvent. The observed number density of nanowires was consistent with the fluence of high-energy charged particles. The length of the nanowires was uniform and corresponded to the thickness of the initial films. These number density and length of the nanowires indicate that the intra-track simultaneous polymerization/crosslinking reactions are responsible for the formation of each nanowire; one particle yielding one corresponding nanowire. To achieve nanowire assembly networks and maximize the surface area, the number density of the nanowires was increased up to 1×10^{11} cm^{-2}. The observed nanowires were partially bundled but still isolated from one another, forming assembled nanowire thin films, as evidenced in **Figure 4**.

Evaluation of Cross-Sectional Radii of Nanowires. The important morphological characteristic of Br_4-SBF-based nanowires is the rigid and straight shape (**Figure 3**). The nanowire cross-sectional radius was examined by AFM. In the height profiles of an individual nanowire (**Figure S4**), the half-width (r_w) and half-height (r_h) of the cross-section of the nanowires were evaluated. By applying the ellipsoidal model, the nanowire radius (r) was defined as $r = (r_w r_h)^{1/2}$. **Figure 5** shows the distribution of the radii of 30 nanowires as observed in the microscopic frame of each compound.

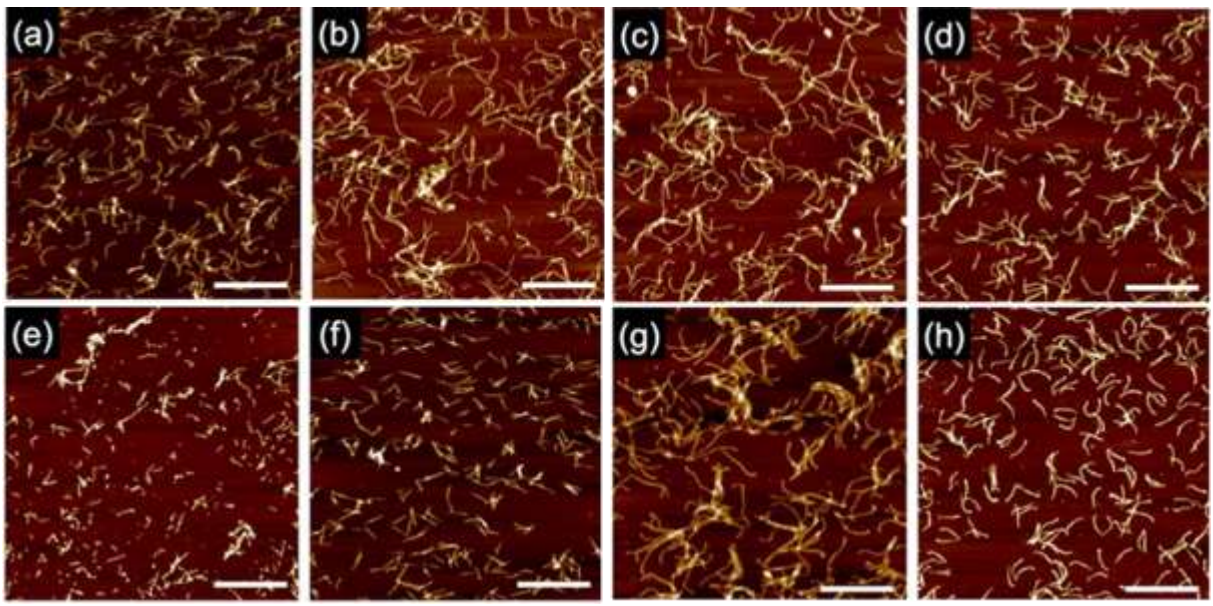

Figure 3. AFM topographic images of nanowires from dropcast films of (a) SBF, (b) 2Br-SBF, (c) 4Br-SBF, (d) 2,2'Br_2-SBF, (e) 2,7Br_2-SBF, (f) Br_4-SBF, (g) SBF_2, and (h) SBF_3. The films were irradiated by 350 MeV $^{129}Xe^{26+}$ particles at a fluence of 1.0×10^{10} cm^{-2} and developed by toluene at room temperature. Scale bars represent 500 nm.

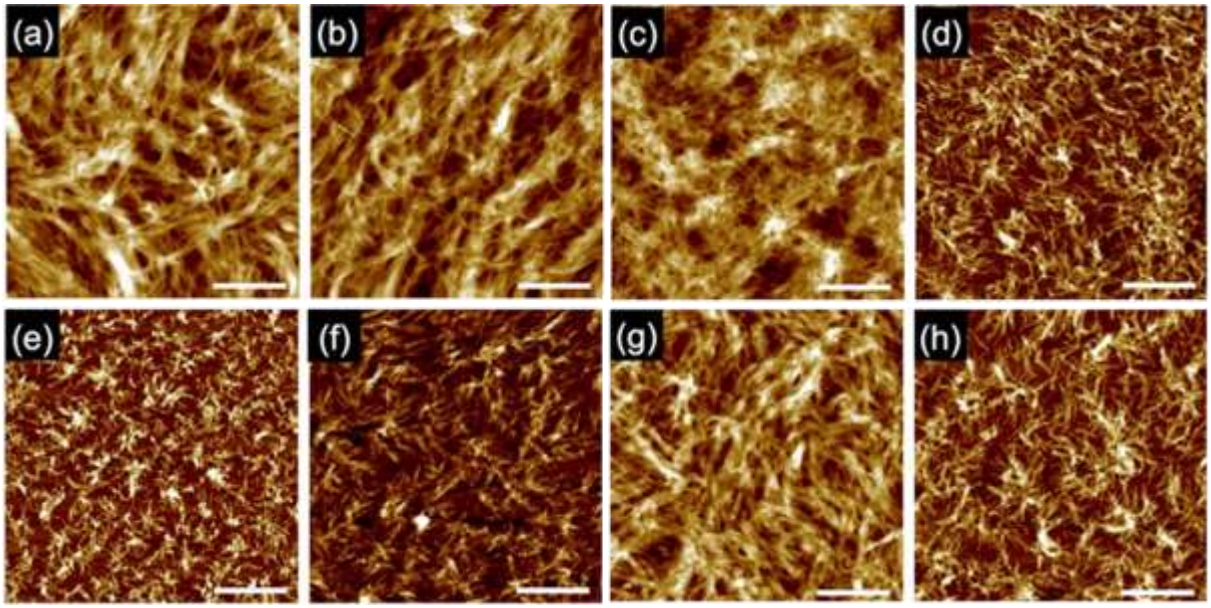

Figure 4. AFM topographic images of bundled nanowires from dropcast films of (a) SBF, (b) 2Br-SBF, (c) 4Br-SBF, (d) 2,2'Br_2-SBF, (e) 2,7Br_2-SBF, (f) Br_4-SBF, (g) SBF_2, and (h) SBF_3. The films were irradiated by 350 MeV $^{129}Xe^{26+}$ particles at a fluence of 1.0×10^{11} cm^{-2} and developed by toluene at room temperature. Scale bars represent 500 nm.

Table 2. Summary of density, calculated maximum radial range r_c and r_p, calculated linear energy transfer (LET), radii in nanowire form $r_{nanowire}$, calculated energy density at the nanowire radii ρ_s, estimated molecular volume $V_{molecule}$, given energy per molecule by high-energy ions $E_{molecule}$, and estimated G for SBF, 2Br-SBF, 2,2'Br-SBF, Br_4-SBF, SBF_2, and SBF_3 upon irradiation with 350 MeV $^{129}Xe^{26+}$.

	Density / g cm^{-1}	LET / eV nm^{-1}	r_c / nm	r_p / nm	$r_{nanowire}$ / nm	ρ_s / eV nm^{-3}	$V_{molecule}$ / nm^3	$E_{molecule}$ / eV	G value / $(100\ eV)^{-1}$
SBF	1.25[a]	11500	0.77	296	3.93	9.18	0.42	3.86	8.6
2Br-SBF	1.48[b]	12000	0.77	250	4.47	7.61	0.45	3.42	9.7
2,2'Br_2-SBF	1.63[a]	12000	0.79	227	4.56	7.45	0.48	3.57	9.3
Br_4-SBF	1.84[a]	12000	0.83	201	4.81	6.90	0.54	3.72	9.0
SBF_2	1.34[a]	12000	0.75	276	4.35	7.87	0.78	6.14	5.4
SBF_3	1.24[a]	11000	0.78	298	4.48	6.76	1.27	8.58	3.9

[a] Presumed from reported crystalline structures (Ref. 29–33). [b] Speculated.

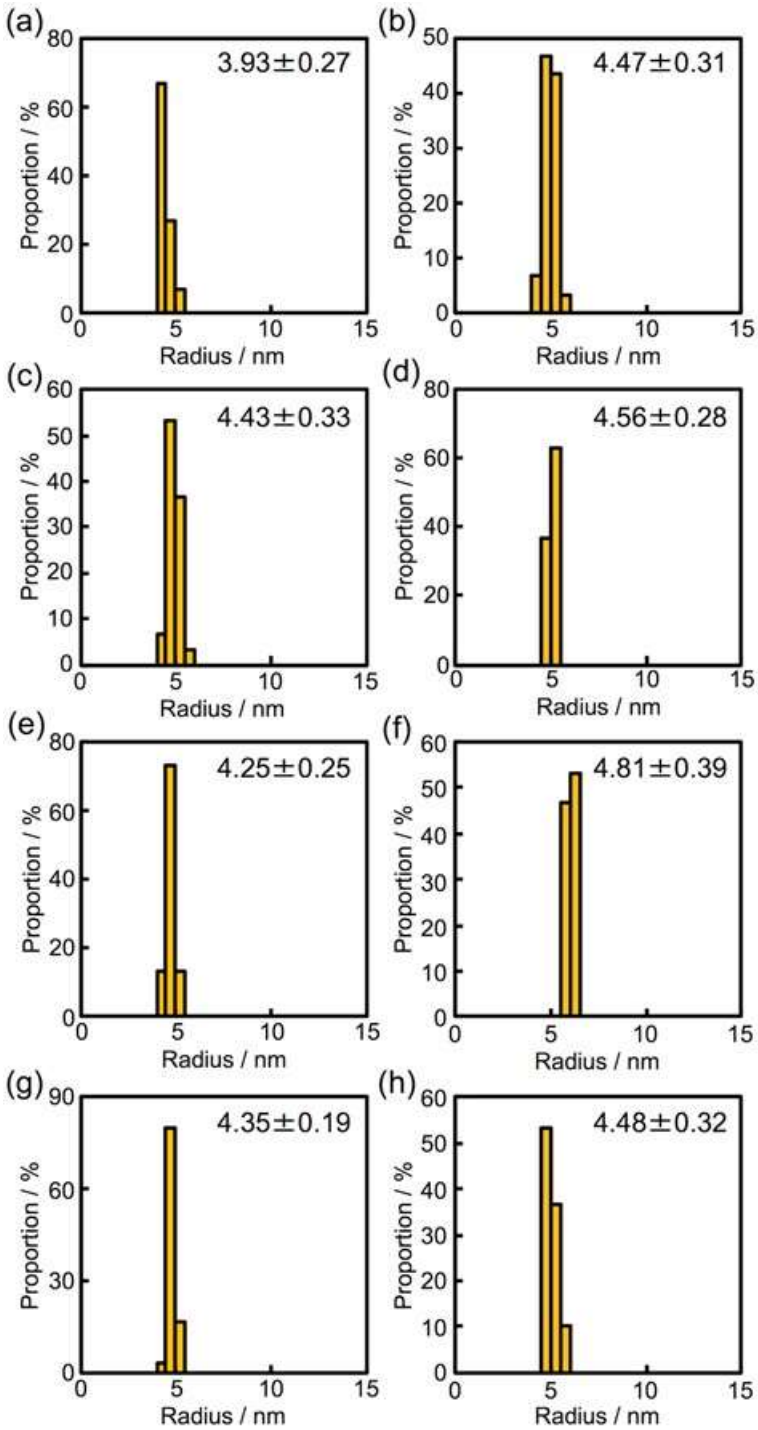

Figure 5. Radius distributions and average radius of nanowires from dropcast films of (a) SBF, (b) 2Br-SBF, (c) 4Br-SBF, (d) 2,2'Br_2-SBF, (e) 2,7Br_2-SBF, (f) Br_4-SBF, (g) SBF_2, and (h) SBF_3. The radius was calculated by $r = (r_w r_h)^{1/2}$ values estimated from AFM cross-sectional profiles for individual 30 nanowires.

Analysis of Polymerized Products by SEC and FT-IR. SEC analysis was performed to confirm the polymerization reactions to give products with higher excluded volumes. After irradiation with 350 MeV $^{129}Xe^{26+}$ particles at the fluence of 1×10^{11} cm^{-2}, films of SBF were developed with toluene to isolate the nanowires. The nanowires were removed from the substrates by sonicating the substrates in THF. The THF solution was filtered through PTFE membrane and concentrated, and then subjected to SEC analysis. Although insoluble fractions were excluded by the filtration process, soluble products with the higher excluded volumes were detected in SEC (**Figure S5**), indicating the fact of polymerization reaction by heavy ion irradiations. Presence of peaks with a longer retention time than that of SBF implies that bond-breaking reactions are also occurred by irradiations. FT-IR measurements of SBF nanowires on a substrate were carried out to know the chemical bond information of the nanowires. However, due to the limitation of the sensitivity, it was difficult to obtain significant spectra as nanowire forms (**Figure S6**).

Fabrication of Nanowires from SBF Derivatives by Using Lower Energy Particles. To support the reactivity difference depending on the presence/absence of Br atoms, lower-energy particle irradiation experiments were also performed using Al cluster ions with a variety of LET but constant velocity to modulate the radial energy distribution in the particle track.[35] 1.5 MeV $^{27}Al^{+}$, 3.0 MeV $^{27}Al_2^{+}$, 4.5 MeV $^{27}Al_3^{+}$, and 6.0 MeV $^{27}Al_4^{+}$ cluster ions at the fluence of 1.0×10^{9} cm^{-2} were irradiated and then developed using toluene. It was disclosed that irradiation with 6.0 MeV $^{27}Al_4^{+}$ afforded nanowires for the cases of 2Br-SBF, Br_4-SBF, and SBF_2, while no nanowire was observed with 1.5 MeV $^{27}Al^{+}$ irradiation (**Figure 6**). When focusing on the results of 3.0 MeV $^{27}Al_2^{+}$ and 4.5 MeV $^{27}Al_3^{+}$ irradiation, only 2Br-SBF among the three compounds exhibited low efficiency for nanowire formation. The present results are consistent with the evaluation of radii, where Br_4-SBF revealed the highest capability of nanowire formation.

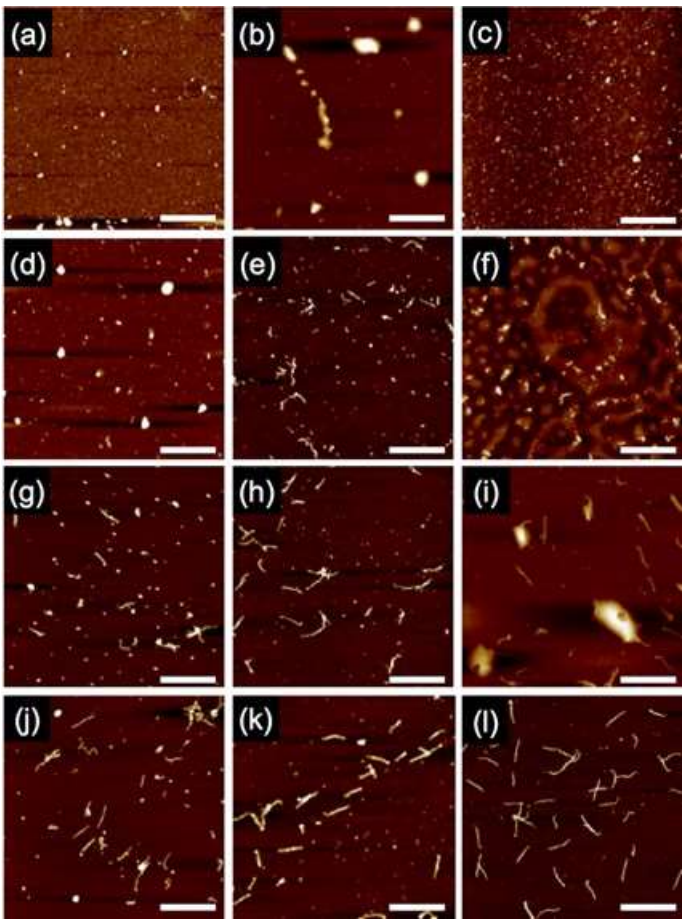

Figure 6. AFM topographic images of nanowires from dropcast films of (a,d,g,j) 2Br-SBF, (b,e,h,k) Br_4-SBF, and (c,f,i,l) SBF_2. The films were irradiated by (a–c) 1.5 MeV Al^+, (d–f) 3.0 MeV Al_2^+, (g–i) 4.5 MeV Al_3^+, (j–l) 6.0 MeV Al_4^+ particles at a fluence of 1.0×10^9 cm^{-2} and developed by toluene at room temperature. Scale bars represent 500 nm.

X-Ray Photoelectron Spectroscopy Measurements. The chemical reactions triggered by high-energy charged particles were investigated by XPS. Photoelectrons were detected in both the film and nanowires, as seen in **Figure 7**. Non-irradiated films yielded peak intensity ratios of about 0.11, 0.24, and 0.48 for Br-SBFs, Br_2-SBFs, and Br_4-SBF, respectively, which explains well the bromine contents of the compounds.

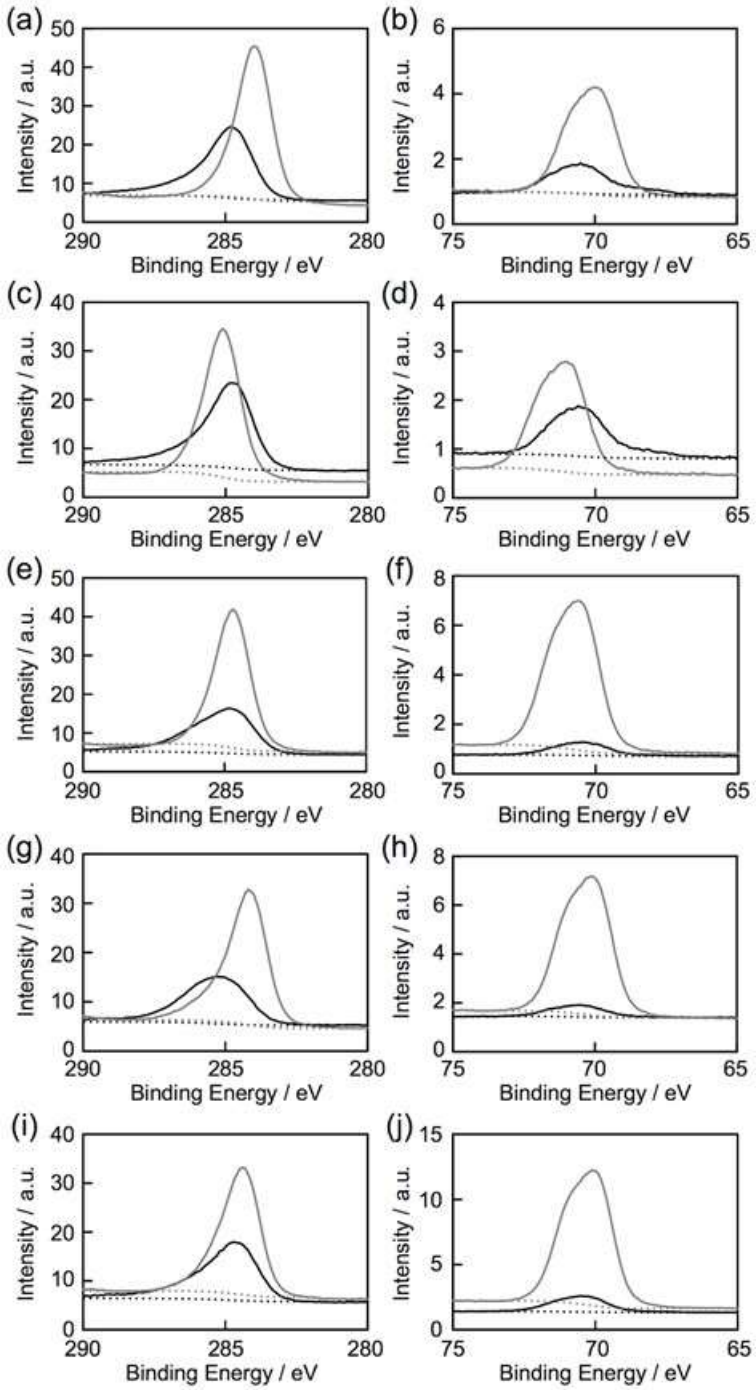

Figure 7. (a,c,e,g,i) C 1s and (b,d,f,h,j) Br 3d X-ray photoelectron spectra for non-irradiated films (gray) and nanowires (black) fabricated from (a,b) 2Br-SBF, (c,d) 4Br-SBF, (e,f) 2,2'Br_2-SBF, (g,h) 2,7Br_2-SBF, and (i,j) Br_4-SBF. Dotted lines represent baselines for films (gray) and nanowires (black).

Table 3. Observed signal intensity ratio of (Br 3d)/(C 1s) in X-ray photoelectron spectra for films and nanowires.

	Film	Nanowire
2Br-SBF	0.11	0.056
4Br-SBF	0.10	0.068
2,2'Br_2-SBF	0.23	0.046
2,7Br_2-SBF	0.24	0.042
Br_4-SBF	0.48	0.094

Photoluminescence Spectroscopy Measurements. The fluorescence spectra of SBF-based nanowires were recorded as shown in **Figure 8**. The emission bands at 330–380 nm of the starting compounds (**Figure 2b**) disappeared in the case of the nanowires at the fluence of 10^{11} cm^{-2} under irradiation with 350 MeV $^{129}Xe^{26+}$ ions. Instead, bands at around 280 nm and 470 nm appeared for the nanowires based on mono-SBF derivatives (**Figure 8a** and **8b**). The photoluminescence intensity is proportional to the fluence of the incident particles (**Figure 8a**), which reflects the number density of the isolated nanowires without any indirect energy relaxation process within the nanowire networks at the density of 10^{11} cm^{-2}; the highly dense state is seen in **Figure 4**. In the case of SBF_2 and SBF_3, an additional band at 350–450 nm was observed that corresponds to the initial compounds (**Figure 8c** and **2c**).

When the nanowires on the silicon substrate were placed in a glass cell filled with cyclohexane, similar characteristic photoluminescence bands were observed in the fluorescence spectra (**Figure 8d**, black). A drop of nitrobenzene was added to cyclohexane (c_{NB} = 2.0 × 10^{-3} M),

and again the photoluminescence spectrum was recorded. Consequently, an obvious quenching of the emission band was observed (**Figure 8d**, red).

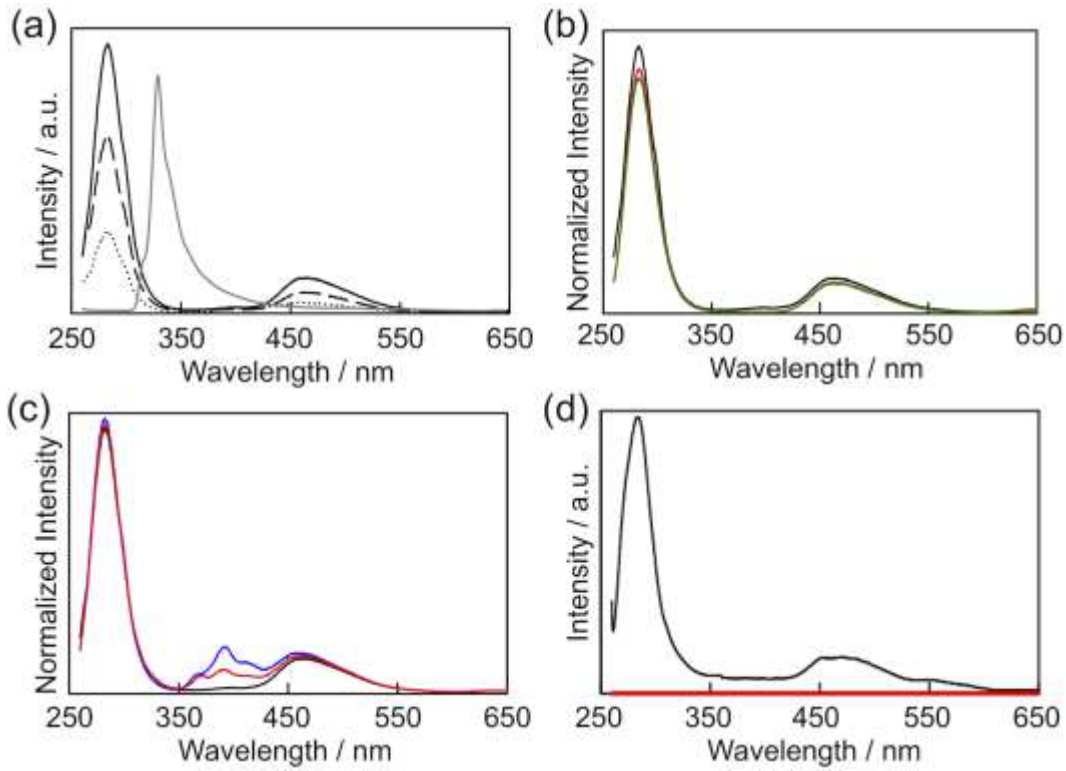

Figure 8. Fluorescence spectra of (a) SBF (gray, solid) and nanowires fabricated from SBF at the fluence of 1.0×10^{11} cm^{-2} (black, dotted), 2.3×10^{11} cm^{-2} (black, dashed), and 5.0×10^{11} cm^{-2} (black, solid). Fluorescence spectra of nanowires fabricated from (b) SBF (black), 2Br-SBF (red), and Br_4-SBF (green) and (c) SBF (solid), SBF_2 (red), and SBF_3 (blue). Fluorescence spectra of nanowires of SBF in cyclohexane (black) and cyclohexane containing 2 mM nitrobenzene (red).

Conductivity Measurements. FP-TRMC measurements were performed using nanowires of SBF on a quartz plate. **Figure 9** shows the typical conductivity transient profiles upon photoexcitation at 355 nm at the photon density of 9.1×10^{15} cm^{-2} pulse^{-1}. The nanowire film of SBF indicated a clear rise–decay profile with photogeneration of charge carriers and their gradual recombination/trapping. The blue and green curves shown in **Figure 9** correspond to the conductivity signals of the SBF nanowires, where the maximum conductivity value, $(\phi\sum\mu)_{max}$, recorded is $3.5–4.0 \times 10^{-9}$ m^2 V^{-1} s^{-1}. On the other hand, under saturated vapors of nitrobenzene (2.0×10^2 ppm), the $(\phi\sum\mu)_{max}$ value increased up to 9.5×10^{-9} m^2 V^{-1} s^{-1} (red curve).

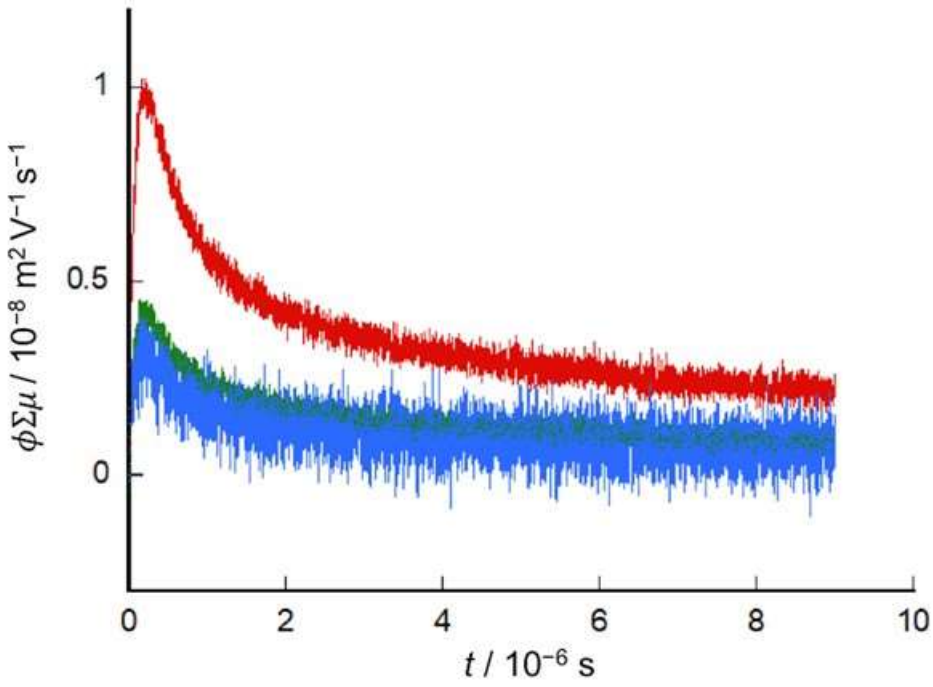

Figure 9. Transient conductivity for SBF-based nanowires soon after exposure to nitrobenzene vapor (green), under saturated nitrobenzene vapor at concentration of 2.0×10^2 ppm (red), and under air (blue) upon exposure to 355 nm pulses at 9.1×10^{15} photons cm^{-2} pulse^{-1}. Nanowires were fabricated by irradiation with 350 MeV $^{129}Xe^{26+}$ particles at a fluence of 1.0×10^{11} cm^{-2}.

Discussion

The cross-sectional radii of the nanowires are correlated with the efficiency of the polymerization/crosslinking reaction. Based on **Figure 5**, the increasing order of radii was revealed as r(SBF) < r(2,7Br_2-SBF) < r(2Br-SBF) ~ r(4Br-SBF) < r(2,2'Br_2-SBF) < r(Br_4-SBF) and r(SBF) < r(SBF_2) < r(SBF_3). The author presumed that the larger r observed in Br-substituted SBFs is due to the highly efficient bond-formation reactions, including the dissociative electron attachment of the generated secondary electrons to the halogenated compounds.[36–38] The order of non-halogenated SBFs can be interpreted in terms of the effect of molecular size on the oligomerization/crosslinking reactions; the starting larger oligomers reach the polymerized products more easily. However, the difference between r(SBF_2) and r(SBF_3) was small, indicating this effect is saturated at a certain size of the molecules with similar reactive sites. In addition, 2,7Br_2-SBF resulted in nanowires with smaller diameters compared to those from 2Br-SBF. This indicates the importance of substitution patterns in changing the electronic state of the monomer, and thus, altering the polymerization efficiency upon irradiation with high-energy charged particles. The other important finding is the narrow distribution of the nanowire radii compared with those produced from polymer films.[15–21] A possible reason is the much smaller molecular volumes of the SBF derivatives compared to those of the polymer chains with polydispersity. The sharp threshold of reaction efficiency, corresponding to r, is considered to appear due to this reason.

In the STLiP method, the cross-sectional radii of the nanowires should be related to the initiation/propagation efficiency of the monomer molecules triggered by the given energy of the incident high-energy particles. The intra-track radial energy density, defined in terms of the collision of incident particles with target materials, is mainly classified into two regions––the "core" and "penumbra."[39–42] The "core" is a narrow central circular zone with a radius of

a few nanometers, where extremely high energy deposition occurs, dominated by the knock-on collision processes between the incident particles and the atoms of the target material. The deposited energy is mainly associated with the process of plasma oscillation of the electrons ejected due to primary ionizations, as well as direct electronic excitation.

The size of the core is defined as the spatial region of plasma oscillations induced by the interactions between a high-energy charged particle and the target material, assuming uniform electron density (n) in the material. The plasma oscillation frequency (Ω) is given by

$$\Omega = \left(\frac{ne^2}{m\varepsilon_0} \right)^{1/2} \quad (2),$$

where m and ε_0 denote the mass of the electron and the permittivity of free space, respectively. For example, SBF has a density of ~1.25 × 10^3 kg m^{-3} [29] and the number of electrons in the outermost shell of SBF is 116. Based on these parameters, the value of Ω is calculated as 2.96 × 10^{16} s^{-1}. The energy of all the incident charged particles (E) employed is in the range of non-relativity. Thus, the velocity (v) of the particle is given by the following equation.

$$E \cdot e = \frac{1}{2} m_p v^2 \quad (3),$$

where m_p is the mass of the incident particle. The calculated v of 2.28 × 10^7 m s^{-1} for 350 MeV ^{129}Xe particle is confirmed to be under 10% of c (the speed of light). In contrast, the value of v is larger than the Bohr orbital velocity, suggesting that the Xe particles are swift heavy ions whose energy loss process is mainly dominated by inelastic scattering with ionization. As a result, r_c is given in terms of Ω and v as

$$r_c = \frac{v}{\Omega} \quad (4)$$

.

The value of r_c is estimated as 0.75–0.83 nm for the SBF derivatives (**Table 2**), which is much smaller than the observed nanowire radii. This is suggestive of the crucial role of radial-energy density in the penumbra region, rather than the density in the core region, in determining nanowire radii.

The "penumbra" is a peripheral zone with radius ranging from nanometers to micrometers, where energy deposition occurs mainly through ionization events caused by energetic secondary electrons (δ-rays) released by the incident charged particle from the center of the "core." The energy spectra of the generated δ-rays are theoretically predictable.[41,42] The maximum radial range values, r_p, summarized in **Table 2**, are based on the densities of the SBF derivatives used. The radial energy distribution in the penumbra region (ρ_p (r)) follows the inverse square rule and is described by the following equation.[41]

$$\rho_p(r) = \frac{LET}{2\pi r^2 \left\{1 + 2 \cdot \ln\left(\frac{r_p}{r_c}\right)\right\}} \quad (5),$$

where the LET values are almost constant for each depth (**Figure S1**). Based on eq. 5, the energy density at the surface of the nanowires, ρ_s, is calculated by using the radius of each nanowire (**Figure 5**), and has been summarized in **Table 2**. The given energy per molecule around the nanowire surface is also summarized in **Table 2**, calculated from ρ_s and molecular volumes, which are in turn estimated from the crystal structures of the SBF derivatives.[29–33] At the nanowire surface, at least one chemical bond is likely formed to immobilize the molecule. One SBF molecule is surrounded by six nearest neighbor molecules capable of bond formation based on the reported crystal structures, and the SBF molecule should react with either of the three inner molecules to be immobilized to a nanowire. The G values for bond formation with the inner nearest neighbors are roughly estimated to be in the range of 8.6–9.7 $(100\ \text{eV})^{-1}$ for

the monomeric SBF derivatives upon 350 MeV ^{129}Xe particle irradiation, whereas the dimer and trimer yielded smaller *G* values of 5.4 and 3.9 $(100\ eV)^{-1}$, respectively. These values are larger than that for the case of the polymer, revealing efficient solid-state polymerization of the SBF derivatives upon high-energy particle irradiation. The lower values observed for oligomeric SBF_2 and SBF_3 can be interpreted as a hypothesis that a larger molecular volume can result in nanowires with a smaller reaction efficiency. Since brominated SBFs afford larger *r* values but reveal similar *G* values with non-brominated SBF along the radial distance of their nanowire surfaces, it is clear that bromination of the SBF rings resulted in higher efficiencies of the polymerization reactions. Note that the high electron density on the Br atoms has already been taken into account for the value of deposited energy density.

XPS was performed to prove that the efficient chemical reactions were triggered by high-energy charged particles in brominated SBF-based nanowires. XPS measurements focused on the electrons of the C 1s and Br 3d orbitals and compared the ratio of their intensities for the starting film and the isolated nanowires. **Table 3** summarizes the observed peak area ratios of (Br 3d)/(C 1s). It was revealed that the ratios for the nanowires were almost 50% those of the non-irradiated films in the case of 2Br-SBF and 4Br-SBF. Notably, the ratio significantly dropped off for the nanowires of 2,2'Br_2-SBF and 2,7Br_2-SBF, revealing about 20% of the peak intensity ratio of (Br 3d)/(C 1s). In the case of Br_4-SBF also, about 20% of the peak ratio was recorded, suggesting that non-negligible numbers of Br atoms were dissociated and escaped from the wires as HBr, Br_2, or other small molecular weight bromine compounds during the irradiation or development process. The Br atoms were actually detached from the SBF cores efficiently removed by swift heavy ion irradiation, which generated the reactive species efficiently to form new covalent bonds. This is reasonable considering the lower bond energy of C_6H_5–Br (~336 kJ mol^{-1}) compared to that of C_6H_5–H

(~472 kJ mol^{-1})[43]. It is revealed that bromination of aromatic structures serves as an effective design strategy for nanowire fabrication by the STLiP method.

In fluorescence spectroscopy, the observed red-shifted emission band at around 460 nm suggested the formation of extended conjugated structures due to the reactions triggered by the high-energy charged particle irradiation. By utilizing the fluorescence property of the SBF-based nanowires, the detection of hazardous substances was demonstrated using nitrobenzene as an example. The fluorescence from the SBF nanowires was obviously quenched by the addition of nitrobenzene. This phenomenon is essentially reversible, as The author confirmed a recovery of the emission band after several rinses of the nanowires using cyclohexane and measuring the fluorescence spectra in cyclohexane itself. Considering that fluorescence quenching by a nitrobenzene moiety is often utilized in bioimaging research fields,[44,45] an identical mechanism should operate in present system. The complete recovery of the fluorescence through the simple rinse procedure involving common electronically neutral solvents suggests the compatibility of reproducibility and high sensitivity due to the extremely high surface area of the nanowires. Thus, fluorescent nanowire systems are promising for sensing applications.

Expecting amperometric or conductometric outputs from the nanowire networks, the intrinsic electrical conductivity of the nanowires was determined by FP-TRMC, which is a contactless microwave technique.[46] Under nitrobenzene saturated vapor condition (~200 ppm), the observed conductivity signal increased up to 2.5 fold. It indicates the improved charge carrier generation between the donor (SBF nanowires) and acceptor (nitrobenzene) materials. Conjugated nanowires fabricated by STLiP method would open up the possibility of using conductivity-based sensing systems.

The fluorometric and conductometric dual outputs from the present nanowire system secure the wide dynamic range of analyte concentrations from the parts-per-million to percentage level for sensing, and both the metric systems are demonstrated herein as non-contact quantitative protocols for fluorescence spectroscopy and microwave-based conductivity measurements.

Conclusion

SBF-based polymerized nanowires were fabricated by the irradiation of their films with high-energy charged particles, followed by their isolation process using toluene. The isolated nanowires display uniform lengths and cross-sectional radii, and showed sufficient tolerance to organic solvent treatment. The cross-sectional radii of the nanowires were correlated with intra-track reaction efficiency that can be increased by bromination of the aromatic cores of the starting molecules. Based on a combination of theoretical approaches on energy deposition in ion tracks and the molecular arrangements expected from their crystalline packings, the reaction efficiency (*G* value) was estimated as 8.6–9.7 $(100\ \mathrm{eV})^{-1}$ for monomeric SBF derivatives upon irradiation with 350 MeV ^{129}Xe ions. The obtained nanowires showed emission bands red-shifted from those of the starting SBF molecules, suggesting the formation of extended aromatic structures by covalent bond formation via polymerization reactions. Owing to this conjugated character, the fabricated SBF-based nanowires allow to detect electron-deficient analytes via fluorescence quenching and observed photoconductivity. The demonstrated strategy for nanowire fabrication from small soluble aromatic compounds with fluorescence and electric conductive capability is useful for producing nanomaterials from various small molecules.

References

(1) Grimsdale, A. C.; Müllen, K. *Macromol. Rapid Commun.* **2007**, *28*, 1676–1702.

(2) Abbel, R.; Schenning, A. P. H. J.; Meijer, E. W. *J. Polym. Sci. A Polym. Chem.* **2009**, *47*, 4215–4233.

(3) Scherf, U.; List, E. J. W. *Adv. Mater.* **2002**, *14*, 477.

(4) Zhao, Q.; Liu, S. J.; Huang, W. *Macromol. Chem. Phys.* **2009**, *210*, 1580–1590.

(5) Xie, L. H.; Yin, C. R.; Lai, W. Y.; Fan, Q. L.; Huang, W. *Prog. Polym. Sci.* **2012**, *37*, 1192–1264.

(6) Clarkson, R. G.; Gomberg, M. *J. Am. Chem. Soc.* **1930**, *52*, 2881–2891.

(7) Weisburger, J. H.; Weisburger, E. K.; Ray, F. E. *J. Am. Chem. Soc.* **1950**, *72*, 4253–4255.

(8) Saragi, T. P. I.; Spehr, T.; Siebert, A.; Fuhrmann-Lieker, T.; Salbeck, J. *Chem. Rev.* **2007**, *107*, 1011–1065.

(9) Teh, C. H.; Daik, R.; Lim, E. L.; Yap, C. C.; Ibrahim, M. A.; Ludin, N. A.; Sopian, K.; Teridi M. A. M. *J. Mater. Chem. A* **2016**, *4*, 15788–15822.

(10) Thomas, S. W.; Joly, G. D.; Swager, T. M. *Chem. Rev.* **2007**, *107*, 1339–1386.

(11) Chan, Y.-H. Wu, P-J. *Part. Part. Syst. Charact.* **2015**, *32*, 11–28.

(12) Sun, X.; Wang, Y.; Lei, Y. *Chem. Soc. Rev.* **2015**, *44*, 8019–8061.

(13) Isaa, N. M.; Baharina, R.; Majid, R. A. Rahman, W. A. *Polym. Adv. Technol.* **2017**, *28* 1559–1571.

(14) Wu, W. Bazan, G. C. Liu, B. *Chem* **2017**, *2*, 760–790.

(15) Seki, S.; Maeda, K.; Tagawa, S.; Kudoh, H.; Sugimoto, M.; Morita, Y.; Shibata, H. *Adv. Mater.* **2001**, ***13***, 1663–1665.

(16) Tsukuda, S.; Seki, S.; Tagawa, S.; Sugimoto, M.; Idesaki, A.; Tanaka, S.; Oshima, A. *J. Phys. Chem. B* **2004**, *108*, 3407–3409.

(17) Tsukuda, S.; Seki, S.; Sugimoto, M.; Tagawa, S. *J. Phys. Chem. B* **2006**, *110*, 19319–19322.

(18) Seki, S.; Saeki, A.; Choi, W.; Maeyoshi, Y.; Omichi, M.; Asano, A.; Enomoto, K.; Vijayakumar, C.; Sugimoto, M.; Tsukuda, S.; Tanaka. *J. Phys. Chem. B* **2012**, 116, 12857–12863.

(19) Asano, A.; Omichi, M.; Tsukuda, S.; Takano, K.; Sugimoto, M.; Saeki, A.; Seki, S. *J. Phys Chem. C* **2012**, *116*, 17274–17279.

(20) Wasin, T.; Enomoto, K.; Sakurai, T.; Padalkar, V. S.; Cheng, H. L.; Kikuchi, K.; Hori, Y.; Chiba, A.; Saito, Y.; Kamiya, T.; Sugimoto, M.; Seki, S. *ACS Sens.* **2016**, *1*, 766–774.

(21) Omichi, M.; Asano, A.; Tsukuda, S.; Takano, K.; Sugimoto, M.; Saeki, A.; Sakamaki, D.; Onoda, A.; Hayashi, T.; Seki, S. *Nat. Commun.* **2014**, *5*, 3718.

(22) Maeyoshi, Y.; Saeki, A.; Suwa, S.; Omichi, M.; Marui, H.; Asano, A.; Tsukuda, S.; Sugimoto, M.; Kishimura, A.; Kataoka, K.; Seki, S. *Sci. Rep.* **2012**, *2*, 600.

(23) Takeshita, Y.; Sakurai, T.; Asano, A.; Takano, K.; Omichi, M.; Sugimoto, M.; Seki, S. *Adv. Mater. Lett.* **2015**, *6*, 99–103.

(24) Horio, A.; Sakurai, T.; Lakshmi, G. B. V. S.; Avasthi, D. K.; Sugimoto, M.; Yamaki, T.; Seki, S. *Nanoscale* **2016**, *8*, 14925–14931.

(25) Horio, A.; Sakurai, T.; Padalkar, V. S.; Sakamaki, D.; Yamaki, T.; Sugimoto, M.; Seki, S. *J. Photopolym. Sci. Technol.* **2016**, *29*, 373–377.

(26) Horio, A.; Sakurai, T.; Kayama, K.; Lakshmi, G. B. V. S.; Avasthi, D. K.; Sugimoto, M.; Yamaki, T.; Chiba, A.; Saito, Y.; Seki, S. *Radiat. Phys. Chem.* **2018**, *142*, 100–106.

(27) Kumar, A.; Avasthi, D. K.; Tripathi, A.; Filip, L. D.; Carey, J. D.; Pivin, J. C. *J. Appl. Phys.* **2007**, *101*, 014308.

(28) Kumar, A.; Singh, F.; Pivin, J. C.; Avasthi, D. K. *J. Phys. D. Appl. Phys.* **2008**, *41*, 095304.

(29) Douthwaite, R. E.; Taylor, A.; Whitwood, A. C. *Acta Cryst.* **2005**, *C61*, o328–o331.

(30) Chiang, C.-L.; Shu, C.-F.; Chen, C.-T. *Org. Lett.* **2005**, *7*, 3717–3720.

(31) Guo, A.; Zhu, R. *Acta Cryst.* **2009**, *E65*, o1528.

(32) Ou, C.-J., Zhu, C., Ding, X.-H., Yang, L., Lin, J.-Y., Xie, L.-H., Qian, Y.; Xu, C.-X.; Zhao, J.-F.; Huang, W. *J. Mater. Chem. C* **2017**, *5*, 5345–5355.

(33) Wong, K.-T., Chien, Y.-Y., Chen, R.-T., Wang, C.-F., Lin, Y.-T., Chiang, H.-H., Hsieh, P.-Y.; Wu, C.-C.; Chou, C. H.; Su, Y. O.; Lee, G.-H., Peng, S.-M. *J. Am. Chem. Soc.* **2002**, *124*, 11576–11577.

(34) Sicard, L.; Quinton, C.; Peltier, J. D.; Tondelier, D.; Geffroy, B.; Biapo, U.; Métivier, R.; Jeannin, O.; Rault-Berthelot, J.; Poriel, C. *Chem. Eur. J.* **2017**, *23*, 7719–7727.

(35) Saitoh, Y.; Mizuhashi, K.; Tajima, S. *Nucl. Instrum. Methods Phys. Res. A* **2000**, *452*, 61–66.

(36) Barszczewska, W.; Kočíšek, J.; Skalný, J.; Matejčík, V.; Matejčík, Š. *Int. J. Mass Spectrom.* **2008**, *277*, 103–106.

(37) Modelli, A.; Jones, D. *J. Phys. Chem. A* **2009**, *113*, 7795–7801.

(38) Kim, N.; Sohn, T.; Lee, S. H.; Nandi, D.; Kim, S. K. *Phys. Chem. Chem. Phys.* **2013**, *15*, 16503–16509.

(39) Fleischer, R. L.; Price, P. B.; Walker, R. M. *Science* **1965**, *149*, 383–393.

(40) Chatterjee, A.; Schaefer, H. J. *Radiat. Environ. Biophys.* **1976**, *13*, 215–227.

(41) Magee, J. L.; Chatterjee, A. *J. Phys. Chem.* **1980**, *84*, 3529–3536.

(42) Freeman, G. R. *Kinetics of nonhomogenous processes;* John Wiley & Sons, Tronto, Canada, 1987.

(43) Luo, Y. R. *Comprehensive Handbook of Chemical Bond Energies;* CRC Press, Boca Raton, FL, 2007.

(44) Goodpaster, J. V.; McGuffin, V. L. *Anal. Chem.* **2001**, *73*, 2004–2011.

(45) Meaney, M. S.; McGuffin, V. L. *Anal. Chim. Acta* **2008**, *610*, 57–67.

(46) Seki, S.; Saeki, A.; Sakurai, T.; Sakamaki, D. *Phys. Chem. Chem. Phys.* **2014**, *16*, 11093–11113.

Chapter 1 Appendix

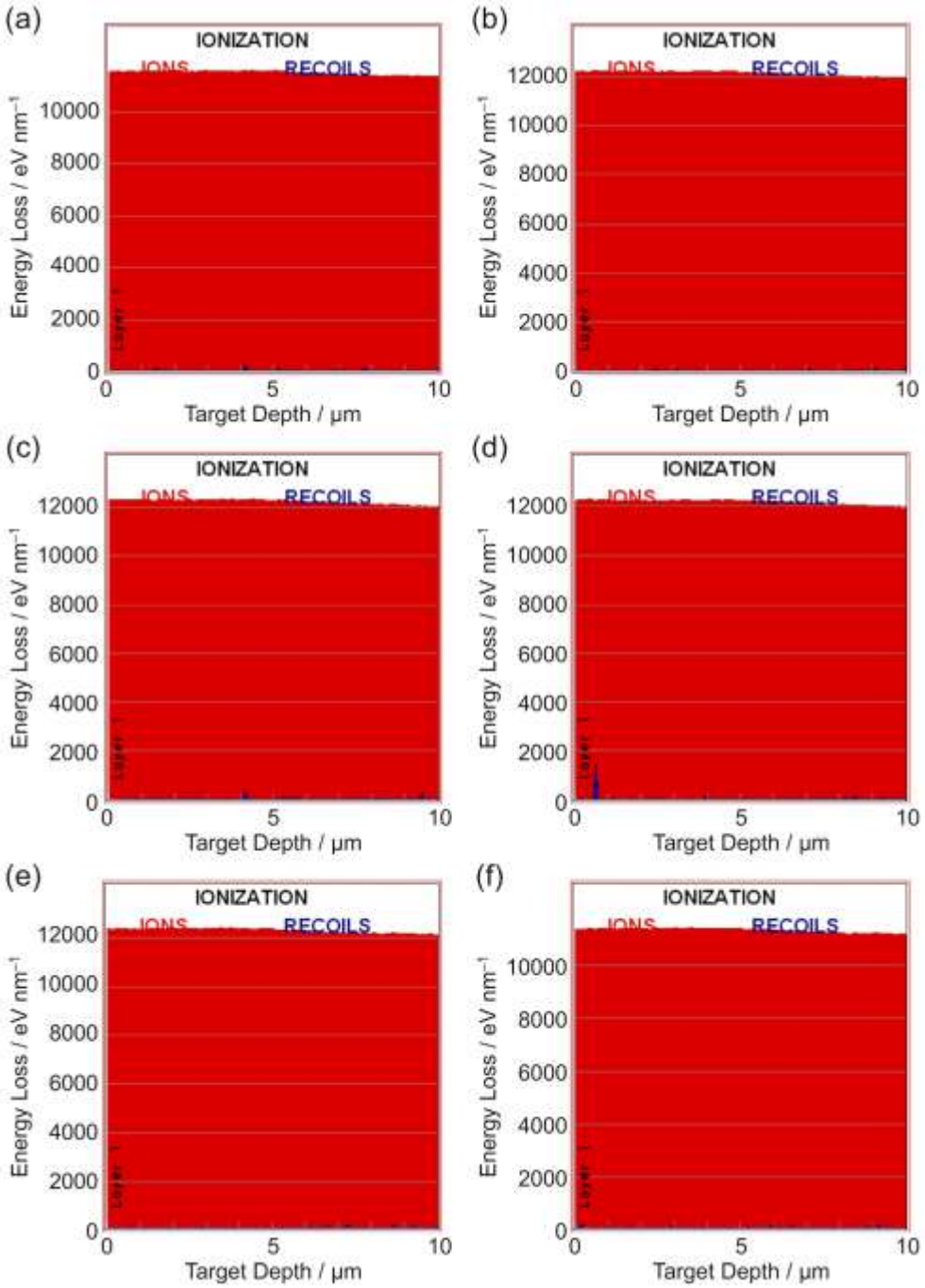

Figure S1. Calculated energy loss (~LET) profiles as a function of target depth for 10-µm thick films of (a) **SBF**, (b) **2Br-SBF**, (c) **2,2'Br$_2$-SBF**, (d) **Br$_4$-SBF**, (e) **SBF$_2$**, and (f) **SBF$_3$** upon 350 MeV ^{129}Xe particles irradiation. Calculation was carried out using SRIM 2008 calculation code.

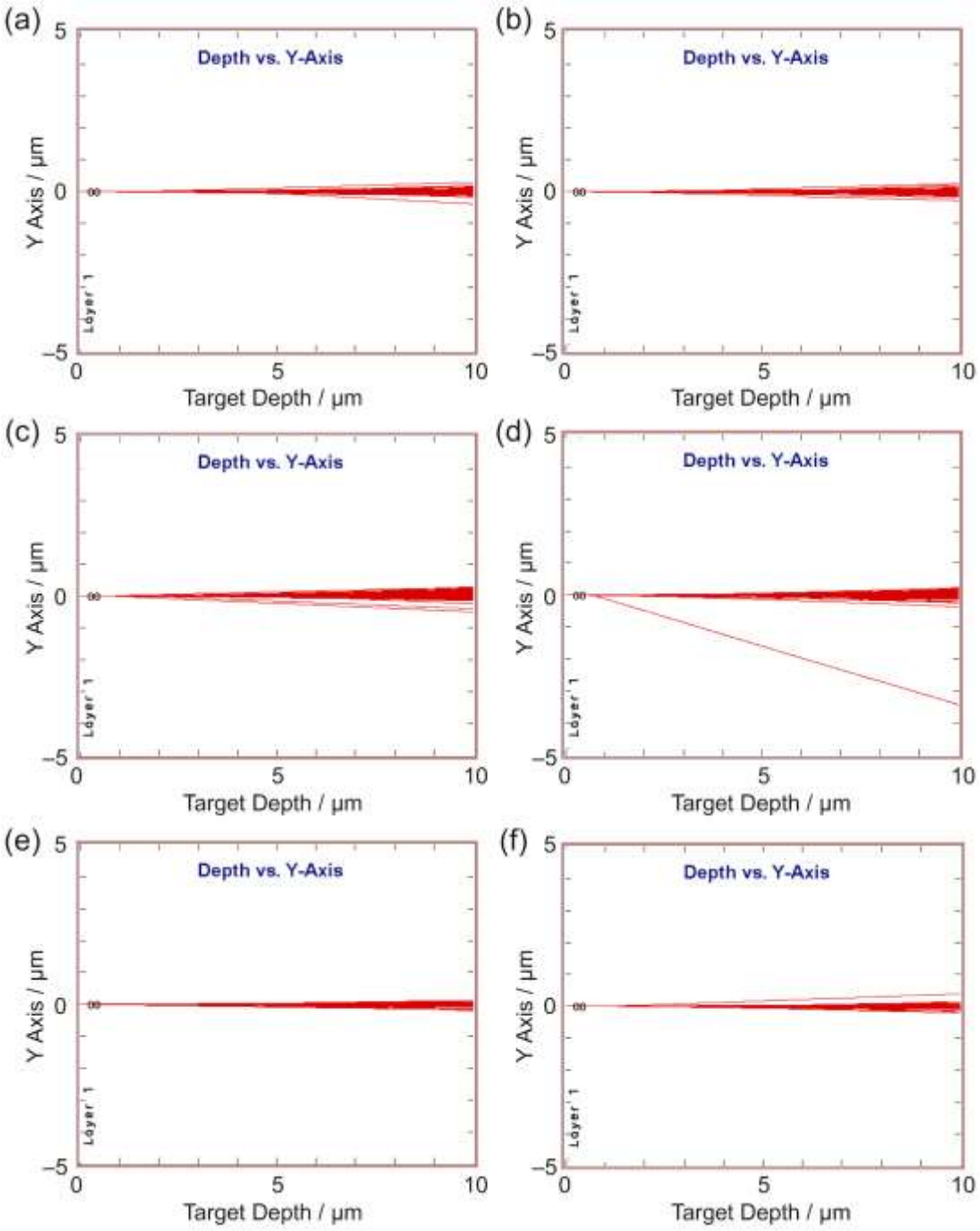

Figure S2. Ion track images of 10-µm thick films of (a) **SBF**, (b) **2Br-SBF**, (c) **2,2'Br$_2$-SBF**, (d) **Br$_4$-SBF**, (e) **SBF$_2$**, and (f) **SBF$_3$** upon 350 MeV ^{129}Xe particles irradiation. Calculation was carried out using SRIM 2008 calculation code.

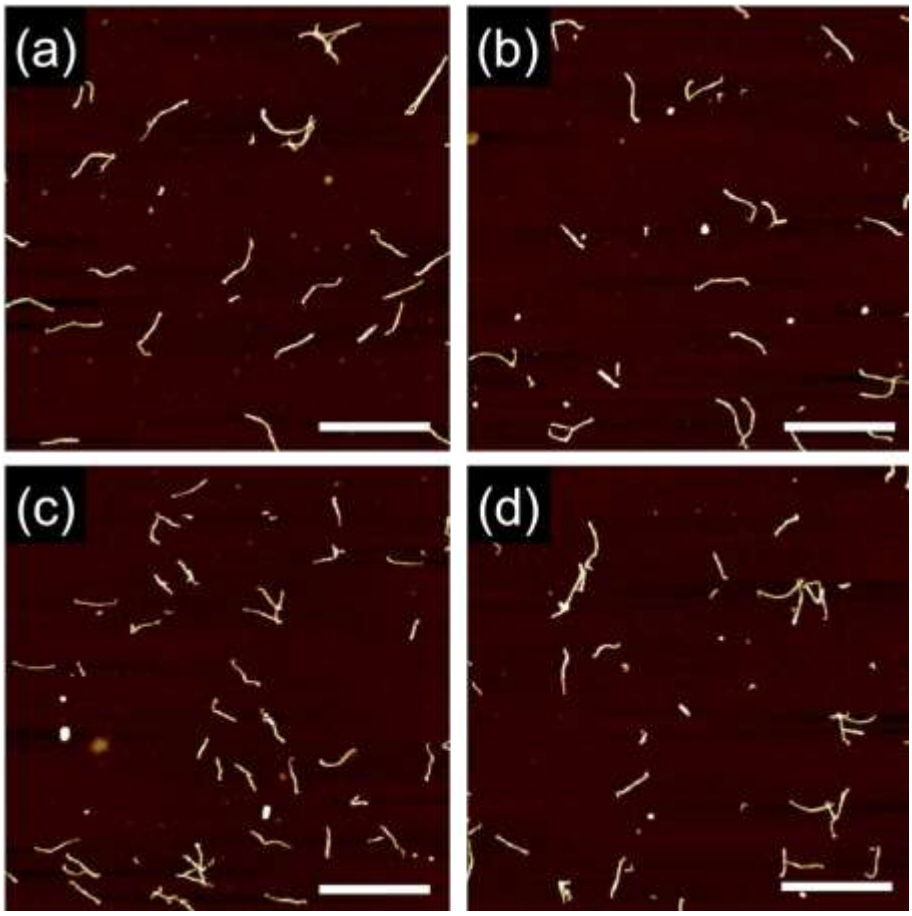

Figure S3. AFM topographic images of nanowires from dropcast films of **SBF**. The films were irradiated by 350 MeV $^{129}Xe^{26+}$ particles at a fluence of 1.0×10^9 cm^{-2} and developed by toluene at room temperature, and then immersed in $CHCl_3$ for (a) 10 min, (b) 30 min, (c) 1 h, and (d) 2 h. Scale bars represent 500 nm.

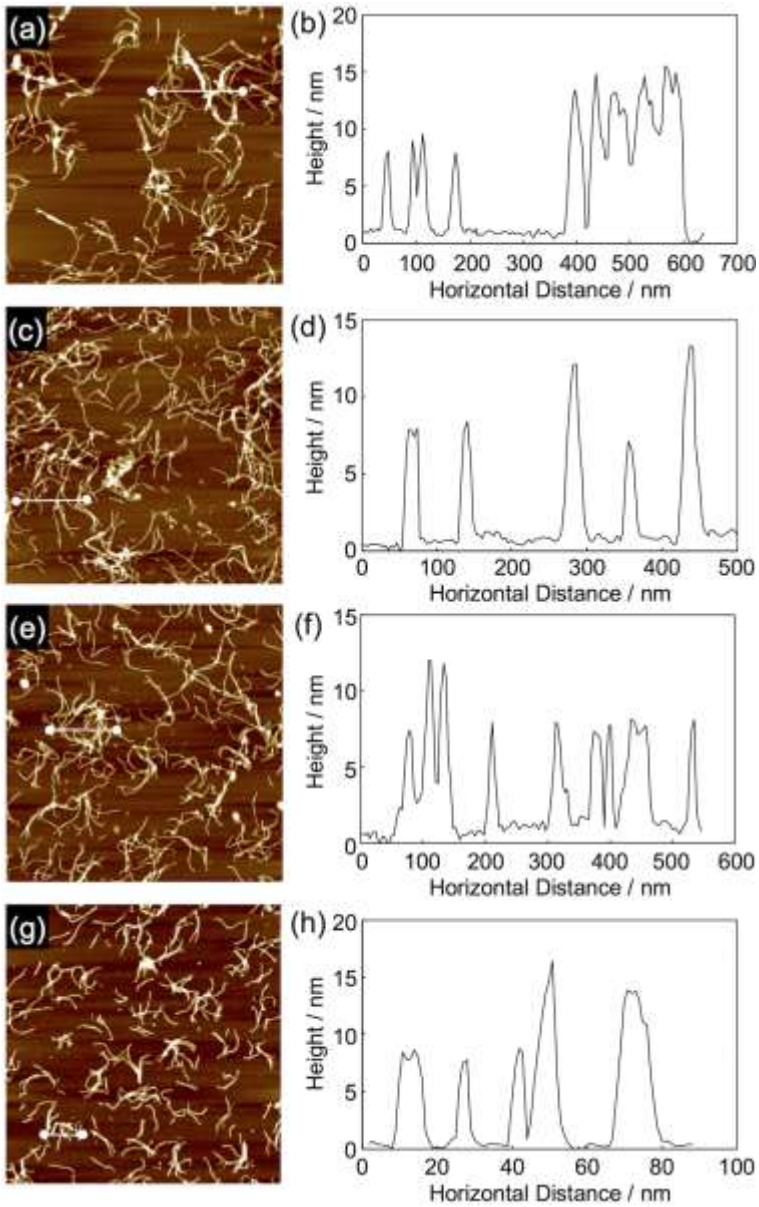

Figure S4. (a,c,e,g) AFM topographic images and (b,d,f,h) representative height profiles of nanowires from dropcast films of (a,b) **SBF**, (c,d) **2Br-SBF**, (e,f) **4Br-SBF**, and (g,h) **2,2'Br$_2$-SBF**. The films were irradiated by 350 MeV $^{129}Xe^{26+}$ particles at a fluence of 1.0×10^9 cm^{-2} and developed by toluene.

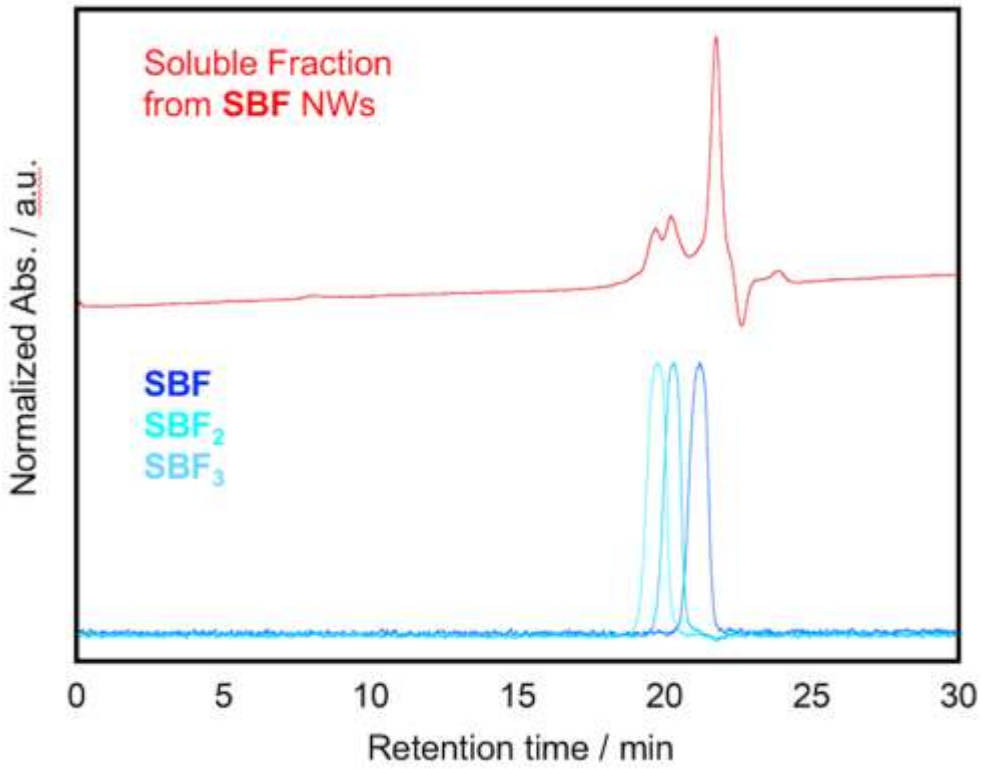

Figure S5. Analytical SEC profiles of **SBF**, **SBF$_2$**, and **SBF$_3$** (blue) and soluble fractions of the **SBF**-based nanowires (red) in THF. The formation of nanowires was confirmed by AFM after irradiation with 350 MeV $^{129}Xe^{26+}$ at a fluence of 1×10^{11} ions cm^{-2} and subsequent development of the dropcast films with toluene. Then the nanowires on a Si substrate was immersed in THF, sonicated, filtered from insoluble fraction and then injected into an analytical SEC system using THF as an eluent. Retention time was monitored by UV light at 280 nm.

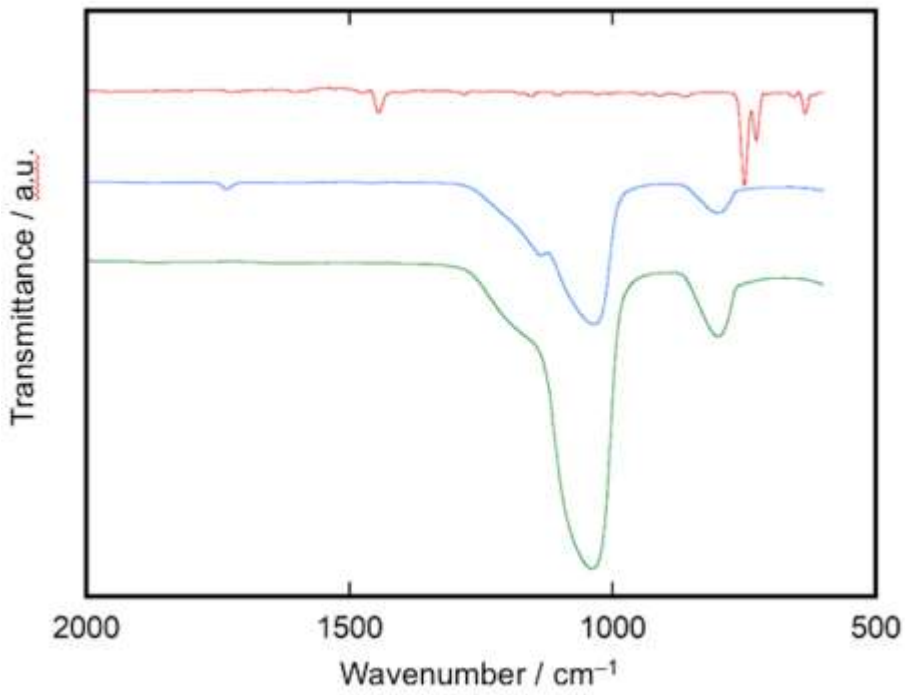

Figure S6. FT-IR spectra of powder samples of **SBF** (red) and nanowire form of **SBF** on quartz substrate (blue) together with that of quartz substrate (green). Only peaks corresponding to the silicon substrate was detected for the nanowire samples. Nanowires were fabricated by irradiation with 350 MeV $^{129}Xe^{26+}$ particles at the fluence of 1.0×10^{11} ions cm^{-2} and development with toluene.

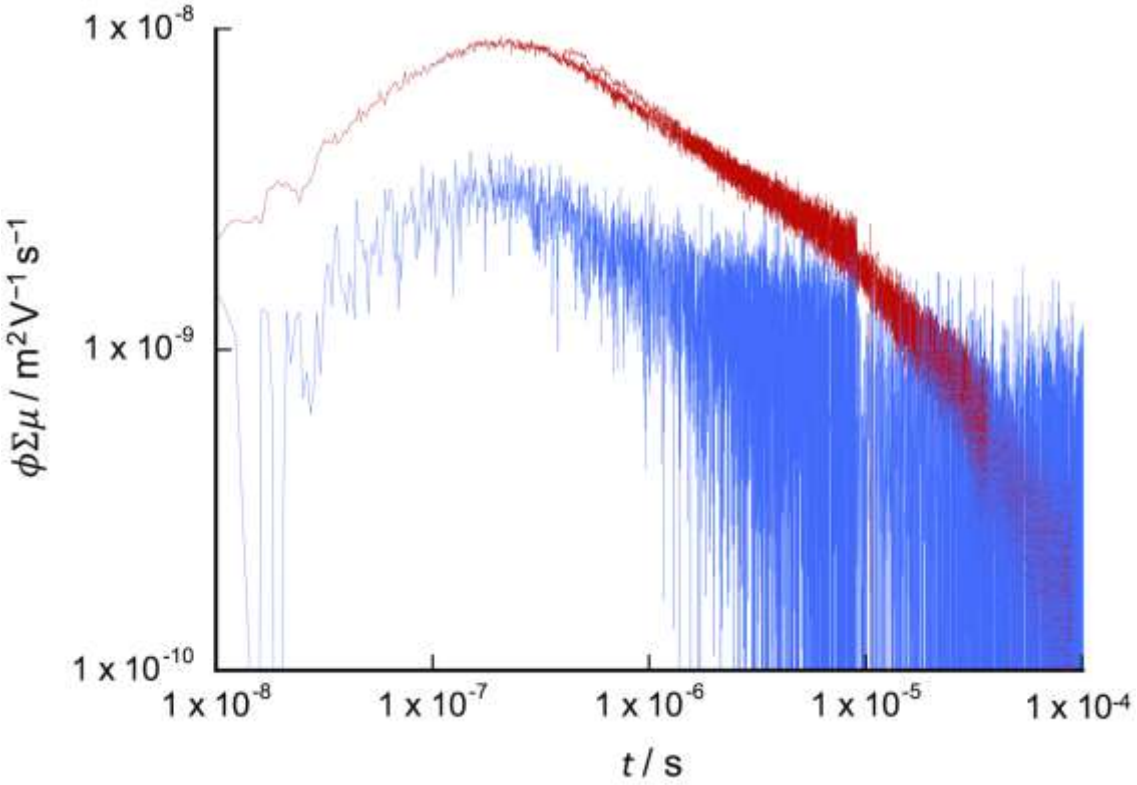

Figure S7. Kinetic trace of transient conductivity for **SBF**-based nanowires under nitrobenzene vapor at concentration of 2.0×10^2 ppm (red) and air (blue) upon exposure to 355 nm pulses at 9.1×10^{15} photons cm^{-2} $pulse^{-1}$. Nanowires were fabricated by irradiation with 350 MeV $^{129}Xe^{26+}$ particles at a fluence of 1.0×10^{11} cm^{-2}.

Chapter 2. Highly Efficient Solid-State Intra-Track Polymerization of Ethynyl-Substituted Spirobifluorenes Triggered by Swift Heavy Ion Irradiations

Synopsis

Acetylenes are the first monomer to polymerize by the energy deposited by ionizing radiations. Herein this study reveals an extremely efficient solid state polymerization of ethynyl-substituted 9,9'-spirobi[9H-fluorene]s (SBFs) *via* a unique nano-fabrication technique referred to as Single Particle Trigged Linear Polymerization (STLiP) initiated by high energy charged particles. The resulted nanowires of polymerized/crosslinked SBFs show a gradual transformation from flexible to rigid rod-like with an increase in the reaction efficiency mediated by the ethynyl substitution. The overall efficiency of initiation/propagation/crosslinking reactions is remarkably high even in comparison with the primary yield of ionization events in the radiation chemical processes, marking up to $G > 80$ $(100\ \text{eV})^{-1}$, which is suggestive of efficient chain reactions in the propagation steps. The present results demonstrate efficient solid-state polymerization reactions, which are neither topochemical polymerization reactions nor acid/base catalyzed reactions, expand the versatility of STLiP technique to fabricate 1D nanomaterials based on a variety of organic compounds.

Introduction

Ionizing radiation met polymeric materials in the third decade of the 20th century,[1–3] although the first report on the radiation induced polymerization reactions appeared in 1874, where electric discharge in acetylene vapor atmosphere gave “condensed materials” on the wall

of the discharge tube in spite of both “polymer” and “ionizing radiation” had not been yet discovered and remained unknown.[4] Since the pioneering works on the radiation induced polymerization reactions, a variety of monomeric molecules have been demonstrated both in their gas and condensed phases as effective substances to polymerize via initiating free radical species and subsequent chain propagation reactions.[5–7]

Ionizing radiations have been often discussed in terms of Linear Energy Transfer (LET) reflecting the rate of released kinetic energy from the incident particles or photons along their trajectory, and the value of LET is given with the unit of eV nm^{-1} .[8] Typical value of LET for X-rays or γ-rays ranges 0.1–0.5 eV nm^{-1} in condensed phases of organic molecular substances[9]. Considering the G-values or W-values of ionization events, one can presume the dispersive events without inter-correlation even in the condensed phase. This leads to homogeneous distribution of reactive intermediates, and thus advantageous for the subsequent quantitative analysis of radiation induced reactions. In contrast to the low-LET radiations, the LET values of α-particles or high energy heavy particles reach up to 1000 eV nm^{-1},[9–11] where the above schema of dispersive reactive intermediates are no longer available, giving critical overlap of ionization events and intercorrelation of reactive intermediates in small confined spatial area, which is often referred as an ion track.

Based on this convergence of released energy along the ionizing radiation trajectory, the subsequent chemical reactions within an ion track have been applied as the track detectors,[12] nanopore formation,[13] and nanochannel fabrication.[14] The merits of the high energy convergence have been also developed in the unique technique: “STLiP” which affords size- and number density-controlled nanostructures with high extremely high aspect ratio via intra-track polymerization reactions (**Figure. 1**). The key factor in the STLiP technique is to achieve gelation with high enough insolubility against successive wet development process with strong

solvent for initial target molecules,[15–18] and thus to trigger efficiently the initiation reactions and promote propagation reactions in a charged particle track.

To maximize the efficiency of the initiation as well as of propagation reaction, herein the target molecules were chosen as new molecular systems based on 9,9'-spirobi[9H-fluorene] (SBF) with Br or acetylene substituents; the former is expected to lead high yield of free radicals via the dissociative electron attachment (DEA) reactions, whereas the latter promotes highly efficient propagation reactions in condensed phases.

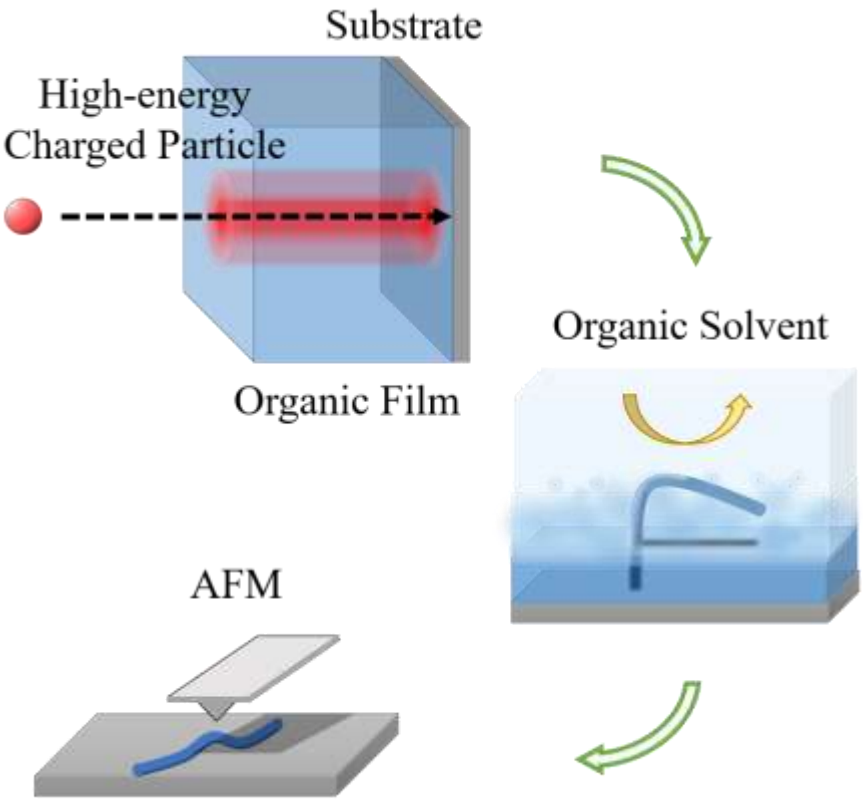

Figure 1. Schematic illustration of nanowire fabrication processes utilizing swift heavy ions that trigger crosslinking/polymerization reactions within ion tracks, and following isolation by development with organic solvents

Experimental

Materials: SBF derivatives **1**–**4** were purchased from Tokyo Chemical Industry Co. and used as-received. Compounds **5**–**7** were synthesized according to the literature.[19] The molecular structures of the compounds employed are shown in **Figure 2**. ^{1}H NMR spectra were recorded in $CDCl_3$ on a JEOL model AL-400 spectrometer operating at 400 MHz, where chemical shifts were determined with respect to tetramethylsilane (TMS) as an internal reference.

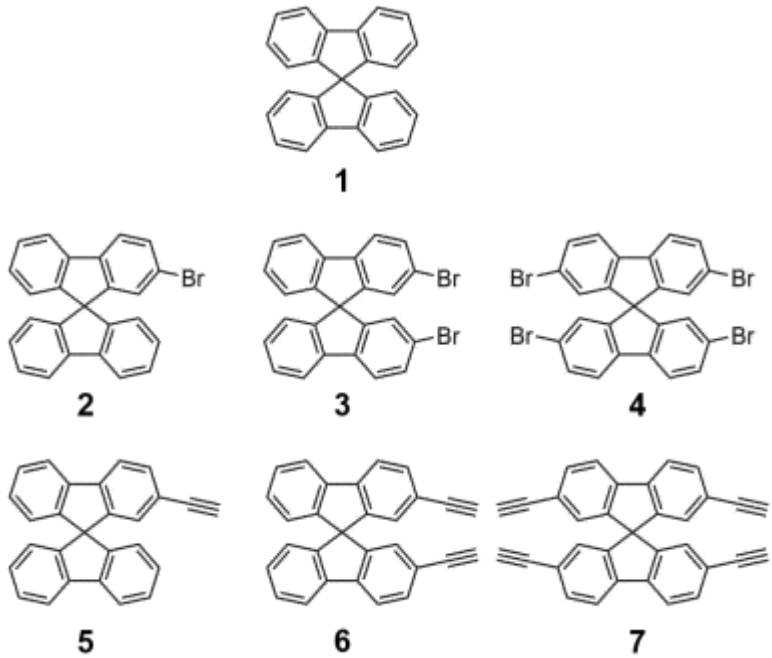

Figure 2. Chemical structures of the spirobifluorene derivatives **1**–**7** in this study

Method: Si substrates were cut into 1.5 × 1.5 cm^2 square pieces, sonicated in 2-propanol, dried, and treated with UV-O_3 irradiation prior to the use. All compounds were dissolved in $CHCl_3$ and spin-coated onto the Si substrate to yield thin films. The thickness of the films was evaluated by a Veeco Instruments Inc. model Dektak 150 surface profiler. 450 MeV $^{129}Xe^{23+}$ particles were generated from a cyclotron accelerator at Takasaki Advanced Radiation Research Institute. The prepared thin films were exposed to the above ion beam in a vacuum chamber (~ 1×10^{-4} Pa). The two-dimensional areal number density of incident particles was controlled

at 10^9–10^{11} particles cm^{-2}. No sublimation under vacuum was confirmed based on the film thickness. Then, the irradiated films were further cut into small pieces and developed by immersing them into toluene for ~1 min at room temperature. The morphology of the isolated nanowires was characterized by using a Bruker Co. model Multimode 8 atomic force microscopy (AFM). The loss of kinetic energy of ions due to penetration through the SBF films was estimated using the SRIM 2010 calculation code. Transition states of presumed neutral radical species in the propagation steps of polymerization reaction of **5**–**7** were calculated by Gaussian09 code.

Results and Discussion

Previous research reported that SBF frameworks were likely to be reacted upon irradiation of high LET charged particles and formed into clear and uniform nanowires by the STLiP process.[16] Halogenation of aromatic rings of SBF enhances the overall polymerization reactions mediated by free radicals remarkably due to DEA. In this study, irradiation of 450 MeV $^{129}Xe^{23+}$ particles also give nanowires with high enough durability against the wet-development processes by strong solvents such as $CHCl_3$ and tetrahydrofuran. The nano-fabrication of ethynyl-substituted derivatives was also conducted by an identical protocol. Considering that nano-gelation within an ion track by polymerization/crosslinking reactions causes the steep change in solubility of the molecular substances. Hence, the structural analysis could estimate the total volume of the nano-gels, and the overall yield of the reactions by direct tracing of the nanowire radius by AFM. The energy density released by a swift heavy ion can be regarded to be attenuated along with an inverse square law of *r*: the radial distance from the center of an ion track.[22] This allows us to calculate the energy density theoretical at the nanowire surface: the boundary of irradiated and non-irradiated part. Cross-sectional shapes of the resulted nanowires are presumed to suffer considerable deformation *via* strong interaction with substrate

surfaces during the development processes with the strong solvents. Thus, the volume of nano-gels was assessed by taking an ellipsoidal model for the cross-sectional shape; The *r* was defined as $r = (r_w r_h)^{1/2}$, where r_w and r_h are the half-width and half-height of the cross-section of the nanowires, respectively. The values of *r*, as well as their distribution, are averaged over more than 30 isolated nanowires for respective compounds **(Figure 3** and **4**). The values of r showed a good correlation with the intramolecular composition of bromine atom or ethynyl groups. It should be noted that the rather remarkable increase of *r* was observed with ethynylation than bromination of the target molecules. Ethynyl groups are expected to play a significant role in efficient polymerization/propagation reactions[23,24], and this is the case giving the dramatic increase in *r*.

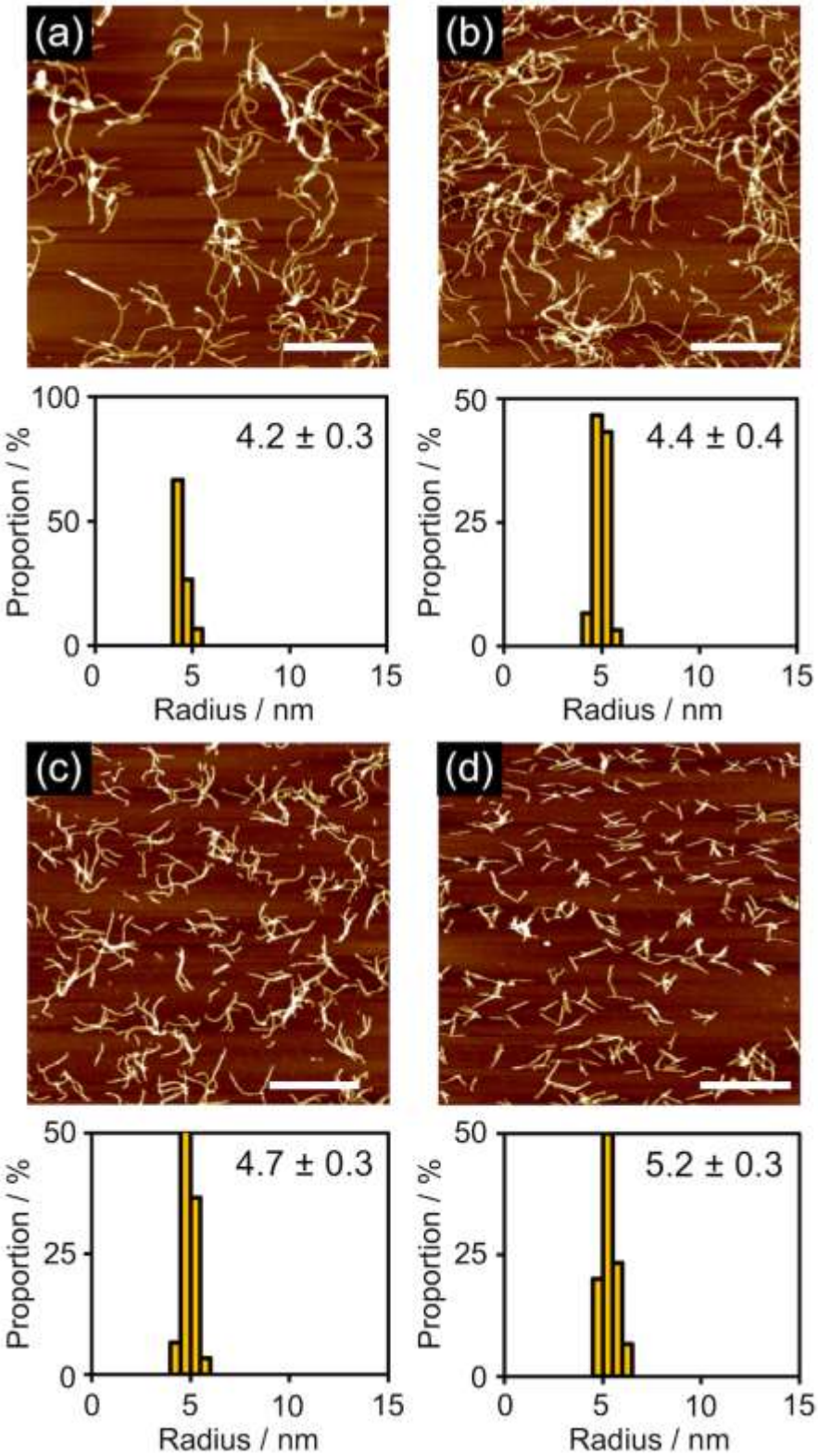

Figure 3. AFM topographic images and the radius distributions of the nanowires from spin-coated film of (a) **1**, (b) **2**, (c) **3**, (d) **4**. Nanowires were fabricated by irradiation with 450 MeV $^{129}Xe^{23+}$ particles at the fluence of 1.0×10^9 cm^{-2}.

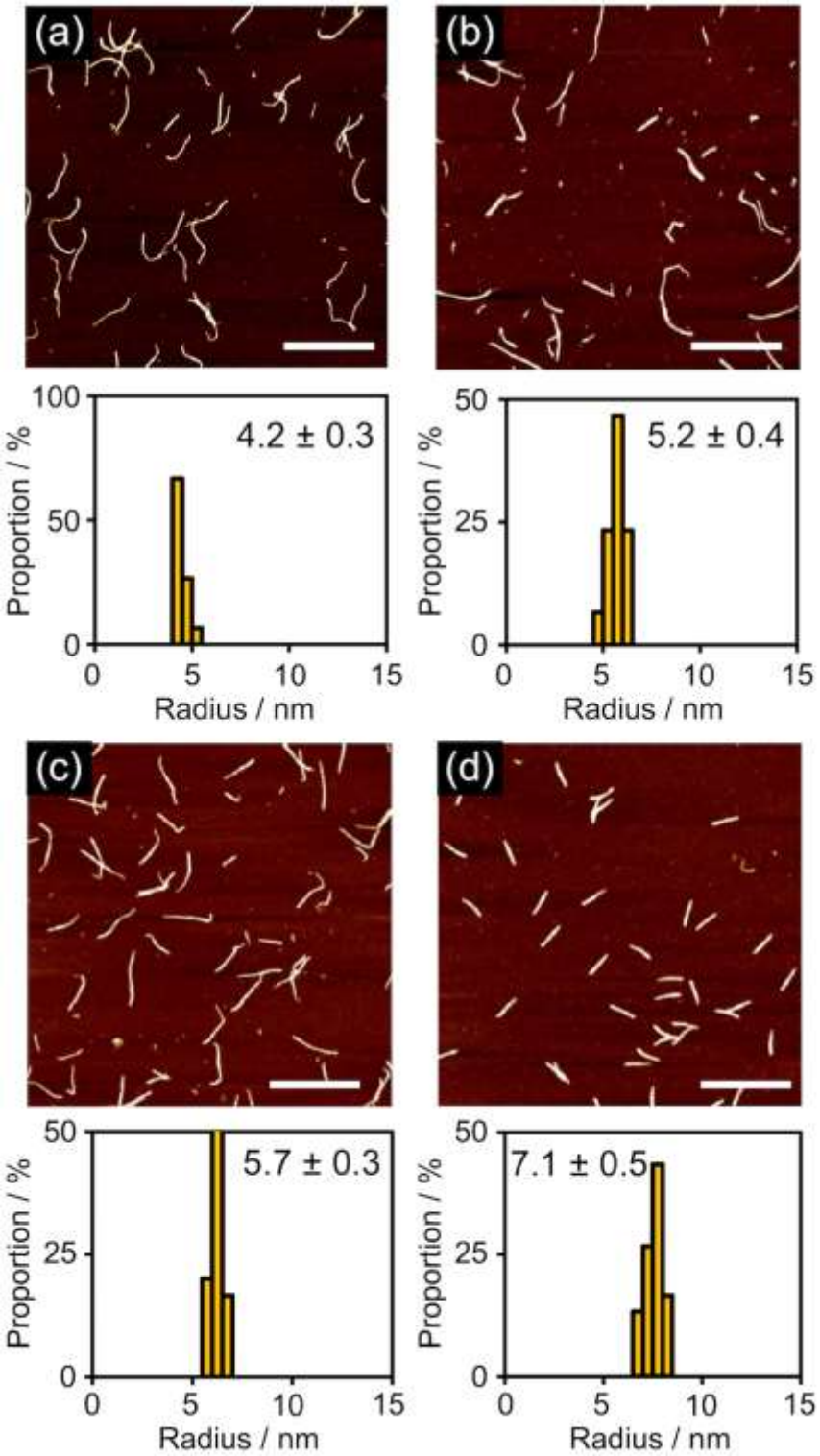

Figure 4. AFM topographic images and the radius distributions of the nanowires from spin-coated film of (a) **1**, (b) **5**, (c) **6**, (d) **7**. Nanowires were fabricated by irradiation with 450 MeV $^{129}Xe^{23+}$ particles at the fluence of 1.0×10^9 cm^{-2}.

To discuss quantitatively on the efficiency of polymerization reactions, the following theoretical model was adopted for estimating the radial energy density in an ion track depicted by two distinctive area: core and penumbra area. The radial energy density distribution in the two distinctive area: $\rho_c(r)$ and $\rho_p(r)$ are given by,[22]

$$\rho_c = \frac{\mathrm{LET}}{2}\left[\pi r_c^{\,2}\right]^{-1} + \frac{\mathrm{LET}}{2}\left[2\pi r_c^{\,2}\ln\left(\frac{e^{1/2}r_p}{r_c}\right)\right]^{-1},\ r \le r_c \qquad (1)$$

and

$$\rho_p(r) = \frac{\mathrm{LET}}{2}\left[2\pi r^2\ln\left(\frac{e^{1/2}r_p}{r_c}\right)\right]^{-1},\ r_c < r \le r_p \qquad (2)$$

where r and e are the calculated radius of the nanowire and an exponential factor, r_c and r_p are the radii of the core and penumbra areas given by the theoretical equation for the interaction of charged particles with matters. As can be seen from the energy distributions in **Figure 5**, the spatial deposited energy distributions are coalesced with each other for non-substituted or substituted SBF, and the observed values of r in the range of penumbra in all cases. This is strongly suggestive of r defined clearly by the contribution of reactive intermediates from respective compounds to the efficiency of initiation/polymerization(propagation) reactions.

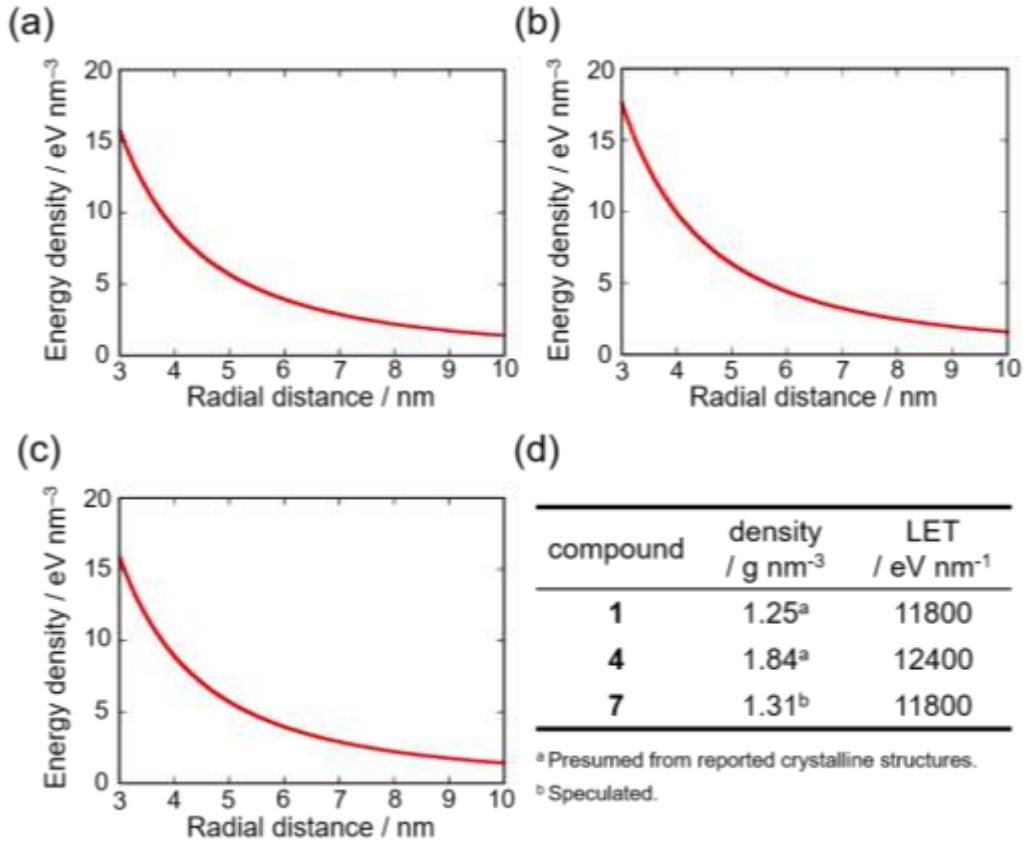

compound	density / g nm^{-3}	LET / eV nm^{-1}
1	1.25[a]	11800
4	1.84[a]	12400
7	1.31[b]	11800

[a] Presumed from reported crystalline structures.
[b] Speculated.

Figure 5. Energy distribution in the penumbra region for compound (a) **1**, (b) **4**, (c) **7** calculated from eq. (2). (d) Summary of density and calculated Linear Energy Transfer (LET) upon irradiation with 450 MeV $^{129}Xe^{23+}$. Densities of compound **1** and **4** are presumed from the articles.[20,21]

The overall efficiency of reactions contributing to the gelation of the present system can be discussed in terms of $G(x)$ that is defined as the number of overall reactions per absorbed 100 eV. Derived values of r reflect precisely the total volume of nanogels, thus $G(x)$ is in good correlation with r as,[25]

$$G(x) = \frac{400\pi\rho N_A r^2}{\mathrm{LET}\cdot M}\ln\left(\frac{e^{1/2}r_p}{r_c}\right) \quad (3)$$

where ρ is the density of the material, N_A is Avogadro's number, and M is the molecular weight, respectively. The derived values of $G(x)$ for all compounds are summarized in **Table 1**.

Table 1. Summary of density ρ, calculated linear energy transfer (LET), observed nanowire radii r, and estimated crosslinking reaction efficiencies $G(x)$ for each compound.

Compounds	**1**	**2**	**3**	**4**
ρ / g mol^{-1}	1.25	1.48	1.63	1.84
LET / eV nm^{-1}	11800	12000	12300	12400
r / nm	4.2 ± 0.3	4.4 ± 0.4	4.7 ± 0.3	5.2 ± 0.3
$G(x)$ / (100 eV)$^{-1}$	29	37	44	59
Compounds	**5**	**6**	**7**	
ρ / g mol^{-1}	1.29	1.29	1.31	
LET / eV nm^{-1}	11700	11700	11800	
r / nm	5.2 ± 0.4	5.7 ± 0.3	7.1 ± 0.5	
$G(x)$ / (100 eV)$^{-1}$	47	57	87	

Radiation-induced polymerization reactions including initiation and propagation reactions usually proceed through free-radical reactions, where a series of investigations have revealed the high-efficient polymerization from organic molecules (e.g. acetylene, propylene, butylene, methylmethacrylate, and styrene) since the early 20th century.[26–29] Especially, it has been reported that aromatic compounds show much less reactivity to radiation than the alkanes and alkenes because excitation of a π-electron appears as delocalized energy distribution due to transitions to lower energy level through the entire π-system. While, dissociative electron attachment has been known a candidate to raise the radical generation efficiency from aromatic compounds. The G value for primary yield of neutral radicals *via* DEA has been determined as 3.5–22.3 (100 eV)$^{-1}$ for chloride and bromide hydrocarbons,[30] which is much higher than that

of free ion yield of aromatic molecules such as benzene (G = 0.052 (100 eV)$^{-1}$).[31,32] These values are almost the upper limit of the efficiency of radiation induced free radical formation reactions. The observed values of G(x) in Br-substituted SBF are even higher than those of DEA, and G(x) > ~ 10 (100 eV)$^{-1}$ is often interpreted as the evidence of chain reaction in their propagation/polymerization reactions (**Scheme 1**). Furthermore, the increase of the reaction efficiency by multi-substitution with Br atoms also suggests that products can contribute again as electron acceptors acting as platforms for the subsequent polymerization/propagation by further DEA.

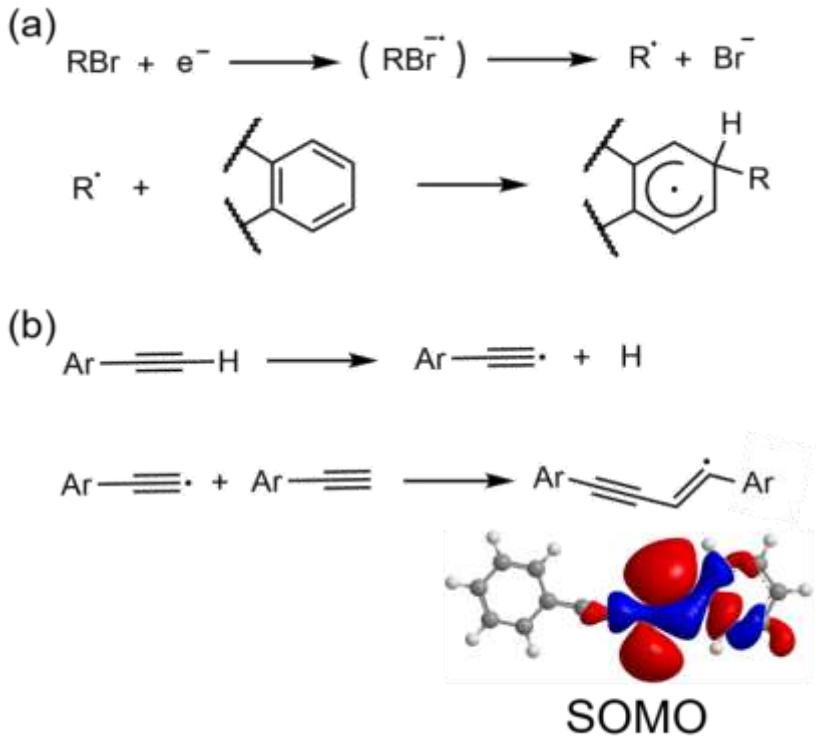

Scheme 1. Plausible primary reactions in (a) Br- and (b) ethynyl-substituted SBF as well as the structure of intermediates in the propagation steps of polymerization reactions. The optimized structures of a model compound of ethynyl-substituted SBFs were calculated by DFT with ROB3LYP/6-31G*.

These efficient free radical formation reactions, in contrast, cannot be expected in ethynyl-substituted SBFs. Nevertheless, the surprisingly high $G(x)$ over ~ 80 $(100\ eV)^{-1}$ beyond those in Br-substituted SBFs was recorded in **7**. Going back to the pioneering works on radiation-induced polymerization of gas and/or liquid acetylenes extensively investigated since 1960s, the polymerization yield of acetylene into cuprene had been reported $G > 70$ $(100\ eV)^{-1}$ upon irradiation to a variety of radiation sources including γ-rays, β-rays and swift heavy ions.[7,33,34] The major two reaction mechanisms were proposed to illustrate the chain reaction in the polymerization: 1) initiating from excited state of an acetylene molecule formed by (geminate or bulk) charge recombination followed by capturing neutral acetylene molecules, and 2) terminal hydrogen dissociation from the excited state of acetylene leading to free radicals for subsequent chain reactions. Considering the restricted molecular motions in the solid phase, the former mechanism rarely occur in the STLiP process. Therefore, the formation of polymeric nanowire can be well explained by free-radical chain reactions proceed *via* the highly reactive vinyl radicals.

Conclusion

Organic nanowires with desired number density and length were fabricated through the charged particle-initiated solid-state polymerization reactions of SBF and its brominated and ethynyl-substituted derivatives. The evaluation of the radius of the isolated nanowires and following estimation of *G* values indicated that the polymerization efficiency was increased upon bromination of SBF, which likely originates from the enhanced radical generation yields *via* DEA reactions. The estimated *G* values for ethynyl-substituted SBFs are further increased, reaching up to those of gas-phase polymerization of acetylenes in the case of tetra-ethynyl SBF. The observed remarkably high reactivity is possibly due to the generation of highly-reactive vinyl radicals as a result of the reaction between an initially-generated radical and carbon-

carbon triple bond, which eventually results in the efficient propagation reactions in the solid state.

References

1. Coolidge, W. D. *Science* 1925, 62, 441.

2. Mund, W., Koch, W. *Bull. Soc. Chim. Belges* 1925, 34, 119.

3. Lind, S.C., Bardwell, D.C., Perry, J. H. *J. Am. Chem. Soc.* 1926, 48, 1556.

4. Thénard, P., Thénard, A. *Compt. Rend.* 1874, 78, 219.

5. Hopwood, F. L. Phillips, J. T. *Proc. Phys. Soc.* 1938, 50, 438.

6. Wagner, C. D. *J. Phys. Chem.* 1961, 65, 2276.

7. Dorfman, L. M., Shipko, F. J. *J. Am. Chem. Soc.* 1955, 77, 4723.

8. Zirkle, R. E. *J. Cellular Comp. Physiol.* 1952, 39, 75.

9. Fano, U., Cooper, J. W. *Rev. Mod. Phys.* 1968, 40, 441.

10. Northcliffe, L. C. *Ann. Rev. Nucl. Sci.* 1963, 13, 67.

11. Ritchie, R. H., Brandt, W. *Phys. Rev. A* 1978, 17, 2102.

12. Jeong, T. W., Singh, P. K., Scullion, C., Ahmed, H., Hadjisolomou, P., Jeon, C., Yun, H., Kakolee, K. F., Borghesi, M., Ter-Avetisyan, S. *Sci. Rep.* 2017, 7, 2152.

13. Xia, F., Guo, W., Mao, Y., Hou, X., Xue, J., Xia, H., Wang, L., Song, Y., Ji, H., Ouyang, Q., Wang, Y., Jiang, L. *J. Am. Chem. Soc.* 2008, 130, 26, 8345.

14. Tian, Y., Zhang, Z., Wen, L., Ma, J., Zhang, Y., Liu, W., Zhai, J., Jiang, L. *Chem. Commun.* 2013, 49, 10679.

15. Horio, A., Sakurai, T., Kamiya, K., Lakshmi, G. B. V. S., Avasthi, D. K., Sugimoto, M., Yamaki, T., Chiba, A., Saito, Y., Seki, S. *Radiat. Phys. Chem.* 2018, 142, 100.

16. Sakaguchi, S., Sakurai, T., Ma, J., Sugimoto, M., Yamaki, T., Chiba, A., Saito, Y., Seki, S. *J. Phys. Chem. B* 2018, 122, 8614.

17. Horio, A., Sakurai, T., Lakshmi, G. B. V. S., Avasthi, D. K., Sugimoto, M., Yamaki, T., Seki, S. *Nanoscale* 2016, 8, 14925.

18. Takeshita, Y., Sakurai, T., Asano, A., Takano, K., Omichi, M., Sugimoto, M., Seki, S. *Adv. Mater. Lett.* 2015, 6(2), 99.

19. Xie, Z., Wei, Y., Zhao, X., Li, Y., Ding, S., Chen, L. *Mater. Chem. Front.* 2017, 1, 867.

20. Douthwaite, R. E., Taylor, A., Whitwood, A. C., *Acta Crystallogr., Sect. C: Cryst. Struct. Commun.* 2005, C61, o328.

21. Guo, A., Zhu, R. Acta Crystallogr., Sect. E: Struc. Rep. Online 2009, E65, o1528.

22. Chatterjee, A., Schaefer, H. J. *Rad. and Environm. Biophys.* 1976, 13, 215.

23. Garrison, W. M. *J. Chem. Phys.* 1947, 15, 78.

24. Rosenblum, C. *Bull. Soc. Chim. Belges,* 1937, 46, 503.

25. Seki, S., Tsukuda, S., Maeda, K., Matsui, Y., Saeki, A., Tagawa, S. *Phys. Rev. B* 2004, 70, 144203.

26. Hopwood, F. L., Phillips, J. T. *Nature* 1939, 143, 640.

27. Dainton, F. S. *Nature* 1947, 160, 268.

28. Schmitz, J. V., Lawton, E. J. *Science* 1951, 113, 718.

29. Chapiro, A., *Compt. Rend*. 1949, 228, 1490.

30. Chapiro, A. “Radiation Chemistry of Polymeric Systems” High Polymers. Vol. 15, Interscience Publishers, New York, 1962, p.263.

31. Grozema, F. C., Siebbeles, L. D. A., Warman, J. M., Seki, S., Tagawa, S., Scherf, U. *Adv. Mater.* 2002, 14, 228.

32. Acharya, A., Seki, S., Koizumi, Y., Saeki, A., Tagawa, S. *J. Phys. Chem. B* 2005, 109, 20174.

33. Mund, W., Rosenblum, C. *J. Phys. Chem*. 1937, 41, 469.

34. Jones, A. R. *J. Phys. Chem*. 1960, 61, 953.

Chapter 3. Porphyrin Nanowire Bundles for Efficient Photoconductivity, Photoemission, and Generation of Singlet Oxygens toward Photodynamic Therapy

Synopsis

Energy released from an accelerated high-energy single/cluster particle triggers solid-state polymerization and crosslinking reactions of porphyrin-based π-conjugated monomers within a nm-scaled 1-dimensional spatial area along the ion trajectory, resulting in the formation of an insoluble nanowire with a precise diameter and length. The nanowires are isolated by the development process–immersion of the irradiated film in organic solvents–and their shape and geometry are clearly characterized by atomic force microscopy. The obtained nanowire bundles, reflecting precisely the number of incident particles, show characteristic absorption spectra originating from porphyrin chromophores without significant degradation of the molecular cores. These porphyrin-based nanowires can be further functionalized into metallocomplexes by immersing the nanowires into solutions containing metal ion sources. The remarkable finding on the monomer structural parameters is that terminal alkyne groups are preferentially reacted and thus highly effective as a monomer structure for the present single particle-triggered linear polymerization (STLiP) method. The porphyrin-based nanowires show much higher photoconductivity than the precursor porphyrin films and enhanced fluorescence on silver nanoparticle layers via surface plasmon resonance. The porphyrin nanowires serve as photosensitizer mediating the generation of singlet oxygens, which is attractive for the use as a controlled nanosystem toward photocatalysis and photodynamic therapy.

Introduction

Porphyrins and phthalocyanines have been recognized as important series of π-conjugated molecules particularly used as building blocks in supramolecular assembly[1–3] with a variety of physico-chemical properties.[4] Porphyrins with rigid and planar geometries of molecular planes facilitate the molecular assembly and resulting their multifunctional optical and electronic properties. A variety of nano-assembled structuresn has been realized so far, bringing out their potentials of delocalized electrons over π-conjugated systems, spins of center metals, chemical stability of molecular frames, etc. The nano-assembly has been featured and tailored in their photophysical/photochemical properties,[5] catalytic activities, and biocompatibilities, and one of the most important key in the functional modulation is the compatibility of the chemical/structural stability and maximization of surface and interfaces of the assembled structures.

One-dimensional nanostructures with high aspect ratio are primarily advantageous to maximize the interfacial area which are accessible by the chemical substances in the catalytic cycles or electron/energy harvesting processes. Motivated by the strong inter-molecular interaction of porphyrin/phthalocyanine cores assisted by the center metal interaction and/or those of peripherals, successful 1D assemblies were achieved under controlled cross sectional geometry,[6–8] and demonstrated as electronic conductive wires,[9–12] efficient surface catalysts,[13] excitation energy harvesting networks,[14–16] sensing platforms,[17] optical switches and prisms.[18,19] Most of all the structures are thermodynamically favored predominantly by intermolecular dispersion forces and partially by formation of hydrogen bonding. Stabilization of the nano-architectures has also been addressed by the dimensional growth of the assemblies. The porphyrin-incorporated covalent organic frameworks (COFs) are one of the solutions for the system with both the compatibility of maximized interfaces and chemical stability via covalent bonds.[20,21] As in the case of the 1D structures, the thermally stable two-

dimensional networks of porphyrins/phthalocyanines have been realized with associated properties derived from the core molecules such as highly efficient electronic conductivity,[22,23] utility of catalytic activity around the central metals,[24,25] electrocatalysis,[26] etc. In particular, the high thermal and chemical stability of the framework systems allows us to modify the functional groups bridged to the porphyrin cores subsequently to the assembly structure formation without damages induced by the reactions, and the enhancement of the above properties were well demonstrated.[27,28] The COF systems can be presumed as an ideal materials to balance the stability and surfaces/interfaces, however the critical issues of the materials system are their processability to fabricate into the systems or onto the substrates, as well as the controllability of macroscopic dimensions such as the aspect ratio of the pore sizes. This is also the case for 3D functional systems incorporated with porphyrins/phthalocyanines assembled by the coordination chemistry; metal organic framework (MOF) systems. Well-stabilized 3D assembly structures of porphyrins were reported as a metalloporphyrin ligands-Co networks with square-shaped nanopores,[29] and the systems have been rapidly expanded to the porous materials.[30,31] The huge interfacial areas of the MOF systems have been, for instance, demonstrated as the platforms for dye sensitized solar cell systems.[32] The sensitivity was certainly improved as a result of efficient energy harvesting processes over the frameworks. However, the overall enhancement was less than expected because of the barrier for electron transport at the grain boundaries as well as the limited diffusion of ionic molecules within the nano-channels. Thus, porphyrin/phthalocyanine based 1D nanostructures with extremely high aspect ratio are still advantageous due to their ‘open’ interfaces with the larger surface area, if an appropriate stabilization method for the nanostructures can be applied.

Porphyrin nanosystems with the wider interfacial area are often chosen as a photo sensitizer (PS) in the agents used for photodynamic therapy (PDT) and photothermal therapy (PTT), because of their photo-energy harvesting nature with high extinction coefficients as well

as the efficient long-lived triplet excited state leading to reactive oxygen species.[33,34] Control of the size of porphyrin/phthalocyanine nanosystems is crucial to optimize cellular uptake by endocytosis, and thus for successive PDT processes. However, unsatisfactory results have often been reported in PDT despite the successful uptake into cells, due to the limitation of triplet excited state of PS in actual intra-cellular conditions.[35] Promising solution for this issue is the combination of PDT and PTT processes by designing the combined nanostructures of porphyrins/phthalocyanines and metal nanoparticles.[36]

1D organic nanowires have been successfully developed by high energy charged particle induced cross-linking/polymerization reaction in condensed organic media, referred to as Single Particle Nanofabrication Technique (SPNT) or Single Particle Triggered Polymerization (STLiP), which serves as a unique and versatile nanostructure formation technique with extra-wide flexibility of the target organic molecules.[37–42] It is worth mentioning that SPNT/STLiP techniques provide a particular advantage in preparing "combined" nanostructures, because the linearity of charged particle trajectories in the media gives adjoined nanostructure by use of multi-layered targets (**Figure 1**).[42] Porphyrins/phthalocyanines were endowed with high radiation resistivity by efficient energy dissipation processes via their developed π-electron systems. Focused ion beams were applied for nanomachining of condensed porphyrins, and the resulted nano/micro structures preserved their unique optical characteristics after the processing conditions.[43] Here we report the successful development of 1D porphyrin nanowires through STLiP method by using alkyne-modified porphyrin monomers as starting materials. The obtained nanowires are highly uniform and tunable in length and number density. The porphyrin chromophores are preserved in the nanowires and metal complexation as a nanowire form is available. The porphyrin nanowires showed improved photoconductivity measured by a microwave-based noncontact evaluation method. The nanowires were connected with Ag nanoparticle surface and exhibited enhanced fluorescence

by the effect of surface plasmon resonance. The detail of these unique nanofabrication method and properties of the obtained nanomaterials are discussed in the following section, which will be attractive toward future applications for photocatalysis[44,45] and PDT[46,47].

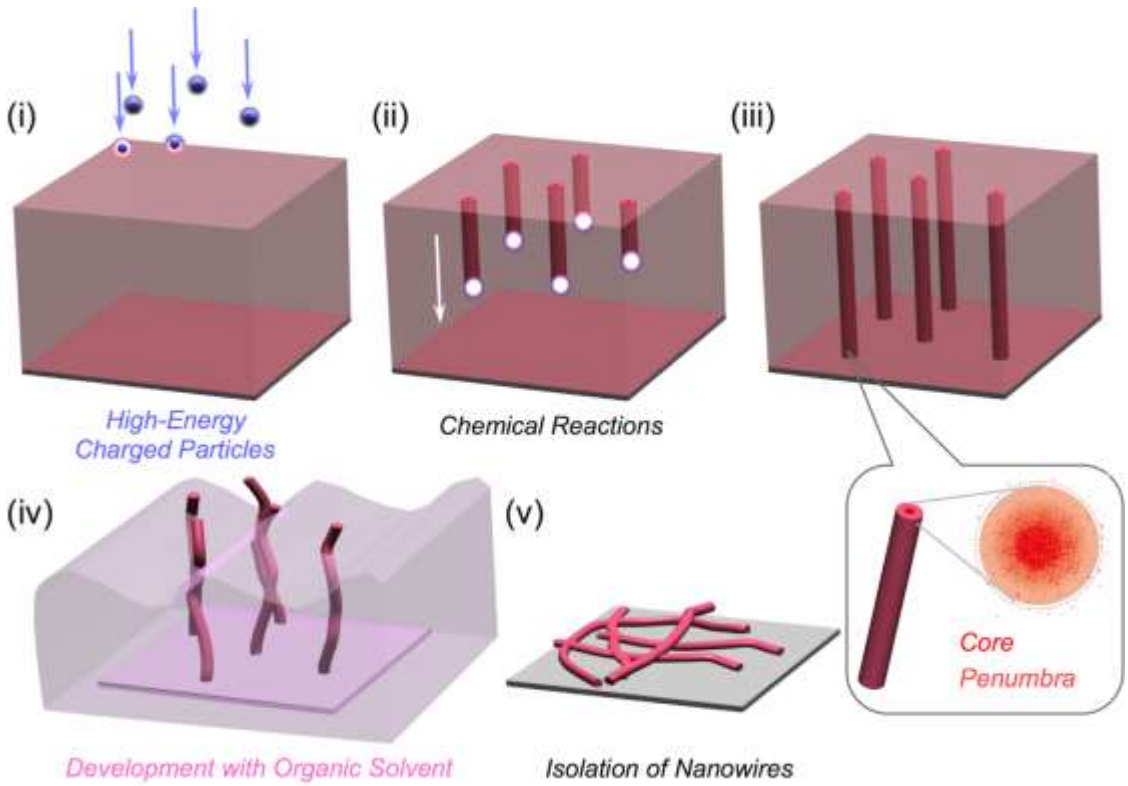

Figure 1. Schematic illustration of single particle-triggered linear polymerization.

Experimental

Materials: Tetraphenylporphyrin **1** was purchased from Tokyo Chemical Industry Co. Ltd. and used without further purification. Porphyrin derivatives **2**–**6** were synthesized as described in the Supporting Information. Unless otherwise noted, all commercial reagents were purchased from Wako Pure Chemical Industries Ltd., Tokyo Chemical Industry Co. Ltd., and Sigma-

Aldrich Co. and used as received. Column chromatography was performed on Silica Gel 60N (spherical, neutral) from Kanto Chemicals. TLC analyses were carried out on aluminum sheets coated with silica gel 60 (Merck 5554). ^{1}H-NMR spectra were recorded in $CDCl_3$ or THF-d_8 on a JEOL model AL-400 spectrometer, operating at 400 MHz, where chemical shifts were determined with respect to tetramethylsilane (TMS) as an internal reference.

Film Preparation: Si substrate was cut into 1.5 cm^2 square, sonicated in 2-propanol, dried, and treated with UV-O_3 prior to the use. Porphyrin derivatives were dissolved (5–10 wt%) in $CHCl_3$ for **1–4** and **6** and THF for **5**, and the solution was spin-coated or dropcast onto the Si substrate to give thin films with a uniform thickness. The thickness of the films was evaluated by a Veeco Instruments Inc. model Dektak 150 surface profiler.

Preparation of Ag Nanoparticle Surfaces: Silver nanoparticles (Ag NPs) with a diameter of ~15 nm were grown on the surface of quartz substrates by thermal evaporation at 10 nm thick under vacuum (~10^{-4} Pa). Ag thin solid films were grown on the substrates by the similar protocol at 50 nm thick.

Irradiation and Development: 490 MeV $^{192}Os^{30+}$ particles were generated from a cyclotron accelerator at Takasaki Advanced Radiation Research Institute, National Institutes for Quantum and Radiological Science and Technology. 150 MeV $^{107}Ag^{11+}$, 100 MeV $^{58}Ni^{7+}$, 60 MeV $^{28}Si^{5+}$, and 60 MeV $^{16}O^{5+}$ were generated from a Pelletron accelerator at Inter University Accelerator Centre. The loss of kinetic energy of ions due to their traversal through the organic films was estimated using the SRIM 2010 simulation code. The prepared thin films of triphenylamine derivatives were exposed to the above ion beam in a vacuum chamber (< 1 × 10^{-4} Pa). The number of incident particles was controlled at 10^8–10^{10} particles cm^{-2} to prevent severe overlapping of the ion tracks. Then, the irradiated films were further cut into small pieces, and developed by immersing them into organic solvents for 10–60 s.

Characterization of Nanowires: The sizes and shapes of the isolated nanowires were observed using a Seiko Instruments Inc. SPI-4000 atomic force microscope (AFM), Bruker Co. model Multimode 8 AFM, and JEOL Ltd. JSM-7001F scanning electron microscope (SEM). After AFM observation, the nanowires on substrates, fabricated with irradiation of 490 MeV $^{192}Os^{30+}$ particles at the fluence of 1×10^{10} ions cm^{-2}, were sonicated in THF. The eluent was filtered through a PTFE membrane, concentrated, and injected into a Hitachi model chromatography instrument (L-2130, L-2455, L-2350) with Shodex columns (KF-804L/KF-805L) using THF (Wako Pure Chemical Industries, Ltd., HPLC grade, stabilizer free) as an eluent at a flow rate of 1 mL min^{-1} at 40 °C, to study the excluded volume of polymerized products.

Measurements of Physical Properties of Nanowires: Electronic absorption spectra were recorded on a JASCO V-570 spectrometer. Infrared transmittance spectra were recorded on a Thermo Fisher Scientific NEXUS® 470 spectrometer with an attenuated total reflectance equipment. Fluorescence spectra were measured on a Hitachi High-Technologies model F-2700 fluorescence spectrophotometer. Flash-photolysis time-resolved microwave conductivity (FP-TRMC) measurements were carried out at 25 °C in air, where the resonant frequency and microwave power were properly adjusted at 9.1 GHz and 3 mW, respectively. Charge carriers were generated using a third harmonic generation (λ = 355 nm) of a Spectra Physics model INDI-HG Nd:YAG laser with a pulse duration of 5–8 ns. The photon density of the 355 nm laser pulse was 0.9×10^{16} photons cm^{-2}. The TRMC signal picked up by a diode (rise time < 1 ns) was monitored by a Tektronics model TDS3052B digital oscilloscope. The observed conductivities, given by a photocarrier generation yield (ϕ) multiplied by the sum of charge carrier mobilities ($\Sigma\mu$), were normalized according to the equation; $\phi\Sigma\mu = (1/eAI_0F_{light})(\Delta P_r/P_r)$, where, e, A, I_0, F_{light}, P_r, and ΔP_r represent unit charge of a single electron, sensitivity factor (S^{-1} cm), incident photon density of the excitation laser (photon cm^{-2}), correction (or filling) factor (cm^{-1}), and reflected microwave power and its change, respectively.

In the singlet oxygen ($^1O_2$) generation experiments, the fluorescence intensity of nanowires on the quartz substrate were monitored at room temperature under air using a JASCO FP-8500 fluorescence spectrophotometer equipped with a Xenon flash lamp. 420 nm light with the slit width of 5 nm was used for the excitation source.

Result and Discussion

Tetraphenylporphyrin was selected as a π-electronic system considering its strong absorptivity, charge and exciton transport capability, and high molecular design flexibility. Dropcast films of the pristine tetraphenylporphyrin (TPP: **1** in **Figure 2**) were prepared on Si wafers and quartz plates from its $CHCl_3$ solution. 5,10,15,20-Tetrakis(3-methylphenyl)porphyrin (**2**) was also used as a TPP analogue with high amorphous nature in films. TPPs carrying unsaturated carbon-carbon bonds such as vinyl (**3**) and ethynyl (**4, 5, 6**) groups instead of methyl groups at 3-positions were synthesized, whose functional groups were expected to have effects for radiation-induced reactions based on the previous macromolecular[48] and small molecular[49,50] examples. Initially, ion-beam irradiation of the prepared films of **1** at a low fluence (~10^8–10^{11} cm^{-2}) was carried out to achieve initiation and propagation reactions of the TPP monomers that lead to the formation of one-dimensional organogels along the trajectories (ion tracks) of the respective particles (**Figure 1**). Since there is a large difference between the linear energy transfers (LETs) of carbon-based materials and Si wafers, the primary charged particles and secondary electrons dominantly formed dense reactive species at the porphyrin/Si interface, leading to heterogeneous covalent bond formation. Thus, the termini of the nanowires are connected to the surface of the substrates, which avoids the nanowires to be washed away by solvents. The important requisite for this technique, named "single particle-triggered linear polymerization (STLiP)", is the difference in solubility between irradiated and non-irradiated parts, which enables the easy isolation of the resultant nanowires via development. In

principle, the initially formed nanowires stand on a substrate, where the length of the nanowires corresponds to the thickness of the films. After development, the nanowires lay down on the substrate due to the surface tension of the solvents.

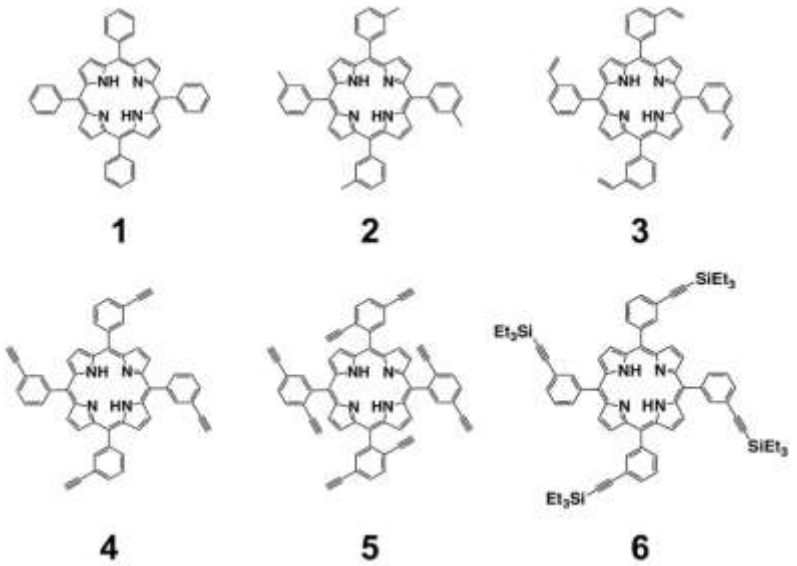

Figure 2. Chemical structures of porphyrin derivatives used in this study.

Figure 3a shows the atomic force microscopy (AFM) topographic image of nanowires from **1** after irradiation with 490 MeV $^{192}Os^{30+}$ ions (LET ~13800 eV nm^{-1}) at a fluence of 1 × 10^9 cm^{-2} and subsequent development with benzene. Although there were small numbers of broken nanowires with a shorter length, the length and diameter (or radius) of most of the nanowires are uniform (**Figure 3a** and **S1**). The radius of nanowire is calculated by applying the ellipse model to the cross-section of the nanowire. The values of r_x and r_y are defined as the half-width and half-height of the cross-section of the nanowires, respectively. The radius r is defined as $r = (r_x r_y)^{1/2}$. Nanowires were obtained similarly from the film of porphyrin **2**, where their radius was found to be a little bit larger than those obtained from **1** (**Table S1** and

Figure S1). Then, investigation of the peripheral substituent effect on the higher reactivity upon irradiation was conducted. The vinyl and ethynyl derivatives **3** and **4** are highly soluble in organic solvent such as toluene and $CHCl_3$ and thus afforded films with a thickness of sub-μm-to-μm ranges. After irradiation with the identical 490 MeV $^{192}Os^{30+}$ ions at a fluence of 1×10^9 cm^{-2}, both films gave clear nanowires with uniform length as well as diameter (**Figure 3c** and **d**). By using a high-resolution AFM for the nanowire bundles obtained by STLiP method with identical Os particle irradiation at a fluence of 1×10^{10} cm^{-2}, a sharp topographic image was recorded (**Figure 3g**). The overlap of the nanowires and uniformity in diameter were confirmed by tracing the height profile as shown in **Figure 3h**. One can notice that the flexibility (rigidity) of the observed nanowires is different between **3** and **4**. In fact, the rigidity, evaluated as d/L parameter, were 0.78 ± 0.14 and 0.97 ± 0.05 for **3** and **4**, respectively, and thus were different (**Table 1** and **Figure S3**), where d and L represent end-to-end distance and length of nanowires, respectively. This rigidity may originate from the high efficiency of chemical reactions among porphyrin monomers to fix the nanostructure. Nanowires from compound **5**, porphyrin with 8 ethynyl groups, were isolated similarly. Based on the end-to-endo distance, the rigidity of the nanowires from **5** was also found to be high (**Table 1** and **Figure S3**). These nanowires, fabricated from porphyrins with ethynyl substituents, are insoluble even in $CHCl_3$, which also supports the high reaction efficiency to form polymerized products that further integrated into the nanowire. In scanning electron microscopy (SEM), the morphology of nanowires was clearly visualized, involving their overlaps (**Figure S4a** and **S4b**) and the presence of "root" of nanowires connected to the substrate (**Figure S4c**). Indirect but more clear evidence for the connection between the nanowire termini and substrate was obtained by a ultrasonication process using the nanowires from **4** as an example (**Figure S5**). After the ultrasonication process, the number density of the nanowires got decreased, while the bright dots were appeared in the AFM image (**Figure S5b**). It can be considered as

the result that the dots correspond to the "root" of nanowires after the bond break by ultrasonication. If the connection is not present, no such "root"-like nano-object would be seen. Compound **6** is the analogue of **4**, where the alkyne termini are protected by triethylsilyl groups. Because of these silyl groups, **6** is highly soluble in $CHCl_3$ and even in hexane. Nevertheless, nanowires were successfully isolated by irradiation of **6** with 490 MeV $^{192}Os^{30+}$ and following treatment with hexane (**Figure 3f**). As expected, the rigidity parameter d/L for nanowires from **6** was estimated as 0.84 ± 0.16 that is smaller than those from **4**. Not only the rigidity parameters (d/L) (**Table 1**) but also the value of cross-sectional radius (r) (**Table S1**) reflect the efficiency of chemical reactions triggered by ion beam irradiations. The deposited energy is a function of the radius vector from the central axis (ion trajectory), and the larger radius of nanowires denotes that more efficient reactions take place for that compound when the same energy is deposited. In fact, the tendency of the order of r is in good agreement with that of d/L values.

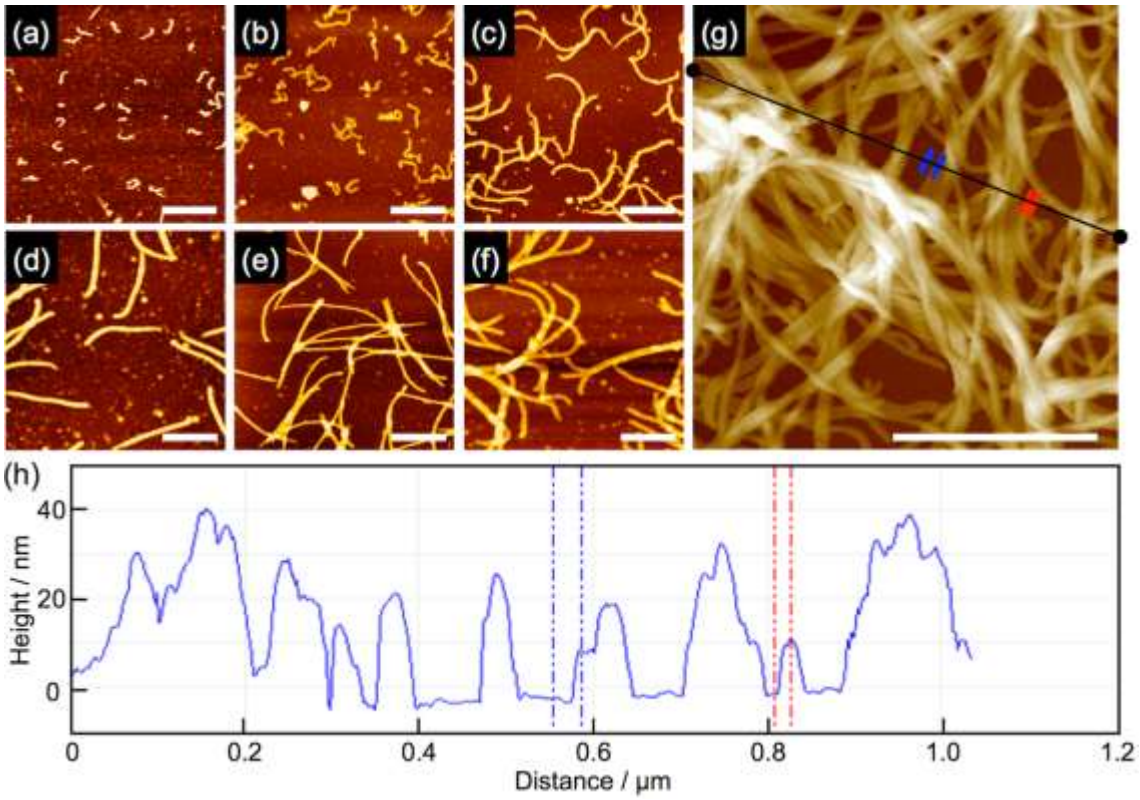

Figure 3. AFM topographic images of nanowires from thin films of (a) **1**, (b) **2**, (c) **3** (d) **4**, (e) **5**, and (f) **6**. The films for (a)(b)(e) and (c)(d)(f) were prepared by dropcast and spincoat methods, respectively, then irradiated with 490 MeV $^{192}Os^{30+}$ particles at the fluence of 1.0×10^9 ions cm^{-2}, and developed with benzene for (a–e) and *n*-hexane for (f). (g) High resolution AFM topographic image of nanowires from dropcast film of **4** after irradiation with at the 490 MeV $^{192}Os^{30+}$ particles at the fluence of 1.0×10^{10} ions cm^{-2}, and developed with benzene. Scale bars represent 500 nm. (h) Height profile along the direction indicated in (g).

Table 1. Averaged length (*L*) and end-to-end distance (*d*) of nanowires fabricated by irradiation with 490 MeV $^{192}Os^{30+}$ particles. Their ratio *d*/*L* indicates the rigidity of the nanowires.

	1	**2**	**3**	**4**	**5**	**6**
L / nm	163 ± 39	294 ± 109	628 ± 116	831 ± 40	926 ± 64	527 ± 131
d / nm	117 ± 37	196 ± 69	480 ± 67	805 ± 45	870 ± 93	429 ± 89
d/*L*	0.72 ± 0.17	0.70 ± 0.16	0.78 ± 0.14	0.97 ± 0.05	0.94 ± 0.06	0.84 ± 0.16

According to the fact that the absorption spectra indicated the retention of the porphyrin ring after polymerization processes and FT-IR spectra suggested the decrease of the stretching vibration of terminal alkyne groups, it is plausible that phenyl rings and/or its substituents (methyl, vinyl, alkynyl, and triethylsilyl groups) were most likely reacted in preference to the core parts and simultaneously have a great effect on the reaction efficiency of polymerization reactions. The obtained values of the averaged nanowire radii in **Table S1** suggest that triple bonds in compound **4** and **5** promote polymerization reaction more than other substituents even though reaction intermediates; silyl radicals in compound **6** were also generated.[37–39] Therefore, the high efficiencies in compound **4** and **5** can be explained by the generation of vinyl radicals, reactive intermediates produced by attack of neutral radical species to the terminal alkyne.[50] This behavior is presumed to be restricted for compound **6** due to the protection by triethylsilyl groups, resulting in the lower reaction efficiency. It should be noted that the reactivity to γ-rays for acetylene is reported to be higher than that for ethylene in gas phase.[51] Moreover, the radiolysis of ethylene yielded acetylene under suppression of direct

polymerization reaction,[52] which eventually leads to the radiation-induced polymerization.[53] This two-step reaction decreases the reaction efficiency for the overall polymerizations.

Then, the difference in reactivity by changing the ion species giving lower LET conditions was investigated. **Figure 4** represents the summary of AFM results on nanowire formation by using aluminum cluster ion irradiation.[54] As shown in **Figure 4d**, **h**, **l**, and **p**, compounds **2**–**5** allowed successful nanowire formation after irradiation with 6.0 MeV Al_4 and development with appropriate solvents. However, by changing the ion source to 4.5 MeV Al_3 offering a lower LET condition, **4** and **5** carrying ethynyl substituents provided clear nanowires while only small numbers of fragmented wires were observed for **2** and **3** (**Figure 4c**, **g**, **k**, and **o**). This tendency is more obvious in the case with 3.0 MeV Al_2 ions, where less rigid nanowires were seen for **4** and **5**. Finally, with 1.5 MeV Al_1 ion irradiation, only a film of **5** was found to afford, though partially fragmented, thin and flexible nanowires. This experiment clearly demonstrated the importance of ethynyl groups and their numbers on nanowire formation, i.e. chemical reaction efficiency upon ion beam irradiations. Similar experiments were done with different single ion species by using 150 MeV $^{107}Ag^{11+}$, 100 MeV $^{58}Ni^{7+}$, 60 MeV $^{28}Si^{5+}$, and 60 MeV $^{16}O^{5+}$ with the expected LET values of ~9500, 5500, 2100, and 500 eV nm^{-1} for Ag, Ni, Si, O, respectively (**Figure S6**). In this example, one can see the difference in reactivity between vinyl and ethynyl groups (**Figure S6c**, **d**, **g**, and **h**). Again, compound **5** having 8 ethynyl groups only realized the formation of nanowires among these porphyrin monomers by irradiation with 60 MeV $^{28}Si^{5+}$ (**Figure S6b**, **f**, **j**, and **n**). Porphyrin derivatives modified with different number of ethynyl groups (compounds **4a**–**4c**) were newly synthesized and nanowire formation capability was also studied (**Figure S7**). In this case, though the clear boundary of presence/absence of nanowires was not appeared, one can recognize the difference in rigidity and diameter, for example, in **Figure S7k**, **c**, **g**, and **k** with the use of 100 MeV $^{58}Ni^{7+}$ ions. As a summary so far, the remarkable impact of ethynyl

substituents on the monomer for STLiP method was demonstrated and porphyrin nanowires were successfully realized by this method.

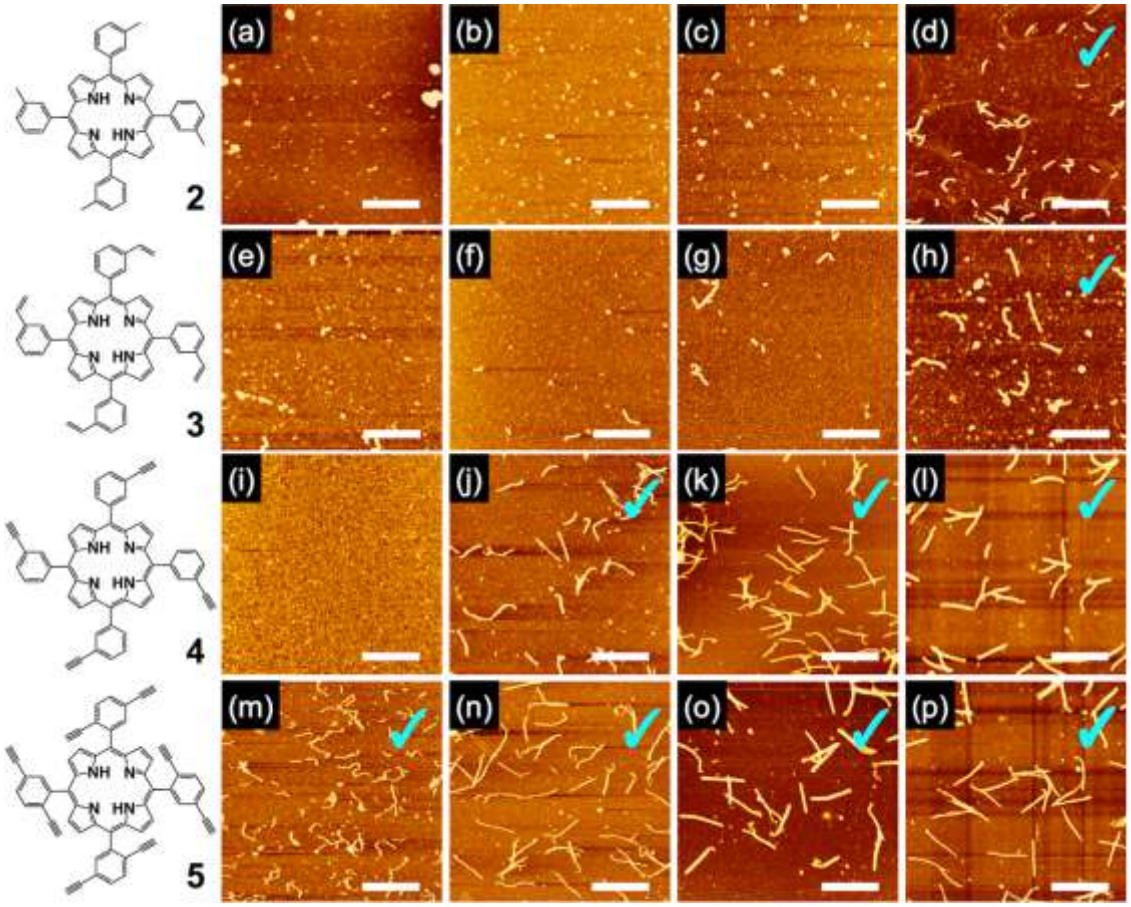

Figure 4. AFM topographic images of nanowires from spin-coated films of (a-d) **2**, (e-h) **3**, (i-l) **4** and (m-p) **5**. The films were irradiated with (a, e, i, m) 1.5 MeV Al_1^+, (b, f, j, n) 3.0 MeV Al_2^+, (c, g, k, o) 4.5 MeV Al_3^+, and (d, h, l, p) 6.0 MeV Al_4^+ particles at the fluence of 1.0×10^9 ions cm^{-2} and developed with *n*-hexane for **2** and benzene for **3**-**5**. Scale bars represent 500 nm. Check marks indicate successful nanowire isolation.

The constituent of the obtained nanowires should be the important topic. Firstly, presence of porphyrin chromophores in these nanowires was investigated. Nanowires on a quartz plate were fabricated by irradiation of dropcast films of **4**–**6** with 490 MeV $^{192}Os^{30+}$ ions at the fluence of 1.0×10^{10} ions cm^{-2} and development with benzene. The morphology of these bundled nanowires was characterized by AFM (**Figure S8**). Electronic absorption

spectra of the nanowire assembly indicated a sharp absorption band (Soret band) at around 420 nm accompanied with four minor peaks (Q band), both of which are characteristic of porphyrin chromophores (**Figure 5a**). Although the rise of baseline due to the light scattering at the surface of the nanowire assembled film was observed, presence of porphyrin chromophores in nanowires was confirmed. Regardless of the peripheral substituents, all the porphyrin nanowires from **1**–**6** recorded similar electronic absorption, excitation, and emission spectra (**Figure S9**) and thus suggests basically the same optical properties for all the nanowires. The film and nanowires from **6** recorded relatively restricted red-shift (**Figure S9c**), representing the weaker interaction probably due to the sterically-demanding triethylsilyl groups. In addition, these porphyrin cores were converted into metallocomplexes even in the nanowire form. By dipping the nanowire-assembled film in MeOH solution of $Cu(OAc)_2$, the coalescence of Q band was observed (**Figure 5a**), which is typical of metal complexation events of porphyrin derivatives.[55] Judging from the absorption peak, nanowires from **4** were not dissociated in this dipping condition. Meanwhile, when the nanowire film from **6** was dipped into MeOH solution of $Zn(OAc)_2$, conversion to Zn complex was again demonstrated, whereas the decrease of absorption was observed (**Figure 5b**). This fact suggested the partial dissociation of nanowires into MeOH probably due to the relatively higher solubility of **6** and/or Zn complex (MeOH can coordinate to the Zn center). Since such dissociation behaviors in good solvents were seen in the previous examples of triarylamine nanowires,[56] the effect of solvents on the present porphyrin nanowires was monitored. Remarkably, these nanowires kept their morphology even in hot $CHCl_3$, while highly-soluble **6** indicated the dissociation behavior. The initially-isolated nanowires, after irradiation with 490 MeV $^{192}Os^{30+}$ and development with hexane, were immersed in $CHCl_3$ for 30 sec and then further for 20 min. As a result, the change to the wavy shape was observed (**Figure S10**). In addition, the decrease of absorption was confirmed after the $CHCl_3$ treatment of the film of nanowire bundles

(**Figure S11**). Thus the author concluded that the polymerized products of **6** by STLiP method were partially dissociated and washed away by $CHCl_3$, leading to the morphological change of the nanowires. This behavior is characteristic of polymerization-based nanowire formation from small molecules that has not been seen in the crosslinking-dominant formation from macromolecules. In this sense, the reactivity of ethynyl-modified molecules is notable. The nanowires from **4** and **5** were not dissociated even in $CHCl_3$, while **4** and **5** themselves are highly soluble.

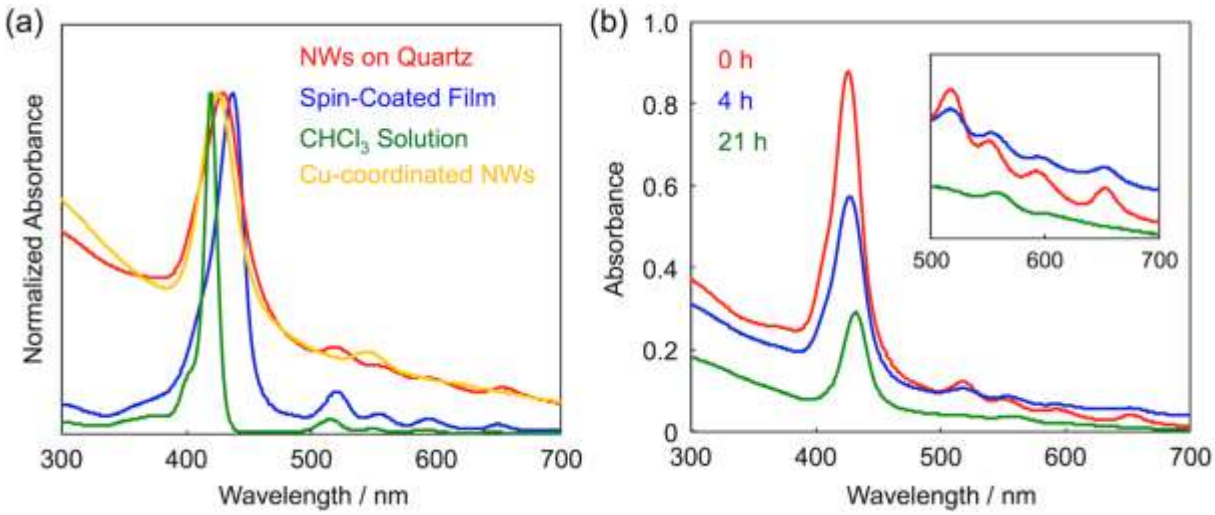

Figure 5. (a) Electronic absorption spectra of **4** in $CHCl_3$ (green), in film (blue), in nanowires (red), and in nanowires after immersed into MeOH solution of $Cu(OAc)_2$ for 24 h. (b) Electronic absorption spectra of **6** in nanowires (red), in nanowires after immersed into MeOH solution of $Zn(OAc)_2$ for (b) 4 h (blue) and (c) 21 h (green). Nanowires were fabricated by irradiation with 490 MeV $^{192}Os^{30+}$ particles at the fluence of 1.0×10^{10} ions cm^{-2} and development with benzene. Coalescence of Q band at 500–700 nm indicates the metallation with copper or zinc.

Although no dissociation was confirmed for nanowires from **4** and **5**, analysis of the molecular weight of polymerized products in the nanowires was examined. After usual development with benzene, the nanowire-bundled films were immersed in THF and sonicated for a few minutes. The THF solution was concentrated, filtered from insoluble fraction, and injected into an analytical size-exclusion chromatography (SEC) system. The retention time–absorbance profiles suggested the presence of larger molecular-weight products, where they showed strong absorption at the Soret band region (**Figure S12**). Thus, porphyrin chromophores are kept in the polymerized products in this molecular-weight region. In fact, monomer-based materials were mostly seen from this extract from THF and insoluble materials were also trapped in the filter before SEC analysis. However, it is possible to say that various molecular weight of polymerized products of porphyrins as well as incorporated monomer-based porphyrin molecules are the constituents of the nanowires that preserve the basic porphyrin-based light absorption capability.

FT-IR spectroscopy of nanowires was addressed to monitor the consumption of ethynyl substituents. IR spectrum of **4** in the powder form exhibited a relatively intense absorption peak at 3281 cm^{-1} accompanied with a shoulder at 3307 cm^{-1} (**Figure 6**). On the other hand, the nanowire film on the quartz displayed weak but split peaks at these wavenumber points. The peak of 3281 and 3307 cm^{-1} can be assigned as C-H vibrational mode of ethynyl groups and N-H vibrational mode of porphyrin cores. Indeed, the powder sample of Cu complex of **4** does not show the shoulder peak due to the absence of N-H bonds. Namely, after irradiation with 490 MeV $^{192}Os^{30+}$ ions, ethynyl groups were heavily consumed and thus N-H peak could be emerged in the nanowire form. In contrast, both monomer powders of **5** and its nanowires did not clearly show the N-H vibrational peak, which may be due to the relatively large (C≡)C-H peak from 4-times larger numbers of ethynyl groups than N-H in compound **5**.

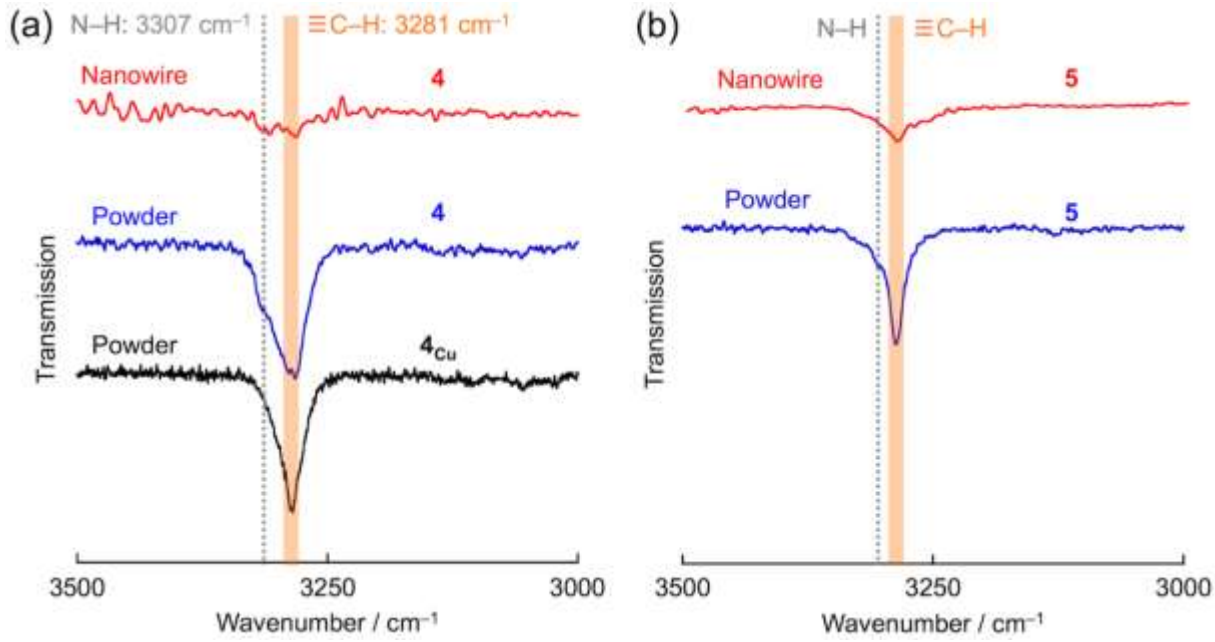

Figure 6. FT-IR spectra of powder samples and nanowire forms of (a) **4** and (b) **5**, together with copper complex of **4** in (a). Nanowires were fabricated by irradiation with 490 MeV $^{192}Os^{30+}$ particles at the fluence of 1.0×10^{10} ions cm^{-2} and development with benzene.

Aiming to expand the generality of the effect of ethynyl substituents, a phthalocyanine compound carrying four ethynyl groups was newly prepared and studied with STLiP method. As a result, obvious nanowires were seen in AFM (**Figure S13a** and **b**) under 490 MeV $^{192}Os^{30+}$ irradiation condition. Furthermore, tetra(4-ethynylphenyl)methane, one of the ultimate motifs with multiple phenylacetylene units, was subjected to the STLiP method. When irradiated with 490 MeV $^{192}Os^{30+}$ and developed by toluene, straight nanowires were obtained (**Figure S13c**). Then, by decreasing the LET with changing the ion species from 150 MeV $^{107}Ag^{11+}$ to 100 MeV $^{58}Ni^{7+}$, and then 60 MeV $^{28}Si^{5+}$, the diameter became small and rigidity got lower in this order for the isolated nanowires. Even in the irradiation with 1.5 MeV Al_1 ions, nanowires were partially observed though most of them were broken (**Figure S13d**).

Therefore, there would be no doubt of the effect of phenylacetylene units on the high reaction efficiency upon swift ion irradiation.

In order to demonstrate the physical property of the obtained porphyrin nanowires, charge carrier transporting property was investigated. Flash-photolysis time-resolved microwave conductivity (FP-TRMC) technique, a contactless microwave-based method, was employed for the measurements to avoid the contact resistance of electrodes.[57] Upon photoexcitation by pulses at 355 nm, the nanowire films from **3**, **4**, and **6** exhibited prompt rise and slow decay curves in conductivity transients (**Figure S14b**), where y-axis of $\phi\Sigma\mu$ represents the product of charge carrier generation efficiency ϕ and sum of hole/electron mobilities $\Sigma\mu$. The gradual decay of the signal indicates the deactivation process of the photo-generated charge carriers including recombination and trapping. By comparing the FP-TRMC profiles of initial nanowire films (**Figure S14a**), it is obvious that the nanowire forms gave at least 10-fold higher photoconductivity. The increase of $\phi\Sigma\mu$ at the end-of-pulse also suggests the enhancement of charge carrier generation efficiency. The slightly larger $\phi\Sigma\mu$ for the nanowire bundles from **6** may derive from the enhanced photoinduced charge separation for a bit separated porphyrin cores as mentioned in the absorption spectra (**Figure S9c**). According to the reported studies of conventional porphyrin systems, the major pathway to give free charge carriers is triplet-triplet annihilation reaction upon excitation at Solet and Q bands of porphyrin moieties.[58–60] The long-lived triplet state of porphyrins is presumed to populate predominantly at the surface of the nanowires, which motivates the application of porphyrin nanowires as a photosensitizer for reactive oxygen generations.

Singlet oxygen sensor green (SOSG) has been widely used as a turn-on sensor molecule in a variety of fields such as biology, medicine, and chemistry, since it easily reacts with singlet oxygens and accordingly emits green fluorescence (**Figure 7a**).[61] In this experiment, the function as a photosensitizer for porphyrins[33,34] at the surface of nanowires was tested by the

observation of fluorescence enhancement from SOSG probe. The isolated nanowires fabricated by irradiation of **6** with 490 MeV $^{192}Os^{30+}$ ions at the different fluence, 1.0×10^{10} and 1.0×10^{11} ions cm^{-2}, were exposed to 420 nm light (~maximum absorption wavelength of porphyrin chromophore) to generate singlet oxygens (**Figure 7b**), resulting in the reasonable plot of the fluorescence intensity of SOSG (λ_{em} = 540 nm, λ_{ex} = 509 nm) as a function of irradiation time (**Figure 7c**). Fluorescence enhancement was observed for the porphyrin nanowire system with higher fluence (~number density: 1.0×10^{11} ions cm^{-2}), indicating the retention of porphyrin chromophore at the nanowire surfaces after nanowire fabrication process. The demonstrated nanoscale objects with photosensitizing property encourage the application to PDT.

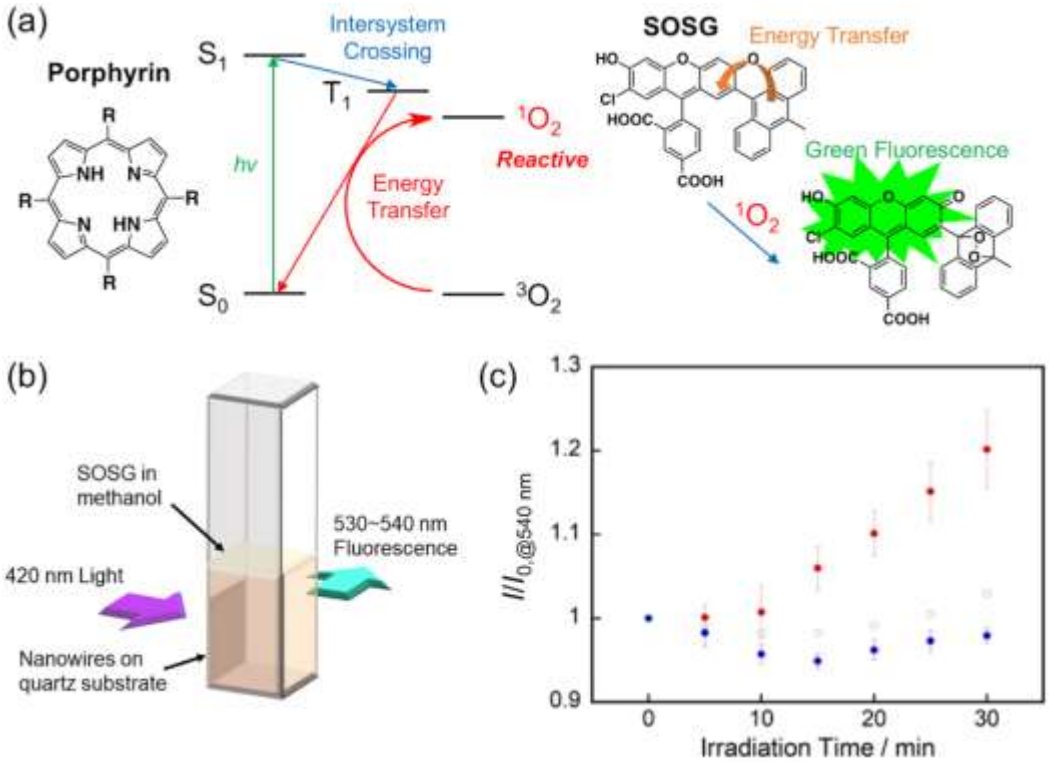

Figure 7. (a) Schematic illustration of porphyrin-sensitized singlet oxygen generation and its reaction with singlet oxygen sensor green (SOSG). (b) Schematic illustration of experimental setup. (c) Fluorescence intensity ratio I/I_0 at 540 nm (λ_{em} = 540 nm, λ_{ex} = 509 nm) as a function of photo-irradiation time at 420 nm observed for SOSG alone (green, control), and SOSG with porphyrin NWs fabricated by irradiation of **6** with 490 MeV $^{192}Os^{30+}$ particles at the fluence of 1.0×10^{10} ions cm^{-2} (blue) and 1.0×10^{11} ions cm^{-2} (red).

As another demonstration of porphyrin nanowire system, enhanced fluorescence was demonstrated by combining the porphyrin nanowires with silver nanoparticles (NPs). Metal NPs, particularly those of the noble metals, exhibit strong surface plasmon resonances (SPRs) with intense optical absorption bands that lead to the strong localized electric fields around the surfaces. For example, Ag NPs are known to show SPR absorption peak at around 400–500 nm when the particle size is below ca. 50 nm.[62] Considering this peak matching with Soret band of porphyrins, nanowires from a porphyrin derivative with a quite similar structure with **6** were fabricated on Ag nanoparticles. Ag NPs with a diameter of ~15 nm were developed

on the surface (**Figure 8d** and **S15**) by simple evaporation of Ag on a quartz substrate with the target thickness of 10 nm. On the other hand, deposition of Ag with the target thickness of 50 nm did not result in the Ag NPs but Ag film (**Figure 8e**). The nanowires from the above porphyrin derivative were easily prepared on all these surfaces with almost identical number density as well as length of nanowires (**Figure 8a–c**). In fluorescence spectroscopy, these nanowires on the quartz and 50 nm-thick Ag surface showed quite low emission with (**Figure 8e**). In contrast, the porphyrin nanowires on the 10 nm-thick Ag NPs showed significantly larger emission, particularly obvious at 650 nm. The enhanced emission behavior, demonstrated on Ag NPs with the size of 30–60 nm, reflected the presence of SPR and resulting stronger excitation phenomenon.[63] Future development of hybrid nanomaterials composed of these organic nanowires and metal NPs will open the possibility in the field of sensor and medical applications.[62]

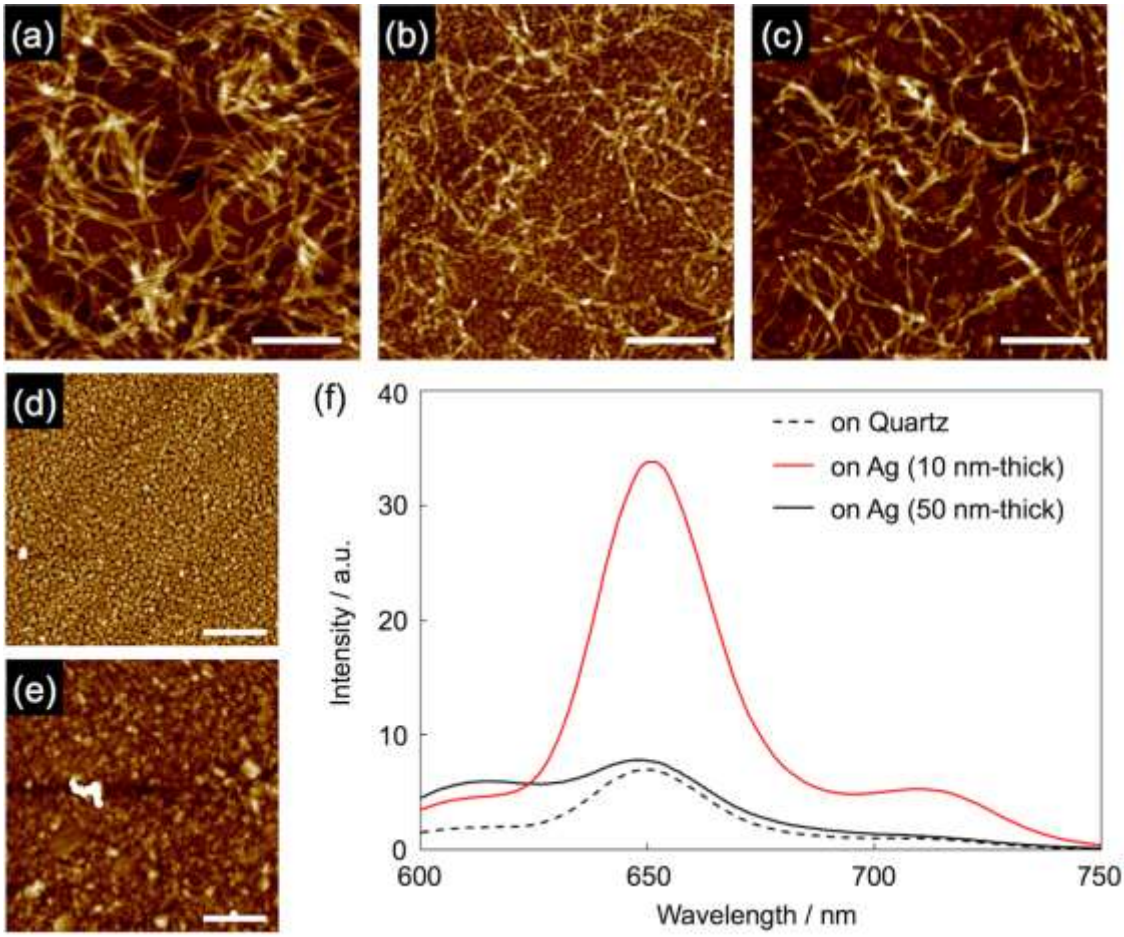

Figure 8. AFM topographic images of nanowires from thin films of tri(isopropylsilyl)-protected analogue of **6** on (a) quartz, (b) 10-nm thick Ag, and (c) 50-nm thick Ag. AFM topographic images of (d) 10-nm and (e) 50-nm thick vapor-deposited Ag on quartz for reference. The films were prepared by dropcasting, irradiated with 490 MeV $^{192}Os^{30+}$ particles at the fluence of 1.0×10^{10} ions cm^{-2}, and developed with cyclohexane. Scale bars represent 500 nm. (f) Fluorescent spectra of nanowires for tri(isopropylsilyl)-protected analogue of **6** on quartz (black, dashed), 10-nm thick Ag (red, solid), and 50-nm thick Ag (black, solid). The spectra were obtained from the samples for (a), (b), and (c), respectively.

Conclusion

In conclusion, this study developed the porphyrin-based organic nanowires with desired length and number density via high-energy charged particle-triggered chemical reactions within ion tracks (STLiP method). Through this work, it was revealed that the remarkable effect of functionalization with ethynyl groups to porphyrin monomers on the reaction efficiency upon irradiation of swift heavy ions. Monitoring the significant consumption of ethynyl groups in nanowires as well as the detailed nanowire formation experiments by changing the peripheral molecular structure and ion species. The design concept of alkyne modification is also effective for other small molecules, which expands the generality of this design for developing nanowires from any organic π-systems. The obtained nanowires are converted into metallocomplexes as a nanowire form and exhibited larger photoconductivity than the pristine amorphous films of porphyrin monomers most likely due to the fixation of the π-stacked porphyrin aggregates. Porphyrin nanowires serve as a photosensitizer for the production of singlet oxygens, which is attractive as a controlled nanosystem potentially useful for the photocatalysis and photodynamic therapy. Moreover, porphyrin nanowires, combined with Ag nanoparticles with a diameter of several tens of nm, showed enhanced fluorescence due to the excitation from the surface plasmon resonance of Ag nanoparticles at around 420 nm. Considering the potential of conductive and photonic functions demonstrated here, as well as the unveiled effective molecular design using alkyne groups, we believe that various functional organic nanowires would be available through the STLiP method that would contributes to the development of organic nanoelectronics and photonics.

References

1. Beletskaya, I.; Tyurin, V. S.: Tsivadze, A. Y.; Guilard, R.; Stern, C. *Chem. Rev.* **2009**, *109*, 1659–1713.
2. Bottari, G.; Torre, de la G.; Guldi, D. M.; Torres, T. *Chem. Rev.* **2010**, *110*, 6768–6816.
3. Torre, de la G.; Claessens, C. G.; Torres, T. *Chem. Commun.* **2007**, *43*, 2000–2015.
4. Torre, de la G.; Bottari, G.; Sekita, M.; Hausmann, A.; Guldi, D.M.; Torres, T. *Chem. Soc. Rev.* **2013**, *42*, 8049–8105.
5. Kundu, S.; Patra, A.; *Chem. Rev.* **2017**, *117*, 712−757.
6. Medforth, C. J.; Wang, Z.; Martin, K. E.; Song, Y.; Jacobsen, J. L.; Shelnutt, J. A. *Chem. Commun.* **2009**, *45*, 7261–7277.
7. Hasobe, T. *Phys. Chem. Chem. Phys*. **2012**, *14*, 15975–15987.
8. Adinehnia, M.; Mazur, U.; Hipps, K. W. *Cryst. Growth Des.* **2014**, *14*, 6599−6606.
9. Bottari, G.; Olea, D.; Gómez-Navarro, C.; Zamora, F.; Gómez-Navarro, J.; Torres, T. *Angew. Chem. Int. Ed.* **2008**, *47*, 2026–2031.
10. Zhai, X.; Alexander, D.; Derosa, P.; Garno, J. C. *Langmuir* **2017**, *33*, 1132−1138.
11. Zijll, M. van; Borders, B.; Mazur, U.; Hipps, K.W. *J. Phys. Chem. C* **2016**, *120*, 14962−14968.
12. Allec, S. I.; Ilawe, N. V.; Wong, B. M. *J. Phys. Chem. Lett.* **2016**, *7*, 2362−2367.
13. Guo, P.; Chen, P.; Liu, M. *ACS Appl. Mater. Interfaces* **2013**, *5*, 5336−5345.
14. Bera, R.; Mandal, S.; Mondal, B.; Jana, B.; Nayak, S. K.; Patra, A. *ACS Sustainable Chem. Eng.* **2016**, *4*, 1562−1568.
15. Li, J.-J.; Peng, H.-D.; Shi, L.-Y.; Wub, H.-D.; Pan, G.-B. *RSC Adv.* **2017**, *7*, 8151–8155.
16. Hartmann, H.; Barke, I.; Friedrich, A.; Plötz, P.-A.; Bokareva, O.S.; Bahrami, M.; Oldenburg, K.; Elemans, J. A. A. W.; Irsig, R.; Meiwes-Broer, K.-H.; Kühn, O.; Lochbrunner, S.; Speller, S. *J. Phys. Chem. C* **2016**, *120*, 16977−16984.

17. Guo, P.; Zhao, G.; Chen, P.; Lei, B.; Jiang, L.; Zhang, H.; Hu, W.; Liu, M. *ACS Nano*, **2014**, *8*, 3402–3411

18. Wu, L.; Wang, Q.; Lu, J.; Bian, Y.; Jiang, J.; Zhang, X. *Langmuir* **2010**, *26*, 7489–7497.

19. Cai, W.-R.; Zhang, G.-Y.; Lu, K.-K.; Zeng, H.-B.; Cosnier, S.; Zhang, X.-J; Shan, D. *ACS Appl. Mater. Interfaces* **2017**, *9*, 20904−20912.

20. Diercks, C. S.; Yaghi, O. M. *Science* **2017**, *355*, 923−931.

21. Lin, G.; Ding, H.; Chen, R.; Peng, Z.; Wang, B.; Wang, C. *J. Am. Chem. Soc.*, **2017**, *139*, 8705–8709.

22. Wan, S.; Gándara, F.; Asano, A.; Furukawa, H.; Saeki, A.; Dey, S. K.; Liao, L.; Ambrogio , M.W.; Botros, Y. Y.; Duan, X.; Seki, S.; Stoddart, J. F.; Yaghi, O. M. *Chem. Mater.* **2011**, *23*, 4094–4097.

23. Liu, J.; Zhou, W.; Liu, J.; Howard, I.; Kilibarda, G.; Schlabach, S.; Coupry, D.; Addicoat, M.; Yoneda, S.; Tsutsui, Y.; Sakurai, T.; Seki, S.; Wang, Z.; Lindemann, P.; Redel, E.; Heine, T.; Wöll, C. *Angew. Chem. Int. Ed.* **2015**, *54*, 7441–7445.

24. Lin, S.; Diercks, C. S.; Zhang, Y.-B. Kornienko, N.; Nichols, E. M.; Zhao, Y.; Paris, A. R.; Kim, D.; Yang, P.; Yaghi, O. M.; Chang, C. J. *Science* **2015**, *349*, 1208–1213.

25. Deng, X.; Fang, Y.; Lin, S.; Cheng, Q.; Liu, Q, Zhang, X. *ACS Appl. Mater. Interfaces* **2017**, *9*, 3514−3523.

26. Peng, P.; Zhou, Z.; Guo, J.; Xiang, Z. *ACS Energy Lett.* **2017**, *2*, 1308−1314.

27. Huang, N.; Krishna, R.; Jiang, D. *J. Am. Chem. Soc.* **2015**, *137*, 7079−7082.

28. Zhao, S.; Dong, B.; Ge, R.; Wang, C.; Song, X.; Ma, W.; Wang, Y.; Hao, C.; Guoc, X.; Gao, Y. *RSC Adv.* **2016**, *6*, 38774−38781.

29. Kosal, M. E.; Chou, J.-H.; Wilson, S. R.; Suslick, K. S. *Nature Materials* **2002**, *1*, 118−121.

30. Suslick, K. S.; Bhyrappa, P.; Chou, J.-H.; Kosal, M. E.; Nakagaki, S.; Smithenry. D. W.; Wilson, S. R. *Acc. Chem. Res.* **2005**, *38*, 283−291.

31. Choi, E.-Y.; Barron, P. M. Novotny, R. W.; Son, H.-T.; Hu, C.; Choe, W. *Inorg. Chem.* **2009**, *48*, 426-428.
32. Spoerke, E. D.; Small, L. J.; Foster, M. E.; Wheeler, J.; Ullman, A. M.; Stavila, V.; Rodriguez, M.; Allendorf, M. D. *J. Phys. Chem. C* **2017**, *121*, 4816−4824.
33. Berg, K.; Selbo, P. K.; Weyergang, A.; Dietze, A.; Prasmickaite, L.; Bonsted, A.; Engesaeter, B. Ø.; Angellpetersen, E.; Warloe, T.; Frandsen, N.; Høgset, A. *J. Microscopy* **2005**, *218*, 133–147.
34. Jeong, H.-G.; Choi, M.-S.; *Israel J. Chem.* **2015**, *56*, 110–118.
35. Castano, A. P.; Demidova, T. N.; Hamblin, M. R. *Photodiagnosis Photodyn Ther*. **2004**, *1*, 279–293.
36. Penon, O.; Marín, M. J.; Russell, D. A.; Pérez-García, L. *J. Colloid Interface Sci.* **2017**, *496*, 100–110.
37. Seki, S.; Maeda, K.; Tagawa, S.; Kudoh, H.; Sugimoto, M.; Morita, Y.; Shibata, H. *Adv. Mater*. **2001**, *13*, 1663–1665.
38. Seki, S.; Tsukuda, S.; Maeda, K.; Matsui, Y.; Saeki, A.; Tagawa, S. *Phys. Rev. B* **2004**, *70*, 144203.
39. Seki, S.; Tsukuda, S.; Maeda, K.; Tagawa, S.; Shibata, H.; Sugimoto, M.; Jimbo, K.; Hashitomi, I.; Kohyama, A. *Macromolecules* **2005**, *38*, 10164–10170.
40. Omichi, M.; Asano, A.; Tsukuda, S.; Takano, K.; Sugimoto. M.; Saeki, A.; Sakamaki, D.; Onoda, A.; Hayashi, T.; Seki, S. *Nat. Commun.* **2014**, *5*, 3718.
41. Maeyoshi, Y.; Saeki, A.; Suwa, S.; Omichi, M.; Marui, H.; Asano, A.; Tsukuda, S.; Sugimoto, M.; Kishimura, A.; Kataoka, K.; Seki, S. *Sci. Rep.* **2012**, *2*, 600.
42. Sakaguchi, S.; Sakurai, T.; Ma, J.; Sugimoto, M.; Yamaki, T.; Chiba, A.; Saito, Y.; Seki, S. *J. Phys. Chem. B* **2018**, *122*, 8614–8623.

43. Huyang, G.; Canning, J.; Gibson, B. C.; Khoury, T.; Sum, T. J.; Neto, C.; Crossley, M. J. *Nanotechnology* **2009**, *20*, 485301.

44. Rahman, M. Z.; Kibria, M. G.; Mullins, C. B. *Chem. Soc. Rev.* **2020**, *49*, 1887–1931.

45. Ghosh, S.; Nakada, A.; Springer, M. A.; Kawaguchi, T.; Suzuki, K.; Kaji, H.; Baburin, I.; Kuc, A.; Heine, T.; Suzuki, H.; Abe, R.; Seki, S. *J. Am. Chem. Soc.* **2020**, *142*, 9752–9762.

46. Li, H.; Zhao, Y.; Jia, Y.; Qu, C.; Li, J. *Chem. Commun.* **2019**, *55*, 15057–15060.

47. Li, H.; Zhao, J.; Wang, A.; Li, Q.; Cui, W. *Colloids Surf. A* **2020**, *590*, 124486.

48. Asano, A.; Omichi, M.; Tsukuda, S.; Takano, K.; Sugimoto, M.; Saeki, A.; Seki, S. *J. Phys. Chem. C* **2012**, *116*, 17274−17279.

49. Takeshita, Y.; Sakurai, T.; Asano, A.; Takano, K.; Omichi, M.; Sugimoto, M.; Seki, S. *Adv. Mater. Lett.* **2015**, *6*, 99–103.

50. Sakaguchi, S.; Sakurai, T.; Idesaki, A.; Koshikawa, H.; Sugimoto, M.; Seki, S. *J. Photopolym. Sci. Technol.* **2020**, *33*, 91–96.

51. Mitsui, H.; Hosoi, F.; Hagiwara, M.; Kagiya, T. *J. Polym. Sci. A* **1968**, *6*, 2881–2888.

52. Mitsui, H.; Machi, S.; Hagiwara, M.; Kagiya, T. *J. Polym. Sci. A* **1967**, *5*, 1073–1082.

53. Dorfman, L. M.; Wahl, A. C. *Radiat. Res.* **1956**, *10*, 680–690.

54. Saitoh, Y.; Mizuhashi, K.; Tajima, S. *Nuclear Instruments and Methods in Phys. Res. A* **2000**, *452*, 61–66.

55. Magno, L. N.; Bezerra, F. C.; Freire, L. E. S.; Guerra, R. A.; Bakuzis, A. F.; Gonçalves, P. J. *J. Phys. Chem. A* **2017**, *121*, 1924−1931.

56. Horio, A.; Sakurai, T.; Lakshmi, G. B. V. S.; Avasthi, D. K.; Sugimoto, M.; Yamaki, T.; Seki, S. *Nanoscale* **2016**, *8*, 14925–14931.

57. Seki, S.; Saeki, A.; Sakurai, T.; Sakamaki, D. *Phys. Chem. Chem. Phys.* **2014**, *16*, 11093–11113.

58. Kim, S.; Fujitsuka, M.; Majima, T. *J. Phys. Chem. B* **2013**, *117*, 13985–13992.

59. Bastus, N. G.; Piella, J.; Puntes, V. *Langmuir* **2016**, *32*, 290−300.

60. Kroeze, J. E.; Savenije, T. J.; Warman, J. M. *J. Photochem. Photobiol. A* **2002**, *148*, 49–55.

61. Kim, S.; Fujitsuka, M.; Majima, T. *J. Phys. Chem. B*, **2013**, *117*, 13985–13992.

62. Bastus, N. G.; Piella, J.; Puntes, V. *Langmuir* **2016**, *32*, 290−300.

63. C. D. Geddes, J. R. Lakowicz, *J. Fluorescence* **2002**, *12*, 121–129.

64. Min, S.-Y.; Kim, T.-S.; Lee, Y.; Cho, H.; Xu, W.; Lee, T.-W. *Small* **2015**, *11*, 45–62.

Chapter 3 Appendix

1. Synthesis

1.1. Summarized Synthetic Schemes

Synthesis of Porphyrin Derivatives 2, 3, 4, 5, and 6.

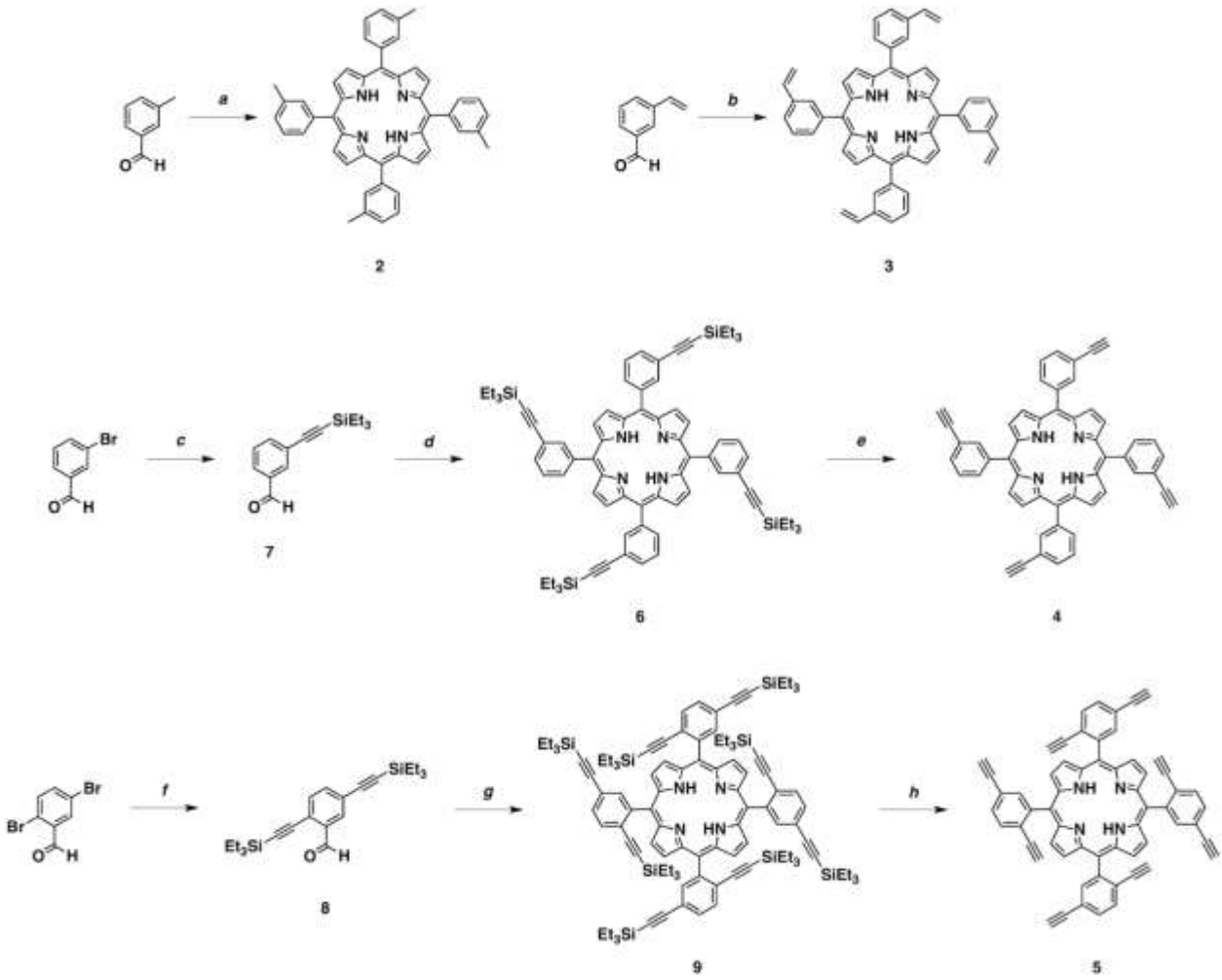

Reagents and Conditions: (a) BF_3•OEt_2, CH_2Cl_2, 25 °C, then DDQ, 25 °C; (b) triethylsilylacetylene, EtN_3, reflux; (c) BF_3•OEt_2, CH_2Cl_2, 25 °C, then DDQ, 25 °C; (d) TBAF, THF, 0 °C; (e) triethylsilylacetylene, EtN_3, reflux; (f) BF_3•OEt_2, CH_2Cl_2, 25 °C, then DDQ, 25 °C; (g) TBAF, THF, 0 °C.

1.2. Synthesis of Compound 2

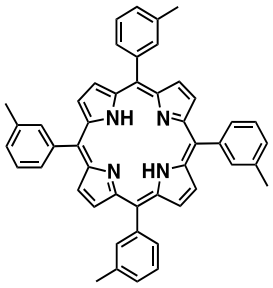

2

To a CH_2Cl_2 solution (700 mL) of a mixture of 3-methylbenzaldehyde (1.24 g, 10.3 mmol) and pyrrole (0.69 g, 10.3 mmol) at 25 °C was added $BF_3 \cdot OEt_2$ (75 μL) and the mixture was stirred for 4 h under N_2. Then, 2,3-dichloro-5,6-dicyano-1,4-benzoquinone (DDQ; 9.35 g, 41.2 mmol) was added and the reaction mixture was stirred for 10 min. The reaction mixture was filtered through alumina gel and evaporated to dryness under reduced pressure. The residue was subjected to column chromatography on silica gel using hexane/$CHCl_3$ (1/1 v/v) as an eluent and evaporated to dryness under reduced pressure. The residue was recrystallized from $CHCl_3$/MeOH, to allow isolation of **2** as reddish purple solid (508 mg, 0.76 mmol, 29%). ^{1}H NMR ($CDCl_3$) δ 8.85 (s, 8H, β-H), 7.99–8.05 (m, 8H, Ar-H), 7.56–7.65 (m, 8H, Ar-H), 2.64 (s, 12H, CH_3), –2.78 (s, 2H, NH); MALDI-TOF MS *m*/*z* calcd. for $C_{48}H_{38}N_4$ $[M]^+$ 670.31, found 670.94.

1.3. Synthesis of Compound 3

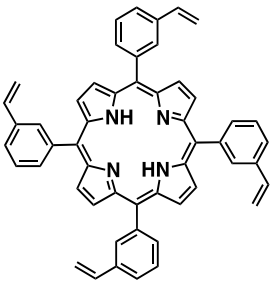

3

To a CH_2Cl_2 solution (1400 mL) of a mixture of 3-vinylbenzaldehyde (2.50 g, 18.9 mmol) and pyrrole (1.27 g, 18.9 mmol) at 25 °C was added $BF_3 \cdot OEt_2$ (150 μL) and the mixture was stirred for 4 h under N_2. Then, DDQ (17.2 g, 75.7 mmol) was added and the reaction mixture was stirred for 10 min. The reaction mixture was filtered through alumina gel and evaporated to dryness under reduced pressure. The residue was subjected to column chromatography on silica gel using hexane/$CHCl_3$ (1/1 v/v) as an eluent and evaporated to dryness under reduced pressure. The residue was reprecipitated from $CHCl_3$/MeOH, to allow isolation of **3** as reddish purple solid (1.39 g, 1.93 mmol, 41%). ^{1}H NMR ($CDCl_3$) δ 8.87 (s, 8H, β-H), 8.26 (s, 4H, Ar-H), 8.11 (d, *J* = 7.8 Hz, 4H, Ar-H), 7.84 (d, J = 7.8 Hz, 4H, Ar-H), 7.71 (t, *J* = 7.6 Hz, 4H, Ar-H), 6.98 (dd, *J* = 11.0, 17.8 Hz, 4H, C–C*H*=CH_2), 5.96 (d, *J* = 17.6 Hz, 4H, C–CH=C*H*$_2$), 5.40 (d, *J* = 10.7 Hz, 4H, C–CH=C*H*$_2$), –2.78 (s, 2H, NH); MALDI-TOF MS *m*/*z* calcd. for $C_{52}H_{38}N_4$ $[M]^+$ 718.31, found 718.72.

1.4. Synthesis of Compound 7

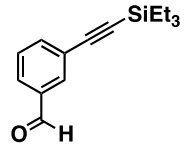

7

To a Et_3N solution (100 mL) of 3-bromobenzaldehyde (3.00 g, 16.2 mmol) were successively added triethylsilylacetylene (3.41 g, 24.3 mmol), $Pd(PPh_3)_4$ (0.94 g, 0.81 mmol), and CuI (0.62 g, 3.24 mmol), and the mixture was refluxed for 3 h under N_2. Then, the reaction mixture was cooled down to 25 °C and poured into hexane (200 mL)/ether (50 mL). The resultant mixture was filtered off from insoluble fractions and evaporated to dryness under reduced pressure. The residue was subjected to column chromatography on silica gel using hexane/CH_2Cl_2 (2/1 v/v) as an eluent, to allow isolation of **7** as pale yellow liquid (3.64 g, 14.9 mmol, 92%). ^{1}H NMR ($CDCl_3$) δ 10.0 (s, 1H, CHO), 7.97 (s, 1H, Ar-H), 7.83 (d, J = 7.8 Hz, 1H, Ar-H), 7.72 (d, J = 7.8 Hz, 1H, Ar-H), 7.48 (t, J = 7.8 Hz, 1H, Ar-H), 0.87–0.89 (t, J = 6.5 Hz, 3H, CH_2).

1.5. Synthesis of Compound 6

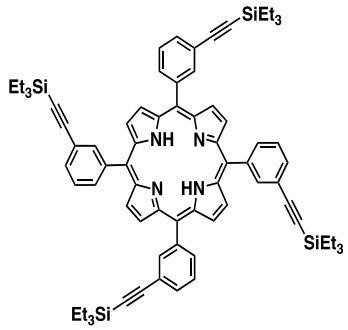

6

To a CH_2Cl_2 solution (1100 mL) of a mixture of **7** (3.76 g, 16.8 mmol) and pyrrole (1.12 g, 16.8 mmol) at 25 °C was added $BF_3 \cdot OEt_2$ (120 μL) and the mixture was stirred for 4 h under N_2. Then, DDQ (9.35 g, 41.2 mmol) was added and the reaction mixture was stirred for 10 min. The reaction mixture was filtered through alumina gel and evaporated to dryness under reduced pressure. The residue was subjected to column chromatography on silica gel using hexane/$CHCl_3$ (1/1 v/v) as an eluent and evaporated to dryness under reduced pressure. The residue was reprecipitated from $CHCl_3$/MeOH, to allow isolation of **6** as reddish purple solid (2.00 g, 1.71 mmol, 41%). ^{1}H NMR ($CDCl_3$) δ 8.84 (s, 8H, β-H), 8.33 (s, 4H, Ar-H), 8.14 (d, J = 7.8 Hz, 4H, Ar-H), 7.90 (d, J = 7.8 Hz, 4H, Ar-H), 7.69 (t, J = 7.6 Hz, 4H, Ar-H), 1.05 (t, J = 7.8 Hz, 36H, CH_3), 0.69 (q, J = 7.8 Hz, 24H, CH_2), –2.86 (s, 2H, NH); MALDI-TOF MS m/z calcd. for $C_{76}H_{86}N_4Si_4$ $[M]^+$ 1166.59, found 1167.457.

1.6. Synthesis of Compound 4

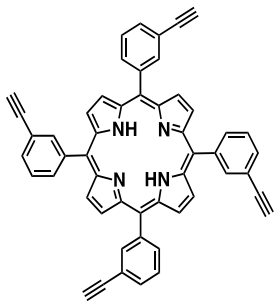

4

To a THF solution (50 mL) of a **6** (0.40 g, 0.34 mmol) at 0 °C was added a THF solution of tetrabutylammonium fluoride (2.0 mL, 1 M), and the mixture was stirred for 12 h under N_2 at 25 °C. Then, the reaction mixture was poured into water and extracted with $CHCl_3$. The organic extract was washed with brine, dried over Na_2SO_4, and evaporated to dryness under reduced pressure. The residue was subjected to column chromatography on silica gel using hexane/$CHCl_3$ (1/1 v/v) as an eluent and evaporated to dryness under reduced pressure. The residue was reprecipitated from $CHCl_3$/MeOH, to allow isolation of **4** as reddish purple solid (0.17 g, 71%). ^{1}H NMR ($CDCl_3$) δ 8.84 (s, 8H, β-H), 8.36 (s, 4H, Ar-H), 8.19 (d, J = 7.8 Hz, 4H, Ar-H), 7.93 (d, J = 7.8 Hz, 4H, Ar-H), 7.72 (t, J = 7.6 Hz, 4H, Ar-H), 3.17 (s, 4H, ≡CH), –2.86 (s, 2H, NH); MALDI-TOF MS m/z calcd. for $C_{52}H_{30}N_4$ $[M]^+$ 710.25, found 710.59.

1.7. Synthesis of Compound 8

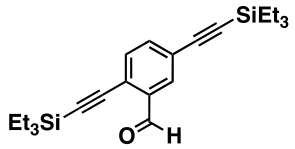

8

To a Et_3N solution (100 mL) of 2,5-dibromobenzaldehyde (2.50 g, 9.47 mmol) were successively added triethylsilylacetylene (2.92 g, 20.8 mmol), $Pd(PPh_3)_4$ (1.1 g, 0.95 mmol), and CuI (0.54 g, 2.84 mmol), and the mixture was refluxed for 12 h under N_2. Then, the reaction mixture was cooled down to 25 ℃ and poured into hexane (200 mL)/ether (50 mL). The resultant mixture was filtered off from insoluble fractions and evaporated to dryness under reduced pressure. The residue was subjected to column chromatography on silica gel using hexane/$CHCl_3$ (2/1 v/v) as an eluent, to allow isolation of **8** as pale yellow liquid (3.45 g, 9.02 mmol, 95%). ^{1}H NMR ($CDCl_3$) δ 10.5 (s, 1H, CHO), 7.98 (d, J = 2.0 Hz, 1H, Ar-H), 7.59 (dd, J = 2.0, 8.3 Hz, 1H, Ar-H), 7.51 (d, J = 8.3 Hz, 1H, Ar-H), 1.06 (t, J = 7.8 Hz, 9H, CH_3), 1.04 (t, J = 7.8 Hz, 9H, CH_3), 0.71 (q, J = 8.0 Hz, 6H, CH_2), 0.68 (q, J = 8.0 Hz, 6H, CH_2).

1.8. Synthesis of Compound 9

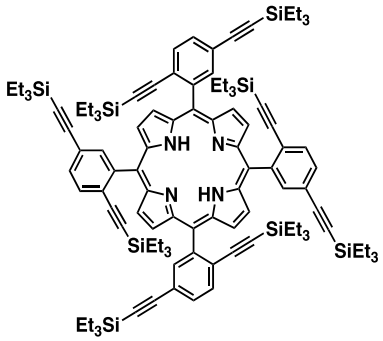

9

To a CH_2Cl_2 solution (700 mL) of a mixture of **8** (3.80 g, 9.93 mmol) and pyrrole (0.67 g, 9.93 mmol) at 25 °C was added $BF_3 \cdot OEt_2$ (75 μL) and the mixture was stirred for 4 h under N_2. Then, DDQ (9.02 g, 39.7 mmol) was added and the reaction mixture was stirred for 10 min. The reaction mixture was filtered through alumina gel and evaporated to dryness under reduced pressure. The residue was subjected to column chromatography on silica gel using hexane/$CHCl_3$ (2/1 v/v) as an eluent and evaporated to dryness under reduced pressure. The residue was reprecipitated from $CHCl_3$/MeOH, to allow isolation of **9** as reddish purple solid (1.02 g, 0.59 mmol, 24%). Compound **9** includes three stereoisomers, affording a complicated NMR spectrum. ^{1}H NMR ($CDCl_3$) δ 8.67–8.73 (s x 3, 8H, β-H), 8.24–8.10 (4H, Ar-H), 7.89–7.78 (8H, Ar-H), 1.05–0.98 (36H, CH_3), 0.71–0.62 (24H, CH_2), –0.17~–0.82 (60H, CH_2, CH_3), –2.73, –2.77 (s × 2, 2H, NH); MALDI-TOF MS *m*/*z* calcd. for $C_{108}H_{142}N_2Si_8$ $[M]^+$ 1718.94, found 1719.79.

1.9. Synthesis of Compound 5

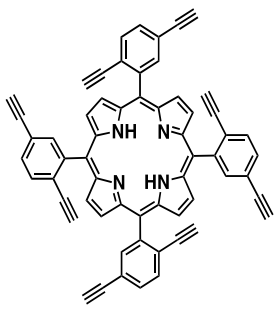

5

To a THF solution (60 mL) of a **3** (0.50 g, 0.29 mmol) at 0 °C was added a THF solution of tetrabutylammonium fluoride (3.5 mL, 1 M), and the mixture was stirred for 6 h under N_2 at 25 °C. Then, the reaction mixture was poured into water and extracted with $CHCl_3$. The organic extract was washed with brine, dried over Na_2SO_4, and evaporated to dryness under reduced pressure. The residue was subjected to column chromatography on silica gel using $CHCl_3$ as an eluent and evaporated to dryness under reduced pressure. The residue was reprecipitated from THF/MeOH, to allow isolation of **5** as reddish brown solid (0.17 g, 73%). Compound **5** includes three stereoisomers, affording a complicated NMR spectrum. ^{1}H NMR (THF-d_8) δ 8.78–8.73 (8H, β-H), 8.36–8.25 (4H, Ar-H), 7.96–7.90 (8H, Ar-H), 3.82–3.80, 2.74–2.65 (8H, ≡CH), –2.70 (s, 2H, NH); MALDI-TOF MS *m*/*z* calcd. for $C_{60}H_{30}N_4$ $[M]^+$ 806.25, found 807.12.

2. Figures

2.1. Evaluation of Nanowire Radii

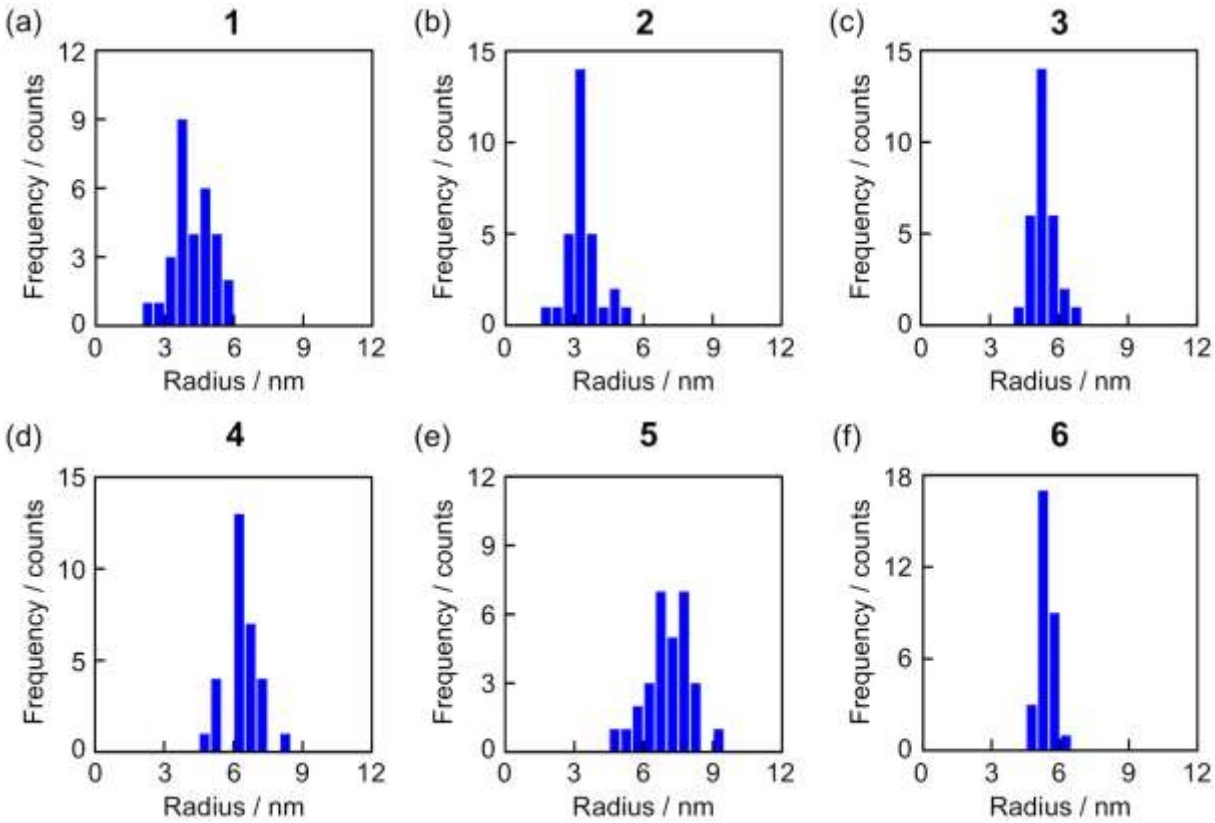

Figure S1. Radius distributions of nanowires fabricated by irradiation with 490 MeV $^{192}Os^{30+}$ particles and development with benzene for **1**–**5** and hexane for **6**.

Table S1. Averaged radii (r) and aspect ratios (r_x/r_y) of nanowires from **1**–**6** fabricated by irradiation with 490 MeV $^{192}Os^{30+}$ particles and development with benzene for **1**–**5** and hexane for **6**.

Starting Compound	r / nm	r_x/r_y
1	4.2 ± 0.9	2.1 ± 0.4
2	3.4 ± 0.7	2.2 ± 0.6
3	5.4 ± 0.5	1.8 ± 0.3
4	6.4 ± 0.7	1.4 ± 0.3
5	7.1 ± 0.9	1.7 ± 0.5
6	5.4 ± 0.4	1.3 ± 0.1

2.2. Evaluation of End-to-End Distances of Nanowires

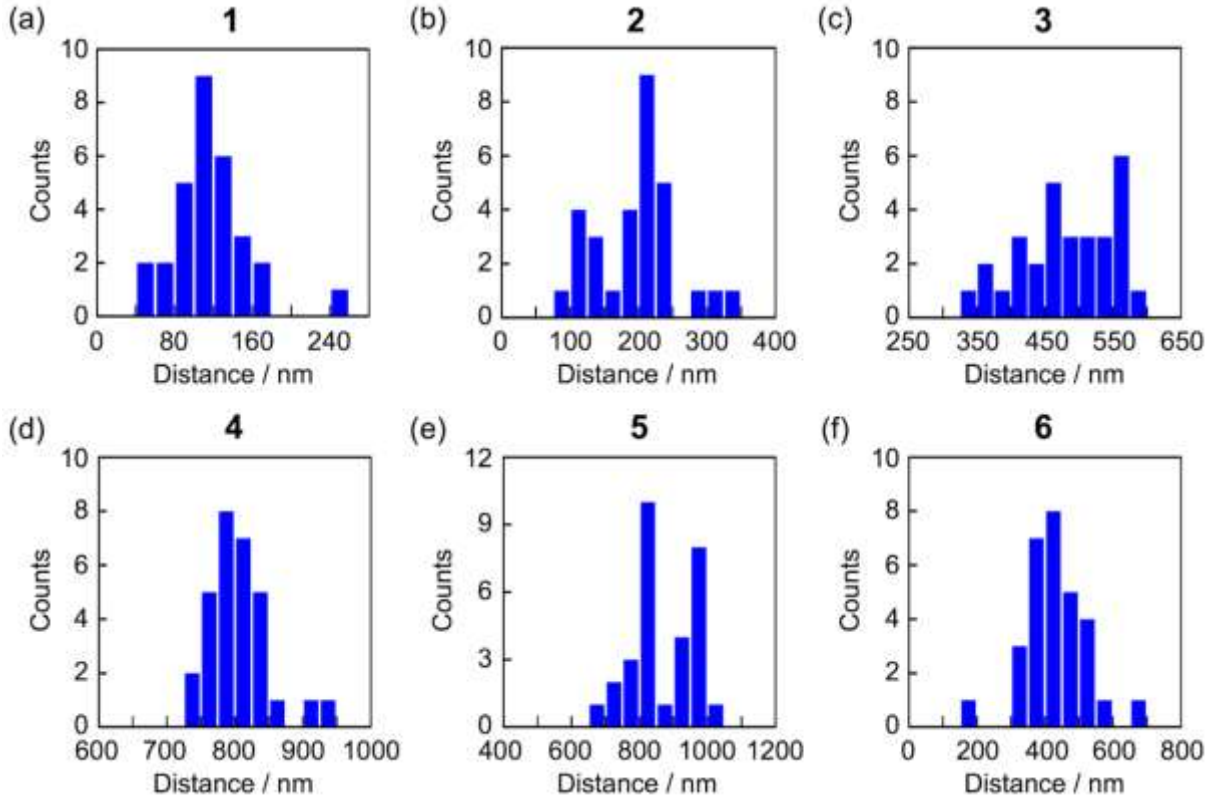

Figure S2. Distributions of end-to-end distances of nanowires fabricated by irradiation with 490 MeV $^{192}Os^{30+}$ particles and development with benzene for **1**–**5** and hexane for **6**. The averaged lengths of nanowires are 163, 294, 628, 831, 926, and 527 for **1**–**6**, respectively (see **Table 1**).

2.3. Evaluation of Rigidity of Nanowires

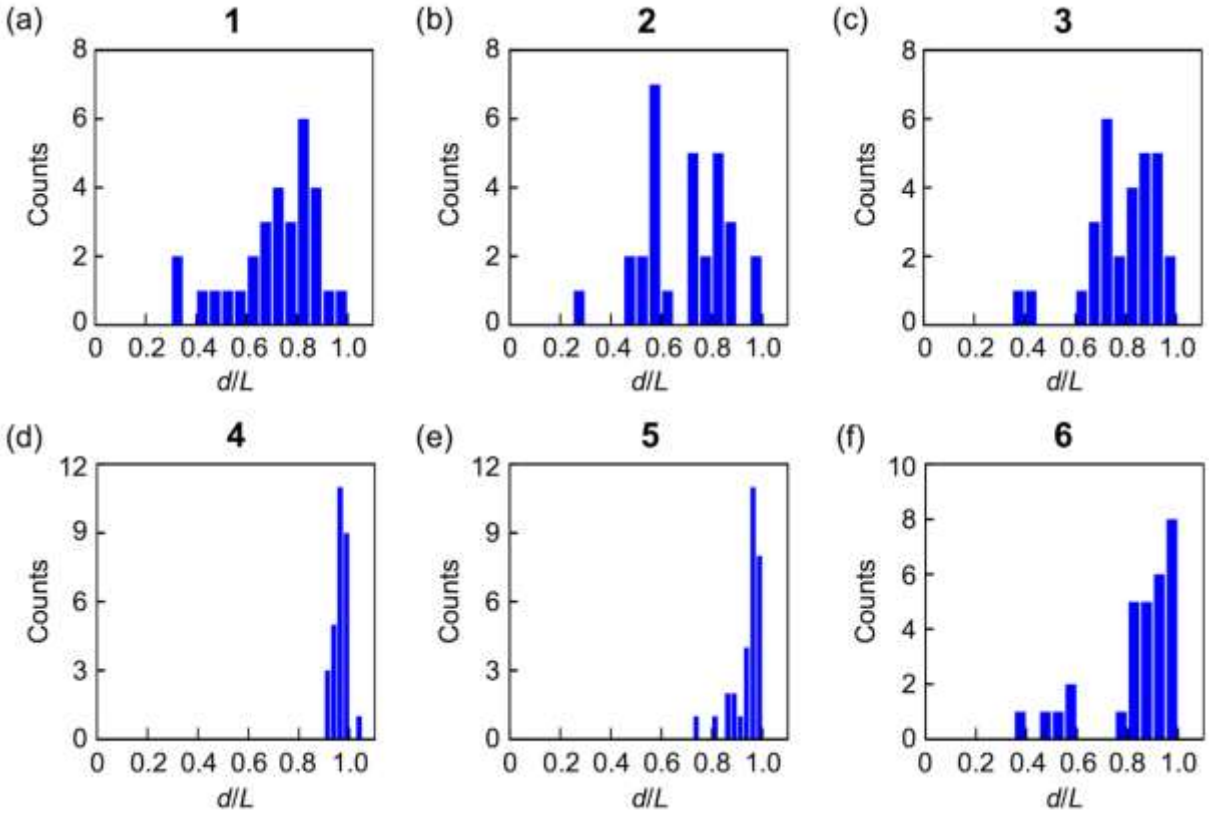

Figure S3. Distributions of *d*/*L* values (*d*: end-to-end distance, *L*: length) of nanowires for **1**–**6** fabricated by irradiation with 490 MeV $^{192}Os^{30+}$ particles and development with benzene for **1**–**5** and hexane for **6**.

2.4. Scanning Electron Microscopy Images of Nanowires

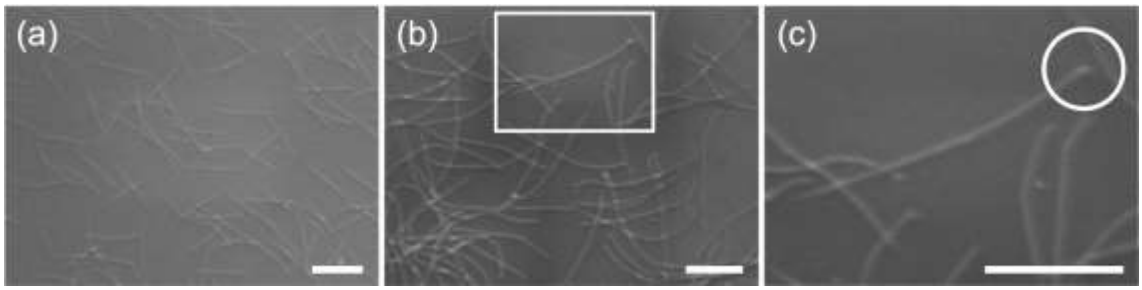

Figure S4. SEM images of nanowires from spincoat film of (a) **4** and dropcast film of (b, c) **5**. The film was irradiated with 490 MeV $^{192}Os^{30+}$ particles at the fluence of 1.0×10^9 ions cm^{-2} and developed with benzene. Scale bars indicate 500 nm. (c) is a magnified image of the square area indicated in (b). Connection of a nanowire terminal with the substrate was visible at the position indicated in the circle in (c).

2.5. Disjointed Nanowires from Substrate by Ultrasonication

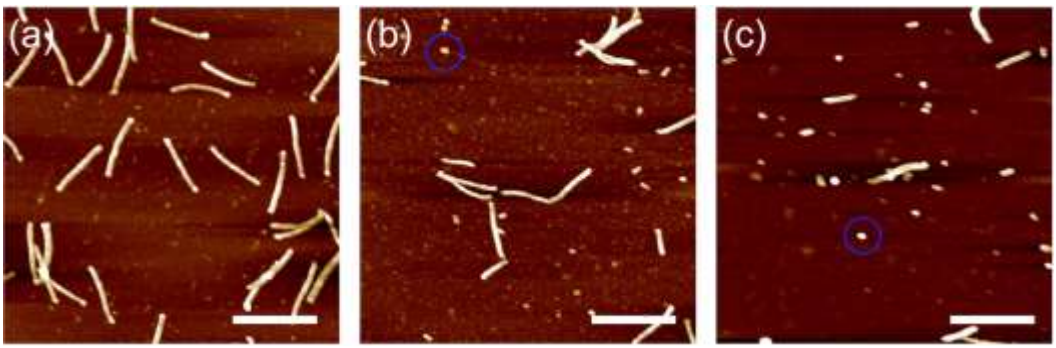

Figure S5. AFM topographic images of nanowires from spincoated film of **4**. The film was irradiated with 490 MeV $^{192}Os^{30+}$ particles at the fluence of 1.0×10^9 ions cm^{-2}, and developed (a) with $CHCl_3$, then with sonication in $CHCl_3$ for (b) 10 min, and (c) further 20 min. Scale bars indicate 500 μm. Blue circles indicate examples of "root"-like nanoobjects. Also fragmented nanowires are seen.

2.6. Nanowire Formation with Lower Energy Ion Irradiation

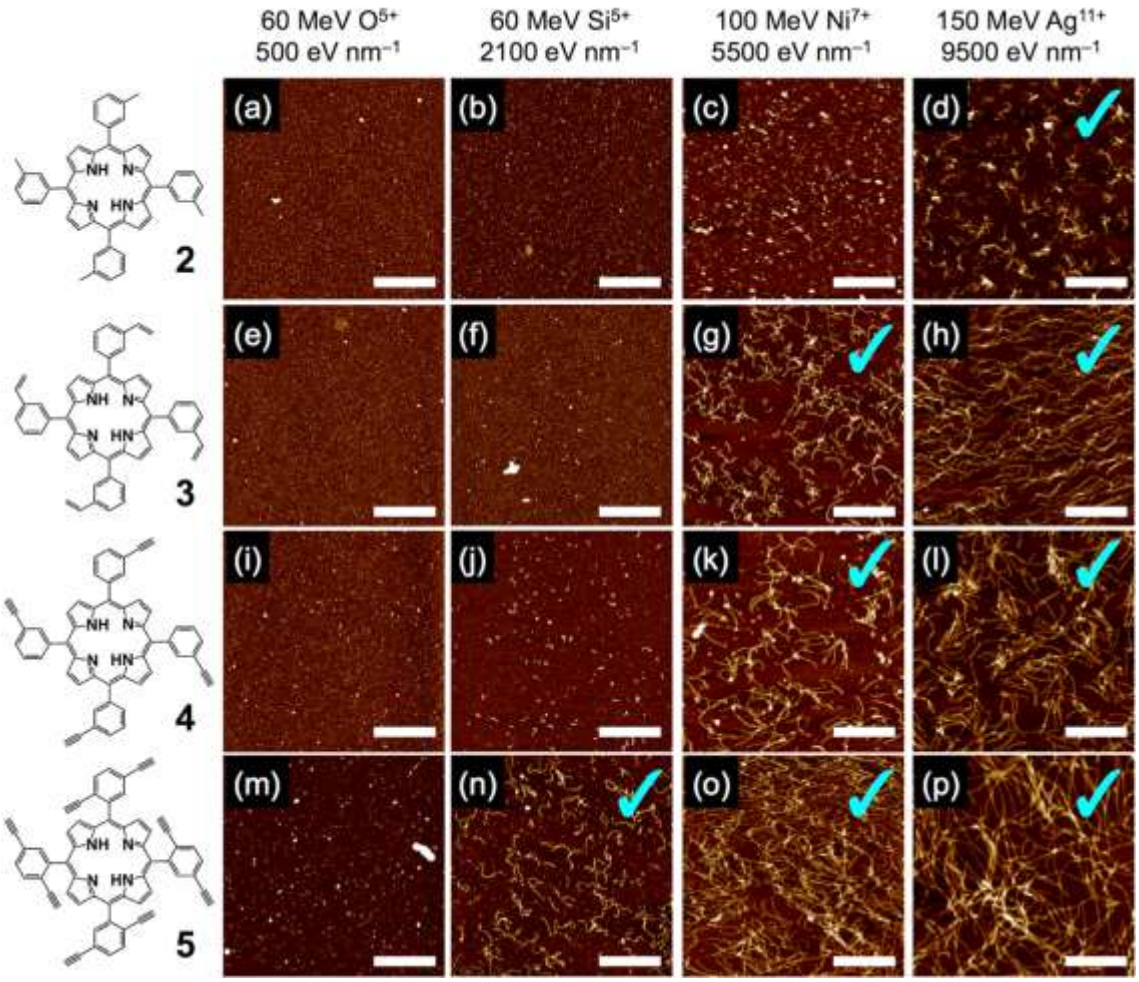

Figure S6. AFM topographic images of nanowires from thin films of (a–d) **2**, (e-h) **3**, (i–l) **4**, and (m–p) **5**. The films were irradiated with (a, e, i, m) 60 MeV $^{16}O^{5+}$, (b, f, j, n) 60 MeV $^{28}Si^{5+}$, (c, g, k, o) 100 MeV $^{58}Ni^{7+}$, and (d, h, l, p) 150 MeV $^{107}Ag^{11+}$ particles at the fluence of 5.0×10^9 ions cm^{-2} and developed with *n*-hexane for **2** and benzene for **3**-**5**. Scale bars represent 500 nm. Check marks indicate successful nanowire isolation.

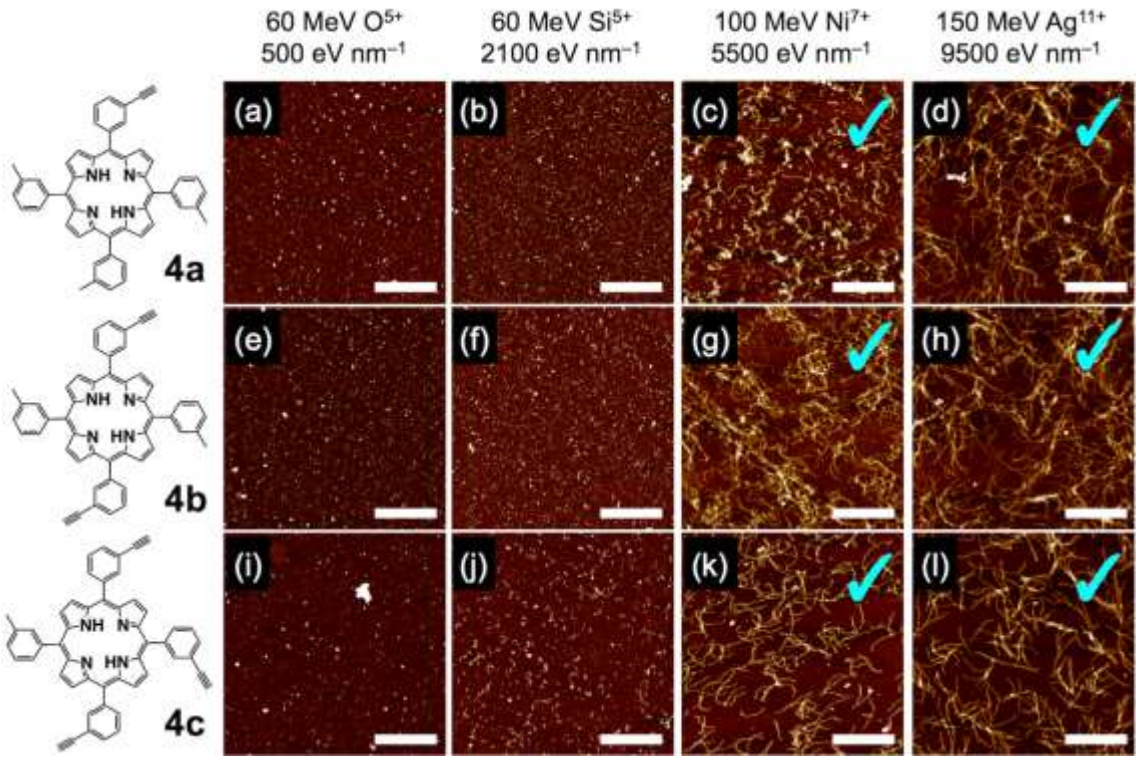

Figure S7. AFM topographic images of nanowires from thin films of reference compounds, (a–d) **4a**, (e–h) **4b**, and (i–l) **4c**. The films were irradiated with (a, e, i,) 60 MeV O^{5+}, (b, f, j) 60 MeV Si^{5+}, (c, g, k) 100 MeV Ni^{7+}, and (d, h, l) 150 MeV Ag^{11+} particles at the fluence of 5.0 × 10^9 ions cm^{-2} and developed with benzene. Scale bars represent 500 nm. Check marks indicate obvious nanowire isolation.

2.7. Morphology of Nanowires Used for Spectroscopic Measurements

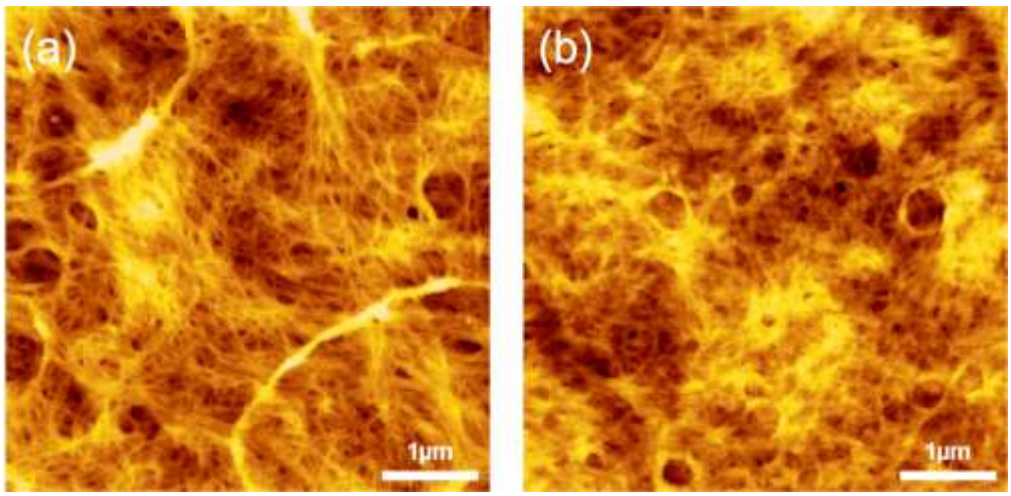

Figure S8. AFM topographic images of nanowires from dropcast films of (a) **4** and (b) **6**. The film was irradiated with 490 MeV $^{192}Os^{30+}$ particles at the fluence of 1.0×10^{10} ions cm^{-2}, and developed with $CHCl_3$ for (a) and *n*-hexane for (b). Scale bars indicate 1 μm.

2.8. Absorption, Excitation, and Emission Spectra of Porphyrin Nanowires

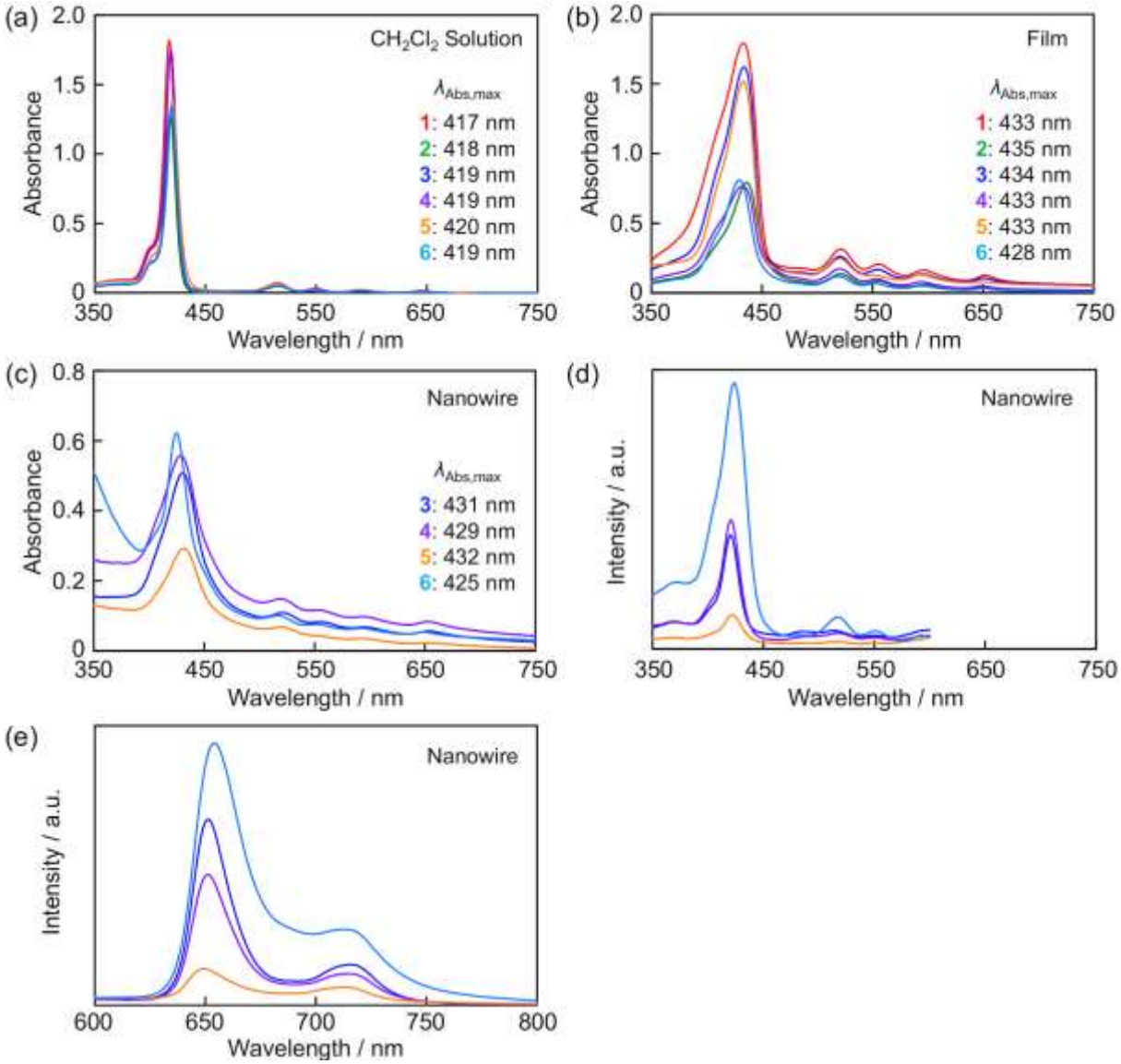

Figure S9. Electronic absorption spectra with wavelength of absorption maxima of (a) CH_2Cl_2 solution, (b) spin-coated thin film, and (c) bundled nanowires for **1** (red), **2** (green), **3** (blue), **4** (purple), **5** (orange), and **6** (pale blue). (d) Excitation (λ_{em} = 651 nm) and (e) emission (λ_{ex} = 420 nm) spectra of bundled nanowires from **3** (blue), **4** (purple), **5** (orange), and **6** (pale blue). The relatively low solubility of **1** and **2** caused a trouble to obtain only thin films and thus yielded nanowires with short lengths, which results in the low spectroscopic sensitivity insufficient for characterizations. Different baselines in (c) are due to the scattering of the incident light.

2.9. Morphology of Nanowires by Stepwise Developments

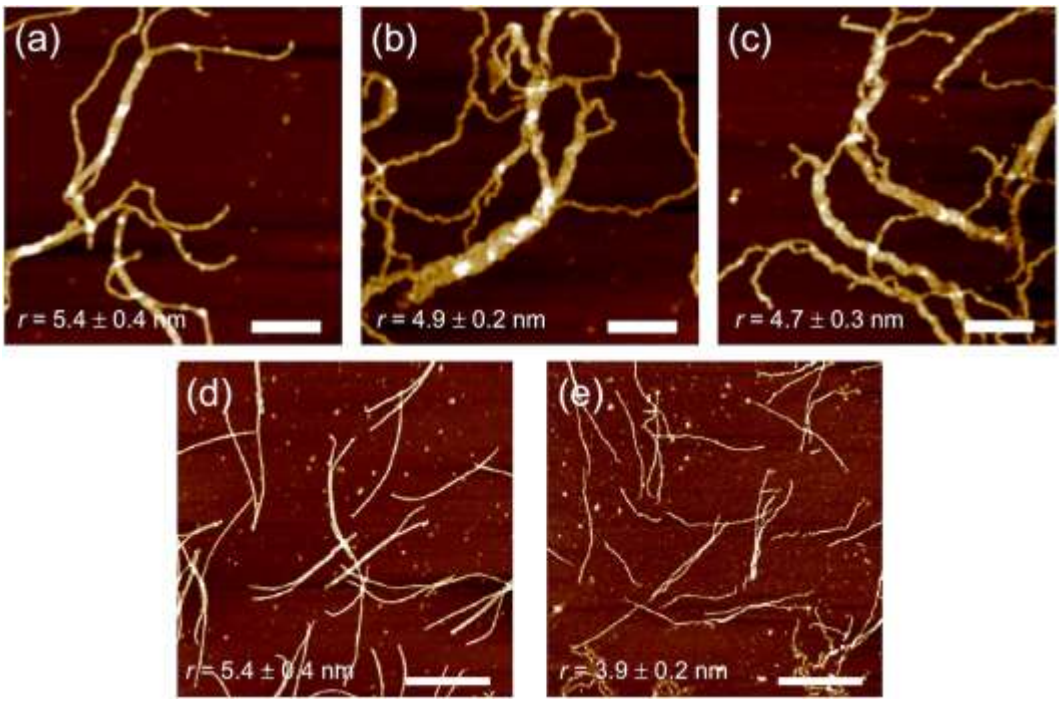

Figure S10. AFM topographic images and corresponding average cross-sectional radius of nanowires from spincoated film of **6**. The film was irradiated with 490 MeV $^{192}Os^{30+}$ particles at the fluence of 1.0×10^9 ions cm^{-2}, and developed initially (a) with *n*-hexane, then with $CHCl_3$ for (b) 30 s, and (c) further 20 min. A different rot sample was confirmed with the development condition with (d) *n*-hexane and (e) then $CHCl_3$ for 30 min. Scale bars indicate 200 and 500 nm for (a–c) and (d,e), respectively.

2.10. Absorption Spectral Changes by Stepwise Developments

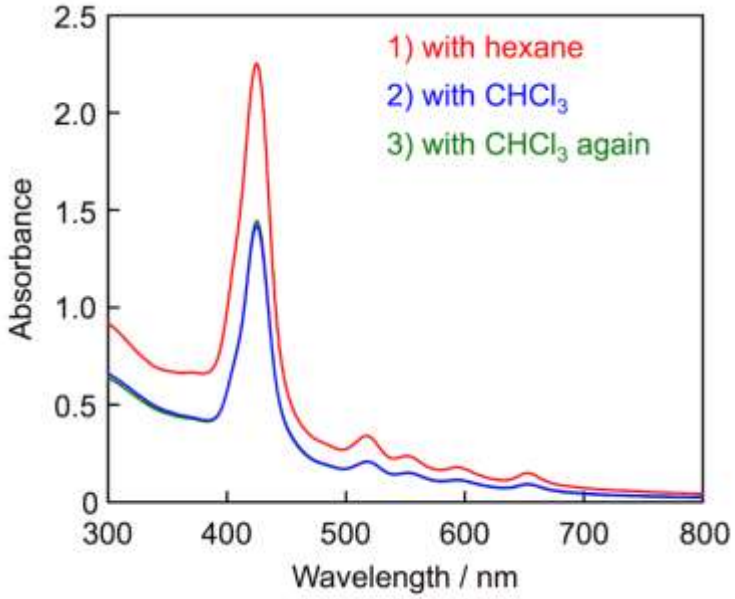

Figure S11. Electronic absorption spectra of nanowires from **6** on quartz plate. Spectra were recorded after development with hexane (red), and then with $CHCl_3$ for 10 min (blue), followed by an additional dipping in $CHCl_3$ for 1 h (green). Nanowires were fabricated by irradiation with 490 MeV $^{192}Os^{30+}$ particles at the fluence of 1.0×10^{10} ions cm^{-2}.

2.11. Size Exclusion Chromatography of Soluble Parts of Porphyrin Nanowires

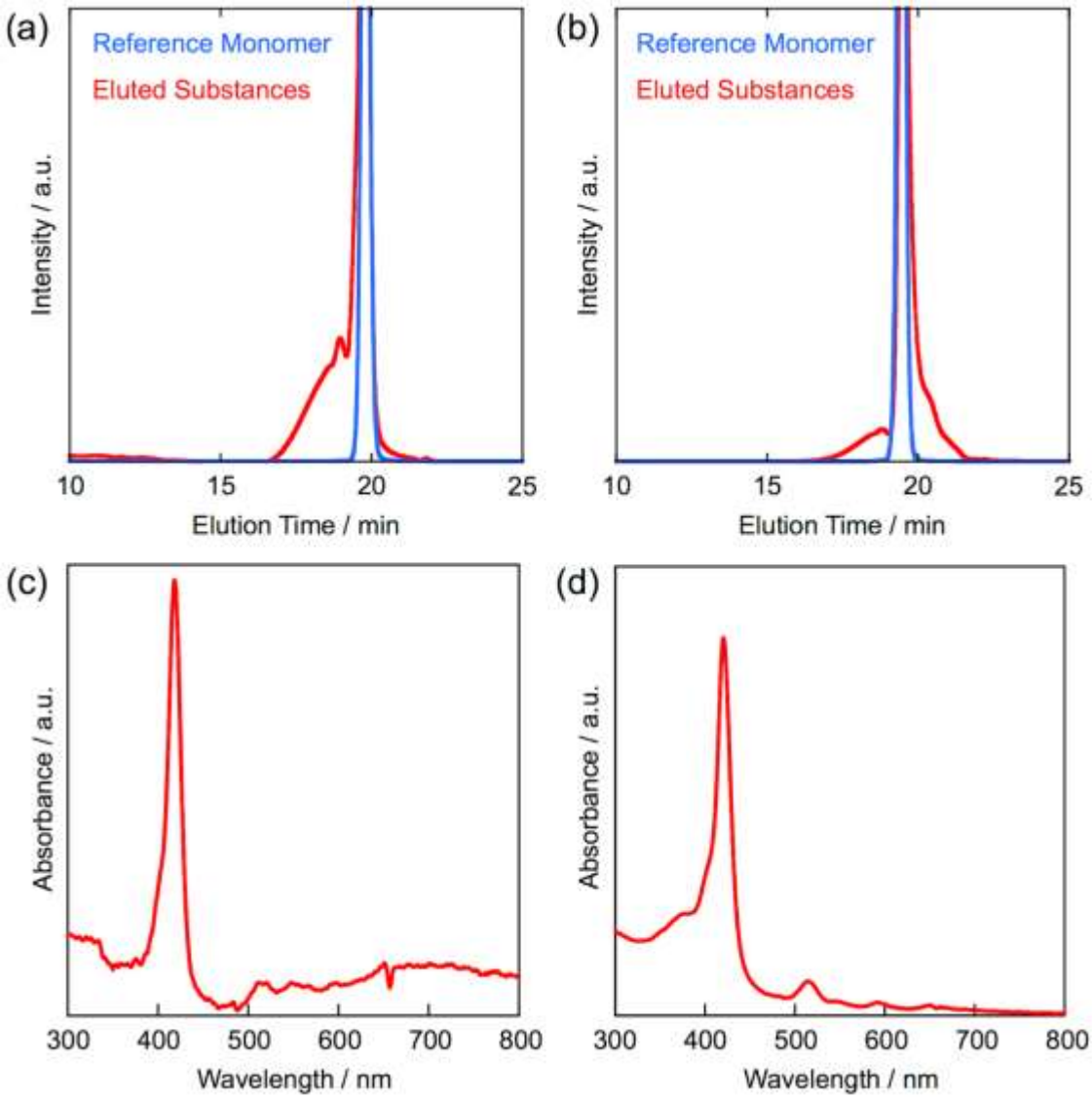

Figure S12. Analytical SEC profiles of monomers (blue) and soluble fractions of their nanowires (red) in THF for (a) **4** and (b) **5**. The formation of nanowires was confirmed by AFM after irradiation with 490 MeV $^{192}Os^{30+}$ at a fluence of 1×10^{10} ions cm^{-2} and subsequent development of the dropcast films of each compound with benzene. Then the nanowires on the Si substrate was immersed in THF, sonicated, filtered from insoluble fraction and then injected into an analytical SEC system using THF as an eluent. Retention time was monitored by UV light at 420 nm. UV-vis absorption spectra of eluted fraction corresponding to the retention peaks in the SEC trace at (c) 19.0 min for the eluted substances in (a) and (d) 18.4 min for the eluted substances in (b).

2.12. AFM Images of Nanowires from Other Ethynyl-Modified Compounds

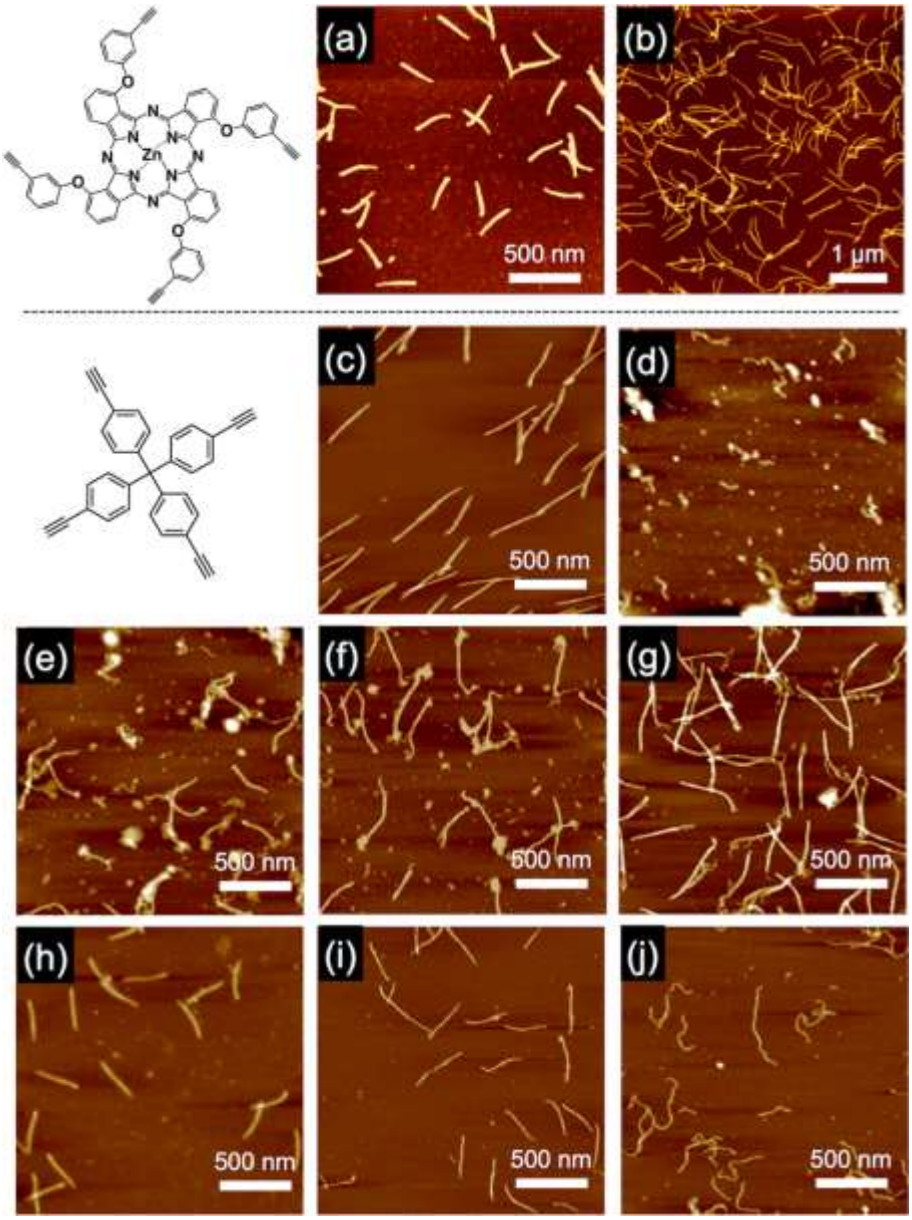

Figure S13. AFM topographic images of nanowires from ethynyl-modified (a,b) phthalocyanine and (c–g) tetraphenylmethane -based compounds. The spin-coated films were irradiated with (a–c) 490 MeV $^{192}Os^{30+}$, (d) 1.5 MeV Al_1, (e) 3.0 MeV Al_2, (f) 4.5 MeV Al_3, (g) 6.0 MeV Al_4, (h) 150 MeV $^{107}Ag^{11+}$, (i) 100 MeV $^{58}Ni^{7+}$, and (j) 60 MeV $^{28}Si^{5+}$, at a fluence of 1×10^9 and 2×10^9 ions cm^{-2} for (a, c–j) and (b), respectively, and then developed with (a,b) benzene or (c–j) toluene.

2.13. Flash-Photolysis Time-Resolved Microwave Conductivity Measurements

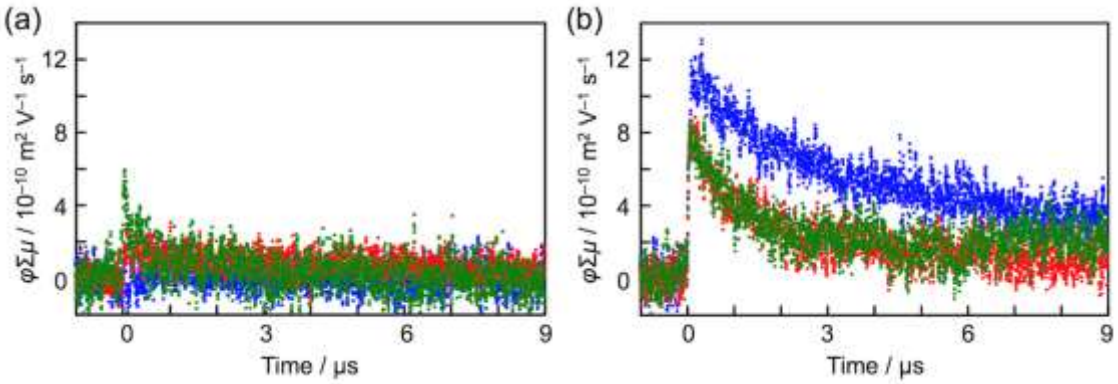

Figure S14. Conductivity transients of **3** (red), **4** (green), and **6** (blue) in (a) thin films and (b) nanowires. Nanowires were fabricated by irradiation with 490 MeV $^{192}Os^{30+}$ particles at the fluence of 1.0×10^{10} ions cm^{-2} and development with benzene.

2.14. AFM Image of Silver Nanoparticle

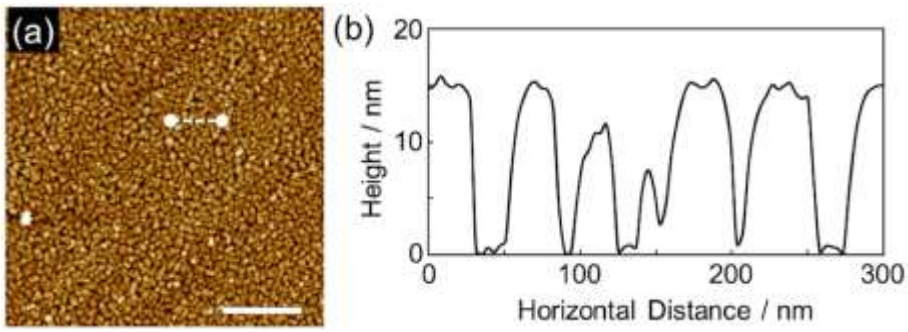

Figure S15. (a) AFM topographic image and (b) height profile (indicated as white dashed line in (a)) of Ag nanoparticles grown on quartz substrates. Scale bar in (a) represents 500 nm

Chapter 4. Fabrication of Ultralong Aligned Fullerene Nanowires Using Swift Heavy Ion Beam

Synopsis

Semiconductor nanowires have been shown to exhibit outstanding electronic, optical and magnetic properties due to their large-area surface and one-dimensional structure, which have attracted extensive interest of precise control of physical dimension and chemical composition of fabricated nanowires. This study reports a new strategy for fabrication of ultralong organic nanowires with extremely high-aspect-ratio exploiting the single-particle triggered linear polymerization (STLiP) technique. The nanowires from fullerene molecules showed over 10 μm length and 4~5 nm radius. The obtained nanowires indicated the typical n-type semiconductor behavior from field-effect transistor measurement, suggesting electron transporting as a carrier within fullerene nanowires. From temperature dependent experiments, the resistance increased as decreasing temperature in the range of 50 K ~ 300 K and the mechanism of carrier transport in relatively high temperature was assumed to be nearest-neighbor hopping. Anisotropic conductivity was also evaluated by time-resolved microwave conductivity technique and measured conductivity in case of that nanowires are parallel or perpendicular to the microwave oscillation have significant difference with ~10^2 times. Thus, this research successfully developed promising approach to fabricate ultralong nanowires which have great potential to break new ground with biosensing and photocatalysis devices.

Introduction

"Miniaturization" has played a key role of energy-, space-, and resource-saving in the integrated circuit (IC) manufacturing and semiconductor industry where reliable and reproducible nano-fabrication systems are desired for various applications in microelectronics

and bioelectronics. Nanostructures can be classified by the dimension of the structure into nanosheet (2D), nanowire/nanofiber/nanorribon/nanorod (1D), and quantum dot (0D). Especially, semiconductor nanowires have exhibited remarkable potential in optical, magnetic and electronic properties due to their surface with outstanding large specific area and anisotropic thermal/carrier transport, which have been utilized for ultrasensitive sensors,[1] drug delivery system,[2] laser,[3] spintronics,[4] and energy devices.[5,6] From the first report of producing Si whiskers made by single crystal growth in 1960s,[7] a lot of scientists have developed nanowire fabrication systems which can be defined as "top-down" or "bottom-up" approaches. Bottom-up approaches focus on chemical synthesis with nucleation and growth of building blocks (atoms, ions, and molecules), including the vapor-liquid-solid (VLS) method,[7,8] the vapor-solid-solid process,[9,10] nanohole templating,[11,12] self-assembly method.[13,14] On the other hand, top-down approaches generally exploit lithographic techniques accomplished by sculpturing or etching balk materials through X-ray or XUV,[15,16] and electron beam[17,18] irradiation. Therefore, scientists must choose the best approach considering many factors such as structure size, cost, reliability, and versatility which are usually trade-off relation. When it comes to size-controllability, top-down approaches have critical difficulties for manufacturing with sub-10-nm resolution because of the diffraction limit of radiation source. Recently, studies on focused ion beam (FIB) lithography have been emerged with advantages of smaller wavelength resulting in reduced proximity effect and high energy transfer efficiency.[19,20] In this sense, single heavy ion with MeV- or GeV-order energy can be regarded as ultimately focused and the most energetic radiation source. Actually, the interaction between charged particle (= ion) and matters have been theoretically discussed since 1930s,[21–23] which proposed that charged particles can release amount of energy within cylindrical area along ion trajectory called "ion track". Using this phenomenon, some studies accomplished fabrication of functionalized nanoholes for nanofluidic system[24] and ion-pumping system.[25] To date, unique top-down

method, named as Single-particle Triggered Linear Polymerization (STLiP), have developed, which achieved fabrication of sub-10-nm thick organic nanowires *via* polymerization reactions triggered by high-energy charged particle irradiation to organic thin films.[26–35] This technique have established precisely controlled manufacturing in terms of the length and the number density which correspond to the thickness of target thin films and the fluence of particles, respectively. However, fabrication of high-aspect-ratio nanowires with over 10 μm length have been hindered because of the difficulty of preparing such thick organic films regardless of the fact that the length and aspect ratio crucially affect the surface area of nanowires.

Herein, this study developed a novel design modifying the traditional STLiP protocol for producing ultralong nanowires from fullerene films and the nanowire shape simultaneously reached sub-10-nm thick and sur-10-μm length. The fabricated nanowires exhibited distinctive electronic properties seen in n-type semiconductors and anisotropic photoconductivity

Experimental

Materials: Buckminster fullerene C_{60} was purchased from Tokyo Chemical Industry Co. Ltd. and used without further purification. Unless otherwise noted, all commercial reagents were purchased from Wako Pure Chemical Industries Ltd., Tokyo Chemical Industry Co. Ltd., and Sigma-Aldrich Co. and used as received.

Film Preparation: Phosphine doped n-type Si wafer covered with thermally oxidized SiO_2 (200 nm thick) layer and quartz plate were used as substrates. Si/SiO_2 substrate was cut into 1.5 cm^2 square, sonicated in 2-propanol, dried, and treated with O_3 plasma prior to the use. Thin films of C_{60} were prepared by vapor deposition under ~10^{-4} Pa at the rate of 0.2−0.3 Å s^{-1}. The thickness of the films was evaluated by a Bruker Co. model Dektak 150 surface profiler.

Nanowire Fabrication: 450 MeV $^{129}Xe^{23+}$ particles were generated from a cyclotron accelerator at Takasaki Advanced Radiation Research Institute, National Institutes for Quantum and Radiological Science and Technology. The loss of kinetic energy of ions due to their traversal through the organic films was estimated using the SRIM 2010 simulation code. The prepared C_{60} films were set horizontally using a sample holder and exposed to the above ion beam in a vacuum chamber ($< 1 \times 10^{-4}$ Pa). The number of incident particles was controlled at 1.0×10^{9}–5.0×10^{11} particles cm^{-2} by setting the exposure time (s) and flux (cm^{-2} s^{-1}) calculated from the beam current, charges of the ions used, and elementary charge. Then, the irradiated films were further cut into small pieces, and developed by immersing them into organic solvents for 30 minutes or sublimation under vacuum a ($5–8 \times 10^{-3}$ Pa).

Characterization of Nanowires: The sizes and shapes of the isolated nanowires were observed using Bruker Co. model Multimode 8 AFM, and JEOL Ltd. JSM-7001F scanning electron microscope (SEM). In the height profiles of an individual nanowire, the half-width (r_w) and half-height (r_h) of the cross-section of the nanowires were evaluated. By applying the ellipsoidal model, the nanowire radius (r) was defined as $r = (r_w r_h)^{1/2}$, and the average nanowire radius was calculated by measuring the radii of 30 individual nanowires.

Sample Preparation for Electrical Measurement: Electrode patterning was performed using photolithography technique. Chromium (2 nm thick) as an adhesion layer and Au (50 nm thick) layer were formed by vapor deposition.

Measurements of Physical Properties of Nanowires: Raman spectra were measured on a JASCO NRS-4100 spectrometer. The electrical conductivity was evaluated on a micro-manipulated probe station (Lake Shore TTPX) and a semiconductor parameter analyzer (Keithley 4200A-SCS). All the measurements were performed in vacuum (~ 10^{-3} Pa) at room temperature. Temperature dependent measurement was conducted by Cryogenic Cryogen Free

Measurement System (CFMS) and electrical parameters were obtained by Keithley 2450 sourcemeter and Keithley 2182A nanovoltmeter. The information about FP-TRMC measurement is already described in **Chapter 1**.

Result and Discussion

The fullerene C_{60} molecule was chosen as a target material. Fullerenes, one of carbon allotropes which consists of spherical π-electron carbon cluster, were first reported in 1985 by Curl, Kroto, and Smalley,[36] and have been received considerable attention for its unique superconducting[37−39] and magnetic[40−42] properties. Especially, n-type semiconducting property helps us to develop functional electronic devices such as organic field-effect transistors[43,44] and photovoltaics[45,46] as an electron-acceptor. It is also known that coalescence of fullerene occurs under laser irradiation through a [2 + 2] cycloaddition resulting in fullerene dimers C_{120},[47] two fullerene cages connected by covalent bonds, and larger oligomer/polymer have been synthesized under high temperature and high pressure.[48] Application of the same polymerization *via* ion beam-initiated reactions to STLiP method have established fabrication of nanowires for organic electronic applications,[31,34] therefore, fullerene molecules can be a good candidate for first demonstration of fabrication of ultralong nanowires and subsequent evaluation of their electronic properties. **Figure 1a** depicts the protocol of fabrication of ultralong aligned nanowires. The value of LET, representing the magnitude of the energy deposited along unit trajectory length, was simulated by using the Monte-Carlo code (SRIM2008). **Figure S1b** shows the LET and range of 450 MeV $^{129}Xe^{23+}$ particles penetrating a fullerene film, which indicates Xe particles can release enough energy for nanowire formation at a distance of above 30 μm from the surface of fullerene film. In previous experiments, however, incident particles have been irradiated perpendicularly to the substrates (out-of-plane) resulting in limit of the range which is identical to the film thickness (< a few μm).

Considering this situation, a novel approach was designed, that is horizontal (in plane) irradiation realizing the best use of the beam range. **Figure 1b**–**d** shows the atomic force microscopy (AFM) topographic images of fullerene nanowires fabricated by irradiation with 450 MeV $^{129}Xe^{23+}$ particles at a fluence of $1 \times 10^9 - 1 \times 10^{11}$ cm^{-2} and subsequent development with *o*-dichlorobenzene. As can be seen from the images, most nanowires have a length of over 10 μm as expected from SRIM simulation. Some nanowires form a bundle composed of a few nanowires in case of high-fluence irradiation, implying that nanowires might interact each other within isolation in an organic solvent due to solvent effect and presence of π-π interaction of fullerene molecules. In addition, the number of nanowires is in proportion to the fluence of irradiated particles though they have no quantitative relationship, where some of irradiated particles did not go through the samples and/or some of latent nanowires escaped from the substrate in development process. Even more remarkable was that fabricated fullerene nanowires had straight configuration and were highly aligned on the substrate, which reflects trajectories of incident particles. Considering the fact that nanowires from another small molecule, rubrene, exhibited thinner and waved structures (**Figure S1c**) because of flexibility of the nanowires, this difference can likely be derived from the rigidity of fullerene nanowires which has been discussed in a previous work.[34] **Figure 1e** represents the raman spectrum of fullerene nanowires and two major peaks (the G and D' band) were observed. The G band near 1580 cm^{-1} commonly corresponds to in-plane bond stretching mode of in the lattice of the sp^2 hybridised carbon atoms. D' band broaden around 2750−3000 cm^{-1} arises from the defects and sp^3 hybridised carbon atoms, suggesting that some structural changes of fullerene backbone occurred through polymerization reactions.

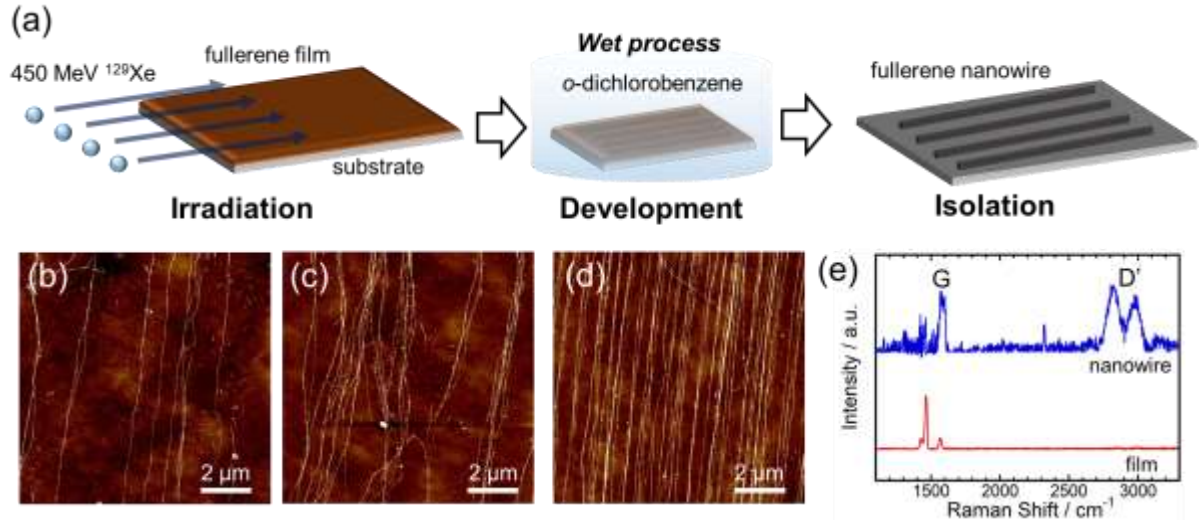

Figure 1. (a) Schematic diagram of STLiP operation for fabrication of ultralong nanowires by in-plane irradiation. (b)−(d) AFM topographic images of fullerene nanowires from a thin film of 300 nm thick irradiated with 450 MeV $^{129}Xe^{23+}$ particles at the fluence of (b) 1.0×10^{9}, (c) 1.0×10^{10}, (d) 1.0×10^{11} cm^{-2}, and developed with *o*-dichlorobenzene. (e) Raman spectra of pristine fullerene film (red) and fullerene nanowires (blue) fabricated with irradiation at the fluence of 5.0×10^{11} ions cm^{-2}.

To evaluate the electronic property of fullerene nanowires, electrical measurements were conducted. **Figure 2a** shows an overview of a prepared sample, where Au electrodes for drain and source electrode on chromium layer are deposited on nanowire-coated surface of substrates, and the gap between these electrodes (L) was fixed to 5 μm and the widths of the electrodes (W) were 100μm, 200μm, 500μm, 1000μm. The current−voltage ($I-V$) curves of fullerene nanowires are described in **Figure 2b**. There was a significant relationship between the fluence of irradiated particle and the measured conductivity, which indicates intrinsic conductivity of fabricated nanowires. This tendency was also observed in another investigation of conductivity dependence on widths of the electrodes (**Figure 2c**). **Figure 2d**

and **2e** represent $I-V$ characteristics of fullerene nanowires as a function of gate voltage (V_G) over a range from 0 V to +50 V and from 0 V to −50 V in steps of 10 V, and the plot of drain current I_{DS} against gate voltage V_G is illustrated as a transfer curve (**Figure 2f**). I_{DS} was increased as positive gate voltage increased while I_{DS} showed little change when negative gate voltage was applied, corresponding to a typical behavior of n-type semiconductors and proving the carriers in fullerene nanowire are electrons. $I-V$ curves became linear response under a low V_{DS} (< 0.1 V) exhibiting an ohmic contact, therefore, the resistivity of single nanowire can be estimated. **Figure S2** and **S3** show scanning electron microscope images of bridged nanowires over two electrodes with 100-μm-width and $I-V$ curves of each sample. Multiplying the counted number of nanowires and the resistance deduced from the slopes of $I-V$ curve, the resistances of single nanowire were calculated as 9.8×10^9 Ω and 1.1×10^{10} Ω, leading to near value. Furthermore, it is assumed that the resistance of single nanowire and the average length of bridged nanowire equal to 1.0×10^{10} Ω and the gap of 5 μm, respectively. The average cross-sectional area of nanowires were evaluated from height profiles of AFM images, as described in **Figure S4**. Eventually, the resistivity of fullerene nanowires was calculated as 1.3×10^1 Ω cm.

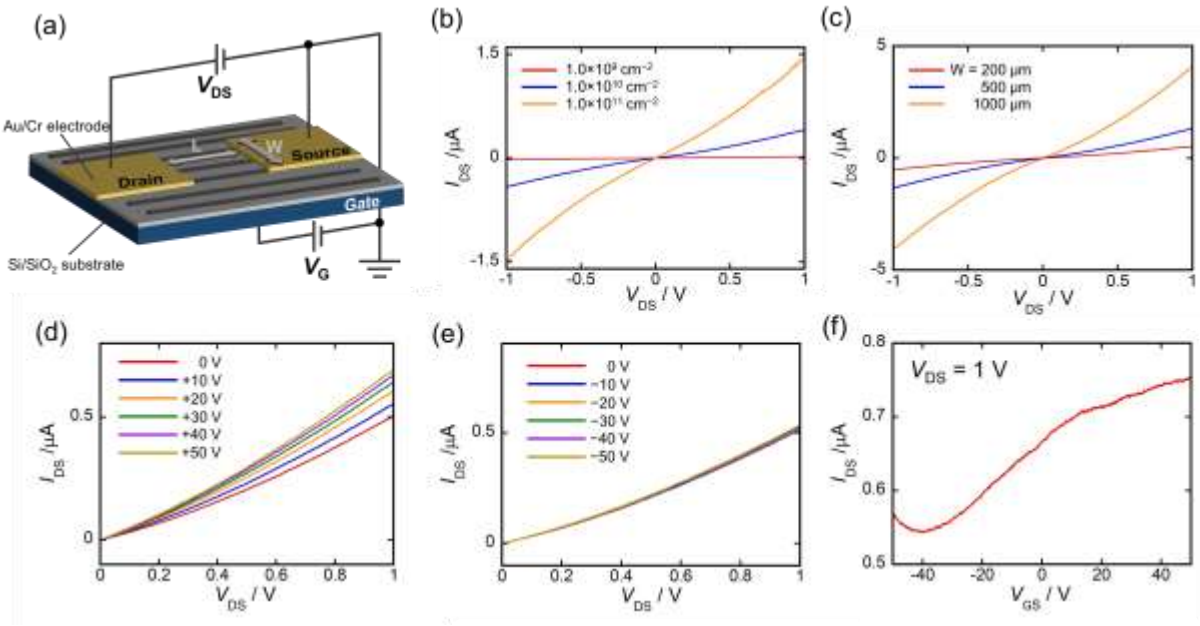

Figure 2. (a) Schematic illustration of the back-gated FET configuration. (b) Current−voltage (*I*−*V*) characteristics of fullerene nanowires with various fluences. The electrode width *W* was 200 μm. (c) *I*−*V* characteristics of fullerene nanowires with various *W*. The nanowires were fabricated at the fluence of 1.0×10^{10} cm^{-2}. (d), (e) *I*−*V* curves with various gating voltages from 0 to +50 V and from 0 to −50 V. (f) Measured transfer curve with V_{DS} fixed to 1 V. The fluence and electrode width were 1.0×10^{10} ions cm^{-2} and 200 μm, respectively in (d)−(f).

Temperature dependent experiments were conducted to explore conduction mechanism of electrons in the fullerene nanowires. As shown in **Figure 3a**, the resistance increases with decreasing temperature over the entire range of from 50 to 300 K, corresponding to well-known semiconductor property. In relatively high temperature region, the carrier transport takes place through hopping processes which is generally referred to as the nearest-neighbor-hopping (NNH) model. Thus, the conductance can be described by Arrhenius equation

$$G = G_0 \, \mathrm{e}^{-E_a/k_B T} \tag{1}$$

where G_0 is a pre-exponential factor and E_a is the activation energy, and the ln G versus 1/T plot well fitted with the equation in the range of from 200 to 300 K (**Figure 3b**). In relatively low temperature region, on the other hand, the Arrhenius plot does not show linear dependence because the current should be carried via variable range hopping (VRH) mechanisms and the conductance can be described as

$$G = G_0 \, \mathrm{e}^{-(T_0/T)^p} \tag{2}$$

where T_0 is a characteristic temperature and exponent p is characteristic exponent. Based on Mott's VRH conduction,[49] exponent p is defined as $p = 1/(d + 1)$ where d is dimension of the system, thus p can be 1/2 in the present 1D nanowire network. However, there is no linear dependence in the ln G versus $1/T^{1/2}$ plot (**Figure 3c**). This reduction of temperature dependence would be explained by the fact that current-voltage characteristic can no longer be described as linear conduction in ohmic regime as decreasing temperature (**Figure 3d**), indicating electric-field-driven hopping transport where the energy necessary for hopping is obtained from the electric field rather than temperature.

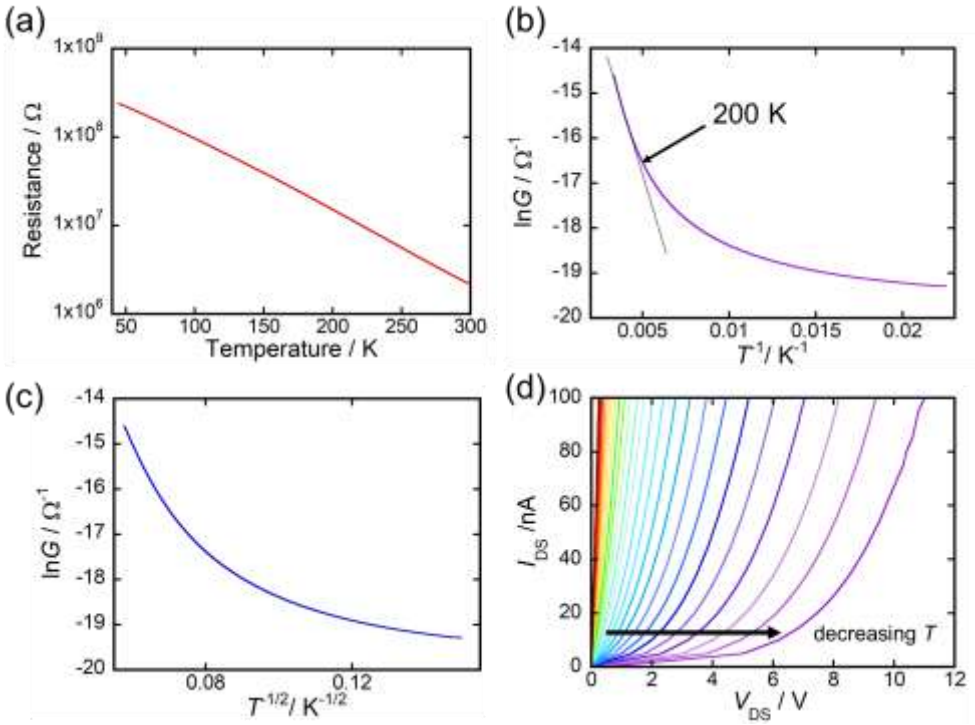

Figure 3. (a) Resistance of fullerene nanowires plotted against temperature T. Nanowires were fabricated by irradiation with 450 MeV $^{129}Xe^{23+}$ particles at the fluence of 1.0×10^{11} cm^{-2}. The electrode width W was 200 μm. (b)(c) ln G plotted against T^{-1} and $T^{-1/2}$. Black dotted line represents fitting based on eq. (1) obtained over the range of from 200 to 300 K. (d) I_{DS}–V_{DS} curves at different temperatures from 50 to 300 K in steps of 10 K.

As mentioned above, a notable advantage of the novel in-plane irradiation is highly alignment of fabricate nanowires. To investigate the anisotropic conductivity of the nanowire ensemble, flash-photolysis time-resolved microwave conductivity (FP-TRMC) measurement (already explained in detail in **Chapter 1** and **Chapter 3**) was conducted. **Figure 4** shows the conductivity transient in a microwave cavity whose electric field direction was parallel or perpendicular to 1D direction of nanowires. When electric field was set parallel to the nanowire direction, the maximum value of $\phi\Sigma\mu$ reaches 2.4×10^{-8} m^2 V^{-1} s^{-1}, while significantly reduced transient conductivity was observed when electric field was set perpendicular to the

nanowire direction. Given that, in the FP-TRMC experiment, the carriers generated by laser pulse irradiation travel along the direction of electric field of oscillating microwave, these results confirm the anisotropic carrier conduction along the nanowire direction.

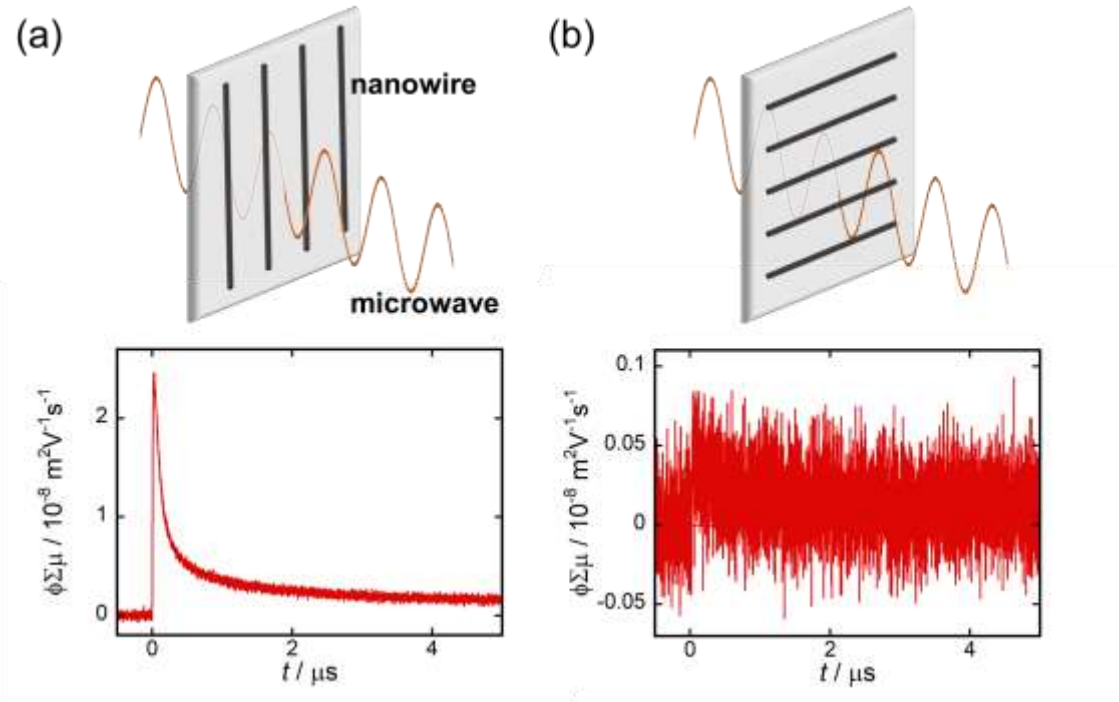

Figure 4. Transient conductivity for fullerene nanowires under an excitation at 355 nm , 10 mJ cm^{-2}. Nanowires were fabricated on a quartz substrate by irradiation with 450 MeV $^{129}Xe^{23+}$ particles at a fluence of 1.0×10^{11} cm^{-2}. Top figures illustrate the configuration of nanowires and microwave where nanowires are aligned (a) parallel and (b) perpendicular to the microwave oscillation.

Conclusion

This study first demonstrated a novel approach creating ultralong fullerene nanowires with the aspect ratio of over 1000. The number density of fabricated nanowires increased

proportionally to the number of irradiated particles. From electric measurements, current-voltage curves were changed corresponding to the fluence of irradiated particles and the width of the source and drain electrodes, suggesting that the observed conductivity were derived from fullerene nanowires with the calculated resistivity of $1.3 \times 10^8\ \Omega$ m. In addition, the field-effect transistor experiment revealed that the fullerene nanowire exhibited typical behavior of n-type semiconductor. Variable temperature experiments denoted the mechanism of the carrier transport where thermal activated conduction and/or nearest neighbor hopping were occur in high temperature regime while electric-field driven hopping took place in low temperature regime, which was proposed from Arrhenius plotting. Furthermore, FP-TRMC measurement clarified the anisotropic photoconductivity whose difference was almost 10^2 times depending on nanowire direction parallel or perpendicular to microwave oscillation. Considering the STLiP method can be applied to a wide series of organic molecules, this feasible and practical technique fabricating ultralong nanowires are desired to be utilized for producing nanomaterials in various field.

References

1. Cui, Y., Wei, W., Park, H., Liber, C. M. *Science* **2001**, *293*, 1289.
2. Fischer, K. E., Aleman, B. J., Tao, S. L., Daniels, R. H., Li, E. M., Bünger, M. D., Nagaraj, G., Singh, P., Zettl, A., Desai, T. A. *Nano Lett.* **2009**, *9*, 716.
3. Huang, M. H., Mao, S., Feick, H., Yan, H., Wu, Y., Kind, H., Weber, E. Russo, R. Yang, P. *Science* **2001**, *292*, 1897.
4. Liu, E.-S., Nah, J., Varahramyan, K. M., Tutuc, E. *Nano Lett.* **2010**, *10*, 3297.
5. Snyder, G. J., Toberer, E. S. *Nat. Mater.* **2008**, *7*, 105.
6. Chan, C. K.; Peng, H.; Liu, G.; McIlwrath, K.; Zhang, X. F.; Huggins, R. A.; Cui, Y. *Nat. Nanotechnol.* **2008**, *3*, 31.

7. Wagner, R. S., Ellis, W.C. *Appl. Phys. Lett.* **1964**, *4*, 89.
8. Holmes, J. D., Johnston, K. P., Doty, R. C., Korgel, B. A. *Science* **2000**, 287, 1471.
9. Cheze, C., Geelhaar, L., Trampert, A., Brandt, O., Riechert, H.` *Nano Lett*. **2010**, *10*, 3426.
10. Lensch-Falk, J. L., Hemesath, E. R., Lopez, F. J., Lauhon, L. J. *J. Am. Chem. Soc*. **2007**, *129*, 10670.
11. Yan, Q., Chen, H., Zhou, W., Hng, H. H., Boey Yin Chiang, F.; Ma, *J. Chem. Mater.* **2008**, *20*, 6298.
12. Sun, Y., Gates, B., Mayers, B., Xia, Y. *Nano Lett.* **2002**, *2*, 165.
13. Dubin, F., Melet, R., Barisien, T., Grousson, R., Legrand, L., Schott. M., Voliotis, V. *Nat. Phys.* **2006**, *2*, 32.
14. Jin, X. -H., Price, M. B., Finnega, J. R., Boott, C. E., Rither, J. M., Rao, A., Menke, S. M., Friend, R. H., Whittell, G. R., Manners, I. *Science* **2018**, *360*, 897.
15. Levenson, M. D. *Solid State Technol.* **1995**, September, 81.
16. Dunn, P. N. *Solid State Technol.* **1994**, June, 49.
17. Colinge, J.-P, Lee, C.-W., Afzalian, A., Akhavan, N. D., Yan, R., Ferain, I., Razavi, P., O'Neill, B., Blake, A., White, M., Kelleher, A.- M., McCarthy, B., Murphy, R. *Nat. Nanotechnol.* **2010**, *5*, 225.
18. Trivedi, K., Yuk, H., Floresca, H. C., Kim, M. J., Hu, W. *Nano Lett*. **2011,** *11*, 1412.
19. Sidorkin, V., Veldhoven, E. van, Drift, E. van der, Alkemade, P., Salemink, H., Maas, D. *J. Vac. Sci. Technol.*, *B* **2009**, *27*, 25.
20. Winston, D., Manfrinato, V. R., Nicaise, S. M., Cheong, L. L., Duan, H., Ferranti, D., Marshman, J., McVey, S., Stern, L., Notte, J., Berggren, K. K. *Nano Lett.* **2011**, *11*, 4343.
21. Bethe, H. *Ann. Phys.* **1930**, *5*, 325.
22. Bethe, H. *Z. Phys.* **1932**, *76*, 293.
23. Bloch, F. *Ann. Phys.* **1933**, *16*, 285.

24. Pérez-Mitta, G., Albesa, A.G., Knoll, W., Trautmann, C., Toimil-Molares, M.E. Azzaroni, O. *Nanoscale* **2015**, *7*, 15594–15598.

25. Yameen, B., Ali, M., Neumann, R., Ensinger, W., Knoll, W., Azzaroni, O. *Small* **2009**, *5*, 1287.

26. Seki, S.; Maeda, K.; Tagawa, S.; Kudoh, H.; Sugimoto, M.; Morita, Y.; Shibata, H. *Adv. Mater*. **2001**, *13*, 1663.

27. Seki, S.; Tsukuda, S.; Maeda, K.; Matsui, Y.; Saeki, A.; Tagawa, S. *Phys. Rev. B* **2004**, *70*, 144203.

28. Seki, S.; Tsukuda, S.; Maeda, K.; Tagawa, S.; Shibata, H.; Sugimoto, M.; Jimbo, K.; Hashitomi, I.; Kohyama, A. *Macromolecules* **2005**, *38*, 10164.

29. Omichi, M.; Asano, A.; Tsukuda, S.; Takano, K.; Sugimoto. M.; Saeki, A.; Sakamaki, D.; Onoda, A.; Hayashi, T.; Seki, S. *Nat. Commun.* **2014**, *5*, 3718.

30. Maeyoshi, Y.; Saeki, A.; Suwa, S.; Omichi, M.; Marui, H.; Asano, A.; Tsukuda, S.; Sugimoto, M.; Kishimura, A.; Kataoka, K.; Seki, S. *Sci. Rep.* **2012**, *2*, 600.

31. Sakaguchi, S.; Sakurai, T.; Ma, J.; Sugimoto, M.; Yamaki, T.; Chiba, A.; Saito, Y.; Seki, S. *J. Phys. Chem. B* **2018**, *122*, 861.

32. Horio, A.; Sakurai, T.; Lakshmi, G. B. V. S.; Avasthi, D. K.; Sugimoto, M.; Yamaki, T.; Seki, S. *Nanoscale* **2016**, *8*, 14925.

33. Sakurai, T., Sakaguchi,. S., Takeshita, Y., Kayama, K., Horio, A., Sugimoto, M., Yamaki, T., Chiba, A., Saitoh, Y., Garimella, L.B.V.S., Avasthi, D., Seki, S. *ACS Appl. Nano Mater.*, **2020**, *3*, 6043.

34. Kamiya, K., Kayama, K., Nobuoka, M., Sakaguchi, S., Sakurai, T., Kawata, M., Tsutsui, Y., Suda, M., Idesaki, A., Koshikawa, H., Sugimoto, M., Lakshmi, G.B.V.S., Avasthi, D. K., Seki, S. *Nat. Commun*. **2021**, *12*, 4025.

35. Sakaguchi, S. Kamiya, K., Sakurai, T., Seki, S. *Quantum Beam Sci.* **2020**, *4*, 7.

36. Kroto, H. W., Heath, J. R., O'Brien, S. C., Curl, R. F., Smalley, R. E. *Nature* **1985**, *318*, 162.

37. Hebard, A. F., Rosseinsky, M. J., Haddon, R. C., Murphy, D. W., Glarum, S. H., Palstra, T. T. M., Ramirez, A. P., Kortan, A. R. *Nature* **1991**, *350*, 600.

38. Schon, J., Kloc, C., Batlogg, B. *Scince* **2001**, *293*, 2432.

39. Dagotto, E. *Science* **2001**, *293*, 2410.

40. Allemand, P.-M., Khemani, K. C., Koch, A., Wudl, F., Holczer, K., Donovan, S., Grüner, G., Thompsom, J. D. Science 1991, 253, 301–303.

41. Makarova, T. L., Sundqvist, B., Hohne, R., Esquinazi, P., Kopelevich, Y., Scharff, P., Davydov, V. A., Kashevarova, L. S., Rakhmanina, A. V. *Nature* **2001**, *413*, 716.

42. Narymbetov, B., Omerze, A., Kabanov, V. V., Tokumoto, Kobayashi, H., Mihailovic, D. *Nature* **2000**, *407*, 883.

43. Haddon, R. C., Perel, A. S., Morris, R. C., Palstra, T. T. M., Hebard, A. F., Fleming, R., M., *Appl. Phys. Lett.* **1995**, *67*, 121.

44. Kobayashi, S., Takenobu, T., Mori, S. *Appl. Phys. Lett.* **2003**, *82*, 4581.

45. Song, X., Hua, W., Ma, Y., Wang, C., Luo, Y. *J. Phys. Chem. C*, **2012**, *116*, 23938.

46. Lenes, M., Shelton, S. W., Sieval, A. B., Kronholm, D. F., Hummelen, J. C., Blom, P.W. M. *Adv. Funct. Mater.*, **2009**, *19*, 3002.

47. Yeretzian, C., Hauser, K., Diederich, F., whetten, R. Nature, **1992**, *359*, 44.

48. Blank, A., Buga, S. G., Serebryanaya, N. R., Denisov, V. N., Dubitsky, G. A., Ivlev, A. N., Mavrin, B. N., Popov, M. Yu. *Phys. Lett. A* **1995**, *205*, 208.

49. Mott, N. F. *J. Non-Cryst. Solids* **1968**, *1*, 1.

Chapter 4 Appendix

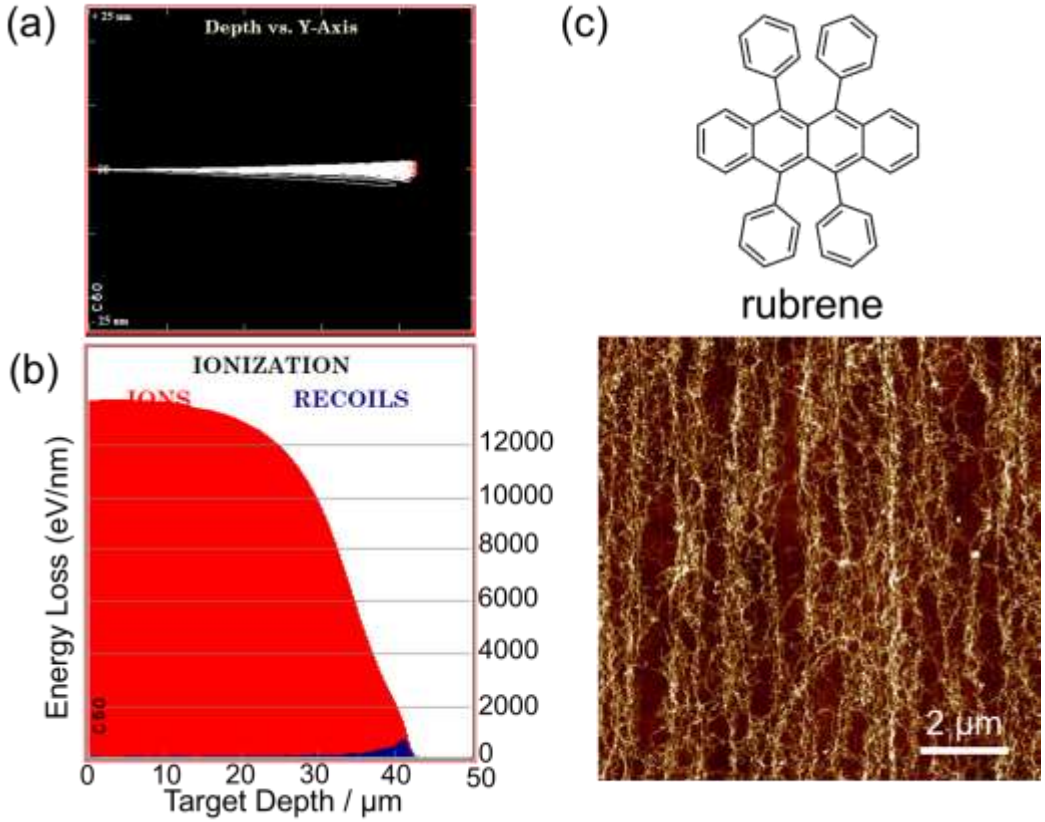

Figure S1. (a)(b) Calculated ion trajectories of 450 MeV Xe ions penetrating a 50 μm-thick fullerene film and calculated LET against the distance from the film surface. (c) Chemical structure of rubrene and a AFM topographic image of rubrene nanowires fabricated from a 500 nm-thick film by irradiation of $^{129}Xe^{23+}$ particles at a fluence of 1.0×10^{11} cm^{-2}.

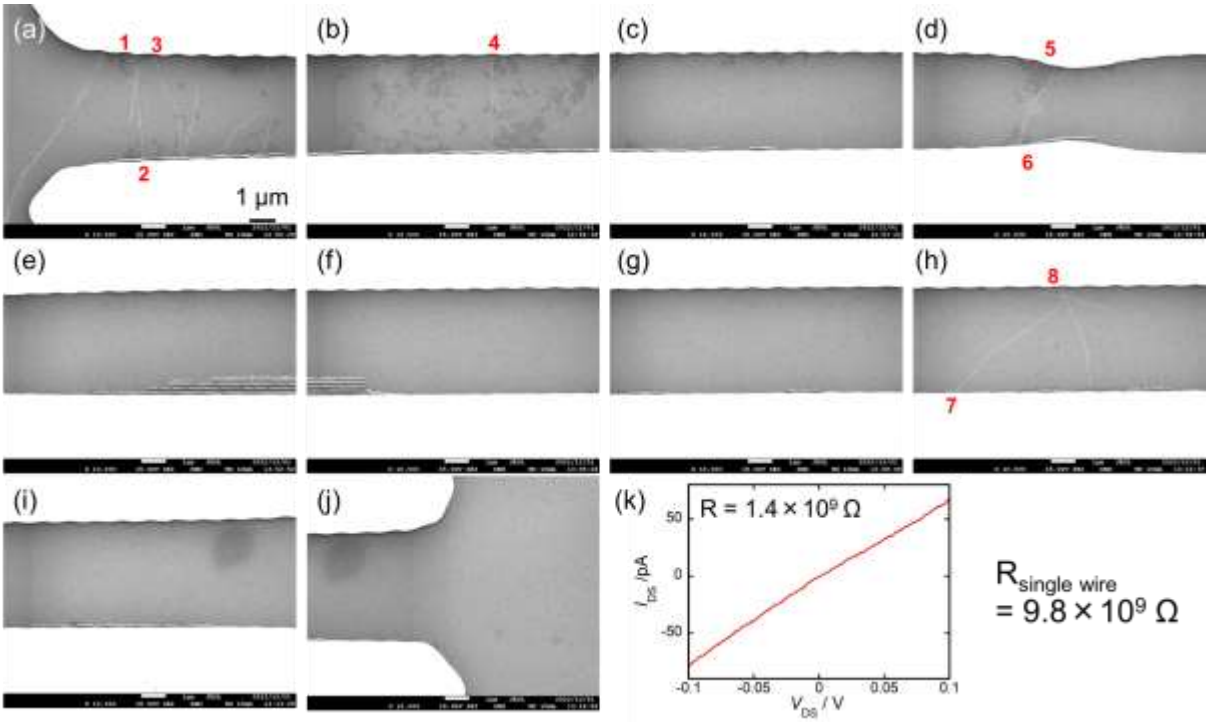

Figure S2. (a)−(j) SEM imaged of fullerene nanowires bridged between 5 μm-gap electrodes. Red numbers represent position and the number of nanowires. (k) Current-voltage characteristic and resistance R calculated from the slope of $I-V$ curve and estimated resistance of single nanowire $R_{\text{single wire}}$.

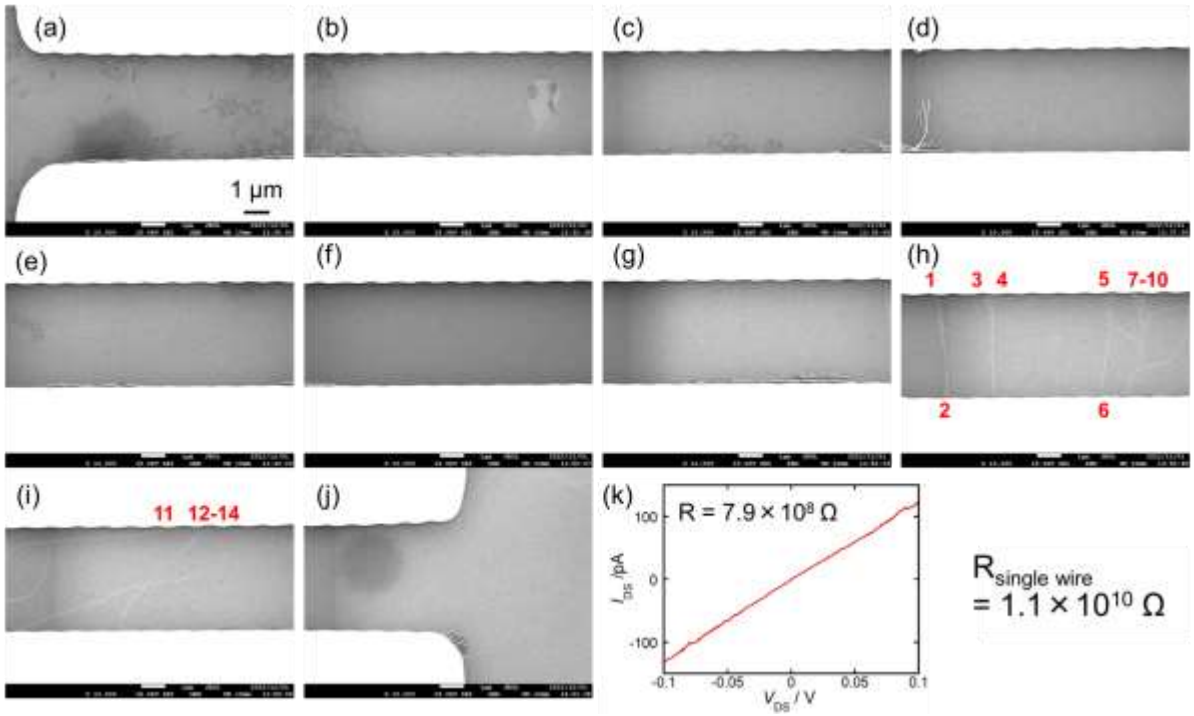

Figure S3. (a)−(j) SEM imaged of fullerene nanowires bridged between 5 μm-gap electrodes. Red numbers represent position and the number of nanowires. (k) Current-voltage characteristic and resistance R calculated from the slope of $I-V$ curve and estimated resistance of single nanowire $R_{\text{single wire}}$.

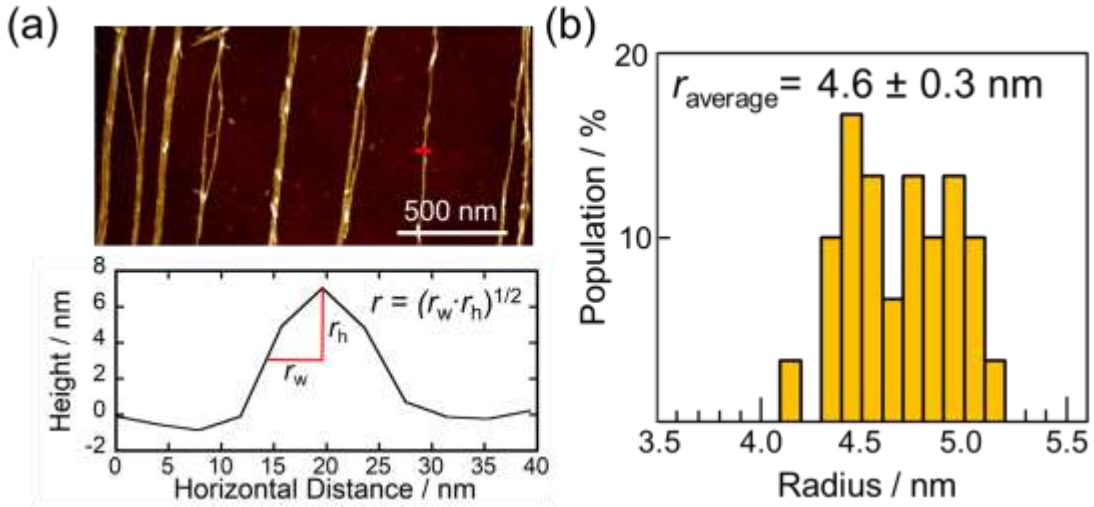

Figure S4. (a) AFM topographic image of fullerene nanowires and its height profile obtained from cross-section at the red line in the AFM image. (b) The radius distribution and the average radius of isolated 30 nanowires fabricated by irradiation with 450 MeV $^{129}Xe^{23+}$ particles

General Conclusion

In this thesis, comprehensive study have been conducted on ion-beam-induced polymerization reactions and fabrication of sub-10-nm scale nanowires from several π-conjugated molecules. The structural, optical, and electrical properties of synthesized nanowires are evaluated by microscopic and spectroscopic analysis, which indicates the outstanding potentials as nanomaterials.

In chapter 1, Spirobifluorene and its derivatives (**SBF** and brominated **SBF**) are the target materials. The structural property shows precise controlled nanowire form with uniform lengths and cross-sectional radii where the cross-sectional radii of brominated **SBF** nanowires are enhanced by increase of intra-track reaction efficiency due to bromination of **SBF** cores. Theoretical treatments suggests that the reaction efficiency (*G* value) can be estimated as 8.6–9.7 $(100\ \text{eV})^{-1}$ for **SBF** derivatives upon irradiation with 350 MeV ^{129}Xe particles. Fluorescence measurements of obtained **SBF**-based nanowire reveals emission bands red-shifted from those of the pristine **SBF** film, indicating the existence of extended aromatic structures via polymerization reactions. Demonstration of the sensing ability of the nanowires is confirmed by fluorescence quenching and photoconductivity enhancement with presence of electron-accepting analyte.

In chapter 2, the mechanism of polymerization reaction triggered by 450 MeV $^{129}Xe^{23+}$ particles is investigated by information of fabricated nanowires from brominated and ethynyl-substituted **SBF** derivatives. Comparing the radii of the nanowires and subsequent estimation of *G* values, it is revealed that the polymerization efficiency of ethynyl-substituted **SBF** is increased more than that of brominated and non-substituted one, suggesting generation of highly-reactive vinyl radicals as a result of the reaction between an initially-generated radical and carbon-carbon triple bond.

In chapter 3, tetraphenylporphyrin (TPP) derivatives are exploited for nanowires fabrication. The obtained nanowires exhibit larger photoconductivity than the pristine amorphous films of porphyrin monomers most likely due to the conformation change of π-stacked porphyrin aggregates. UV-vis and IR measurements indicates that porphyrin analogue is still remained in fabricated nanowires which potentially exhibit a photosensitize ability for the production of singlet oxygens, which can be useful for the photocatalysis and photodynamic therapy. In addition, porphyrin nanowires on Ag nanoparticles resulted in enhanced fluorescence due to the excitation from the surface plasmon resonance of Ag nanoparticles at around 420 nm.

In chapter 4, fabrication of ultralong (> 10 μm length) nanowire is demonstrated by redesigning the irradiation process in the STLiP protocol. Electric measurements of obtained fullerene nanowires implies the carrier (electron) transport as a n-type semiconductor along the 1D nanowire structure and resistivity of the nanowires are calculated as 1.3×10^8 Ω m. Temperature dependence of electric properties suggests that the carrier transport occurs in nanowire network through nearest neighbor hopping at high temperature (> 200 K), while non-ohmic regime was observed at low temperature due to electric-field driven hopping. FP-TRMC measurement reveals the anisotropic photoconductivity depending on nanowire alignment direction against electric-filed generated by the microwave, which supports the advantage of this new approach with fabrication of highly-aligned nanowires.

At the end, dimension of nanostructures, nanomaterials, and nanodevices is scaling down day-by-days since the second half of the last century, concurrently to the development of electronic integrated circuits. Now the dimension is approaching the sizes equivalent to that of small organic molecules. Chemical reactions within the dimension induced by ionizing radiations have played always a crucial role in the determination of the sizes as well as their accuracy. “Single particle” provides an ultimate limit of the spatial distribution (chemical

reaction field) as the energy source, and herein the successful nanomaterials fabrication is discussed and reviewed through the energy released within the field. Starting from the visualization of latent tracks formed by high energy charged particles given by nuclear reactions, a variety of applications as well as direct formation of the materials have been developed till date, with advantages to widely used nanofabrication techniques employed particularly in semiconductor industries as follows: 1) intrinsically small special size of chemical reaction fields, 2) extremely high aspect ratio of the field reflecting intrinsic “indivisible” nature of single particle, and 3) facile way to combine a variety of nanomaterials. Considering the ubiquitous nature of high energy charged particle at the outside of our Earth, puzzling out the total landscape of the high energy particle induced reactions will be contact to the origin of organic molecule, and the scenario to the origin of the breaking symmetry in our lives.

List of Publication

Chapter 1

"Conjugated Nanowire Sensors via High-Energy Single-Particle-Induced Linear Polymerization of 9,9'-spirobi[9*H*-fluorene] Derivatives"

Sakaguchi, S., Sakurai, T., Ma, J., Sugimoto, M., Yamaki, T., Chiba, A., Saito, Y., Seki, S. *J. Phys. Chem. B* **2018**, *122*, 8614–8623.

Chapter 2

"Highly Efficient Solid-State Intra-Track Polymerization of Ethynyl-Substituted Spirobifluorenes Triggered by Swift Heavy Ion Irradiations"

Sakaguchi, S., Sakurai, T., Idesaki, A., Koshikawa, H., Sugimoto, M., Seki, S. *J. Photopolym. Sci. Technol.* **2020**, *33*, 91–96.

Chapter 3

"Porphyrin Nanowire Bundles for Efficient Photoconductivity, Photoemission, and Generation of Singlet Oxygens toward Photodynamic Therapy"

Sakurai, T., **Sakaguchi, S.**, Takeshita, Y., Kayama, K., Horio, A., Sugimoto, M., Yamaki, T., Chiba, A., Saitoh, Y., Garimella, L.B.V.S., Avasthi, D., Seki, S. *ACS Appl. Nano Mater.*, **2020**, *3*, 6043.

Chapter 4

"Fabrication of Ultralong Aligned Fullerene Nanowires Using Swift Heavy Ion Beam"

Sakaguchi, S., Idesaki, A., Koshikawa, H., Seki, S. *to be submitted*

Supplementary Publication

"Interactions of Single Particle with Organic Matters: A Facile Bottom-Up Approach to Low Dimensional Nanostructures"

Sakaguchi, S., Kamiya, K., Sakurai, T., Seki, S. *Quantum Beam Sci.* **2020**, *4*(1), 7.